The Astrophysical Journal, 777:5 (33pp), 2013 November 1 doi:10.1088/0004-637X/777/1/5

THE CO-TO-H_2 CONVERSION FACTOR AND DUST-TO-GAS RATIO ON KILOPARSEC SCALES IN NEARBY GALAXIES

K. M. Sandstrom[1,32], A. K. Leroy[2], F. Walter[1], A. D. Bolatto[3], K. V. Croxall[4,5], B. T. Draine[6], C. D. Wilson[7], M. Wolfire[3], D. Calzetti[8], R. C. Kennicutt[9], G. Aniano[6,10], J. Donovan Meyer[11], A. Usero[12], F. Bigiel[13], E. Brinks[14], W. J. G. de Blok[15], A. Crocker[4,8], D. Dale[16], C. W. Engelbracht[17,18], M. Galametz[9], B. Groves[1], L. K. Hunt[19], J. Koda[11], K. Kreckel[1], H. Linz[1], S. Meidt[1], E. Pellegrini[4], H.-W. Rix[1], H. Roussel[20], E. Schinnerer[1], A. Schruba[21], K.-F. Schuster[22], R. Skibba[17,23], T. van der Laan[1], P. Appleton[24], L. Armus[25], B. Brandl[26], K. Gordon[27], J. Hinz[17,28], O. Krause[1], E. Montiel[17,29], M. Sauvage[30], A. Schmiedeke[1,31], J. D. T. Smith[4], and L. Vigroux[20]

[1] Max Planck Institut für Astronomie, Königstuhl 17, D-69117 Heidelberg, Germany; sandstrom@mpia.de
[2] National Radio Astronomy Observatory, 520 Edgemont Road, Charlottesville, VA 22903, USA
[3] Department of Astronomy, University of Maryland, College Park, MD 20742, USA
[4] Department of Physics and Astronomy, Mail Drop 111, University of Toledo, 2801 West Bancroft Street, Toledo, OH 43606, USA
[5] Department of Astronomy, The Ohio State University, 140 West 18th Avenue, Columbus, OH 43210, USA
[6] Princeton University Observatory, Peyton Hall, Princeton, NJ 08544-1001, USA
[7] Department of Physics and Astronomy, McMaster University, Hamilton, Ontario L8S 4M1, Canada
[8] Department of Astronomy, University of Massachusetts, Amherst, MA 01003, USA
[9] Institute of Astronomy, University of Cambridge, Madingley Road, Cambridge CB3 0HA, UK
[10] Institut d'Astrophysique Spatiale (IAS), bâtiment 121, Université Paris-Sud 11 and CNRS (UMR 8617), F-91405 Orsay, France
[11] Department of Physics and Astronomy, SUNY Stony Brook, Stony Brook, NY 11794-3800, USA
[12] Observatorio Astronómico Nacional, Alfonso XII, 3, E-28014 Madrid, Spain
[13] Institut für theoretische Astrophysik, Zentrum für Astronomie der Universität Heidelberg, Albert-Ueberle Str. 2, D-69120 Heidelberg, Germany
[14] Centre for Astrophysics Research, University of Hertfordshire, Hatfield AL10 9AB, UK
[15] ASTRON, The Netherlands Institute for Radio Astronomy, Postbus 2, 7990-AA Dwingeloo, The Netherlands
[16] Department of Physics and Astronomy, University of Wyoming, Laramie, WY 82071, USA
[17] Steward Observatory, University of Arizona, Tucson, AZ 85721, USA
[18] Raytheon Company, 1151 East Hermans Road, Tucson, AZ 85756, USA
[19] INAF-Osservatorio Astrofisico di Arcetri, Largo E. Fermi 5, I-50125 Firenze, Italy
[20] Institut d'Astrophysique de Paris, UMR 7095 CNRS, Université Pierre et Marie Curie, F-75014 Paris, France
[21] California Institute for Technology, 1200 East California Boulevard, Pasadena, CA 91125, USA
[22] IRAM, 300 rue de la Piscine, F-38406 St. Martin d'Héres, France
[23] Center for Astrophysics and Space Sciences, University of California, 9500 Gilman Drive, San Diego, CA 92093, USA
[24] NASA Herschel Science Center, IPAC, California Institute of Technology, Pasadena, CA 91125, USA
[25] Spitzer Science Center, California Institute of Technology, MC 314-6, Pasadena, CA 91125, USA
[26] Leiden Observatory, Leiden University, P.O. Box 9513, 2300-RA Leiden, The Netherlands
[27] Space Telescope Science Institute, 3700 San Martin Drive, Baltimore, MD 21218, USA
[28] MMT Observatory, Tucson, AZ 85721, USA
[29] Department of Physics and Astronomy, Louisiana State University, Baton Rouge, LA 70803, USA
[30] CEA/DSM/DAPNIA/Service d'Astrophysique, UMR AIM, CE Saclay, F-91191 Gif sur Yvette Cedex, France
[31] Universität zu Köln, Zülpicher Strasse 77, D-50937 Köln, Germany
Received 2012 December 4; accepted 2013 July 9; published 2013 October 8

ABSTRACT

We present ∼kiloparsec spatial resolution maps of the CO-to-H_2 conversion factor (α_{CO}) and dust-to-gas ratio (DGR) in 26 nearby, star-forming galaxies. We have simultaneously solved for α_{CO} and the DGR by assuming that the DGR is approximately constant on kiloparsec scales. With this assumption, we can combine maps of dust mass surface density, CO-integrated intensity, and H I column density to solve for both α_{CO} and the DGR with no assumptions about their value or dependence on metallicity or other parameters. Such a study has just become possible with the availability of high-resolution far-IR maps from the *Herschel* key program KINGFISH, ^{12}CO $J =$ (2–1) maps from the IRAM 30 m large program HERACLES, and H I 21 cm line maps from THINGS. We use a fixed ratio between the (2–1) and (1–0) lines to present our α_{CO} results on the more typically used ^{12}CO $J =$ (1–0) scale and show using literature measurements that variations in the line ratio do not affect our results. In total, we derive 782 individual solutions for α_{CO} and the DGR. On average, $\alpha_{CO} = 3.1\ M_\odot\ \mathrm{pc}^{-2}\ (\mathrm{K\ km\ s}^{-1})^{-1}$ for our sample with a standard deviation of 0.3 dex. Within galaxies, we observe a generally flat profile of α_{CO} as a function of galactocentric radius. However, most galaxies exhibit a lower α_{CO} value in the central kiloparsec—a factor of ∼2 below the galaxy mean, on average. In some cases, the central α_{CO} value can be factors of 5–10 below the standard Milky Way (MW) value of $\alpha_{CO,MW} = 4.4\ M_\odot\ \mathrm{pc}^{-2}\ (\mathrm{K\ km\ s}^{-1})^{-1}$. While for α_{CO} we find only weak correlations with metallicity, the DGR is well-correlated with metallicity, with an approximately linear slope. Finally, we present several recommendations for choosing an appropriate α_{CO} for studies of nearby galaxies.

Key words: dust, extinction – galaxies: ISM – infrared: ISM – ISM: molecules

Online-only material: color figures, figure set

1. INTRODUCTION

The H_2 molecule is difficult to observe in the prevalent interstellar medium (ISM) conditions of a normal star-forming galaxy. Since H_2 is the primary constituent of molecular gas, inferring its mass is crucial for studying this phase of the ISM and the star formation that occurs within it. A widespread practice is to use the second most abundant molecule, carbon monoxide (^{12}CO), as a tracer and convert the measured CO integrated intensities into H_2 column densities using a "CO-to-H_2" conversion factor X_{CO}[33]:

$$N_{H_2} = X_{CO} I_{CO}. \quad (1)$$

In mass surface density units, this equation can be rewritten as:

$$\Sigma_{H_2} = \alpha_{CO} I_{CO}, \quad (2)$$

where Σ_{H_2} is the total mass surface density of molecular gas (including a correction for the second most abundant element, He). A variety of observations have shown that $\alpha_{CO} \approx 4.4\ M_\odot\ pc^{-2}\ (K\ km\ s^{-1})^{-1}$ is characteristic of the local area of the Milky Way (MW; Solomon et al. 1987; Strong & Mattox 1996; Abdo et al. 2010). Despite uncertainties in the physics behind the conversion factor, the observability of CO ensures that it will remain a widely used molecular gas tracer, particularly at high redshift.

α_{CO} is used in a variety of contexts in Galactic and extragalactic studies. In the following, we define and measure α_{CO} on ~kiloparsec scales in nearby galaxies. At these resolutions, the small-scale structure of the ISM is averaged out and the variation in α_{CO} is driven by large-scale changes in the galactic environment (e.g., metallicity, galactic dynamics, ISM pressure). In general, extragalactic studies have adopted a single value of α_{CO} for entire galaxies. The new ability to perform systematic studies of α_{CO} on sub-galactic scales in nearby galaxies facilitated by high angular resolution maps of gas and dust will let us move beyond this simplistic assumption.

In addition, studying α_{CO} on ~kiloparsec scales has several advantages: (1) because we do not resolve molecular clouds, we avoid issues with sampling the cloud structure (e.g., envelopes of CO-free H_2); (2) because our resolution element contains many clouds, we average over cloud evolutionary effects; and (3) we cover large enough fractions of the total molecular gas mass in a galaxy that it becomes reasonable to generalize our results to determine α_{CO} values appropriate for integrated galaxy measurements. It is important to note that our definition of α_{CO} is distinct from the line-of-sight Σ_{H_2}/I_{CO} one can measure in small regions of Galactic molecular clouds—in such cases the conversion factor is not well defined since it does not sample the full structure of the cloud.

In order to measure the conversion factor, one must measure Σ_{H_2} (or equivalently, $\Sigma_{gas} - \Sigma_{H\,I}$) independently of CO and then compare it to observed CO integrated intensities. This measurement has been accomplished using a variety of techniques, including: measuring total gas masses from γ-ray emission plus a model for the cosmic ray distribution (Strong & Mattox 1996; Abdo et al. 2010), using the observed velocity dispersion and size of the molecular cloud to obtain virial masses (Solomon et al. 1987; Wilson 1995; Bolatto et al. 2008; Donovan Meyer et al. 2012; Wei et al. 2012; Gratier et al. 2012), and modeling multiple molecular gas lines with varying optical depths and critical densities (e.g., Weiß et al. 2001; Israel 2009a, 2009b). In general, few of these techniques are effective for constraining α_{CO} in galaxies outside the Local Group due to the difficulty of obtaining the necessary observations (i.e., γ-ray maps or CO mapping at <100 pc resolution) or doubts about fundamental assumptions (e.g., that CO traces the full extent of molecular gas in the clouds; that the clouds lack contributions to virial balance from magnetic or pressure forces; that simple radiative transfer models can reproduce molecular gas excitation on kiloparsec scales).

Another possible technique to measure Σ_{H_2} is to use dust as a tracer of the total gas column. Assuming that dust and gas are well mixed, the dust-to-gas ratio (DGR) is not a function of atomic/molecular phase, and the fraction of mass in ionized gas is negligible, the observed dust mass surface density can be converted to a gas mass surface density with information on the DGR, i.e., using the following equation:

$$\frac{\Sigma_D}{DGR} = \Sigma_{H\,I} + \Sigma_{H_2} = \Sigma_{H\,I} + \alpha_{CO} I_{CO}. \quad (3)$$

Here, Σ_D is the mass surface density of dust and $\Sigma_{H\,I}$ and Σ_{H_2} are the mass surface densities of atomic and molecular gas,[34] respectively, and DGR is the dust-to-gas mass ratio. By measuring Σ_D and $\Sigma_{H\,I}$ and assuming the DGR (or simultaneously measuring it, as we will discuss shortly), the molecular gas mass can be determined. While still subject to its own systematic uncertainties (discussed in detail in Section 3.4), this technique relies on a different set of assumptions than those techniques mentioned previously.

Studies of the DGR or α_{CO} have typically fixed one of the parameters in order to determine the other, so it is difficult to avoid circularity when using a fixed DGR to solve for α_{CO} in Equation (3). Alternatively, with sufficiently high spatial resolution, the DGR can be determined along sight-lines free of molecular gas and extrapolated to regions where CO is detected. For very nearby galaxies like the Magellanic Clouds, such a technique has been used by Israel (1997) and Leroy et al. (2009a), who found that α_{CO} determinations from virial masses can be strongly biased by envelopes of "CO-dark" molecular gas in low-metallicity systems. In more distant galaxies, we generally cannot isolate purely atomic lines of sight at the resolution of typical H I and CO observations. Instead, it is possible to use a technique developed by Leroy et al. (2011) to simultaneously measure α_{CO} and the DGR using the assumption that the DGR should be constant over a region of a galaxy. Since we can now achieve ~kiloparsec spatial resolution in the far-infrared (far-IR) with *Herschel* and have sensitive, high-resolution CO and H I maps, it is possible to extend this technique, which has thus far only been applied to the Local Group, to more distant galaxies.

The idea behind this technique (explained in detail in Section 3) is that spatially resolved measurements of Σ_D, $\Sigma_{H\,I}$, and I_{CO} allow one to solve for α_{CO} and the DGR over regions smaller than the typical scale over which the DGR varies (i.e., one region is well represented by a single DGR value) and it covers a range of CO/H I ratios. Having chosen an appropriately

[32] Marie Curie Postdoctoral Fellow.

[33] We refer to the CO-to-H_2 conversion factor in mass units throughout this paper. Including a factor of 1.36 for helium, $X_{CO} = 2 \times 10^{20}\ cm^{-2}\ (K\ km\ s^{-1})^{-1}$ corresponds to $\alpha_{CO} = 4.35\ M_\odot\ pc^{-2}\ (K\ km\ s^{-1})^{-1}$. α_{CO} can be converted to X_{CO} units by multiplying by a factor of 4.6×10^{19}.

[34] In converting from column densities to mass surface densities, we account for helium with a factor of 1.36. For Σ_{H_2}, this factor is included in the α_{CO} term. We apply the helium correction to $\Sigma_{H\,I}$ as well.

sized region, we can determine these two constants, defining the best fit as that which produces the most uniform DGR for the multiple lines-of-sight included in the region. This technique assumes no prior value of the DGR or α_{CO}—it makes use of the linear (by definition) dependence of Σ_{H_2} on α_{CO} to identify the solution. The technique is therefore only applicable in regions where CO is detected. Constraining α_{CO} in more extreme conditions would require different techniques (see Schruba et al. 2012 for a more thorough discussion).

One useful aspect of solving simultaneously for α_{CO} and the DGR is that the absolute normalization of the dust tracer is irrelevant for the determination of α_{CO} as long as it is linear with the "true" Σ_D. Since the DGR is calibrated from the map itself, any constant term will show up in both the DGR and Σ_D and therefore has no impact on the assessment of Σ_{H_2}. For example, Leroy et al. (2011) showed that the dust optical depth at 160 μm, determined using an assumed power-law dependence on frequency and an estimate of the dust temperature from the 70 μm/160 μm ratio, works comparably well as the dust mass surface density. Dobashi et al. (2008) performed a similar study in the Large Magellanic Cloud using A_V mapping to trace dust mass surface density. Since we are also interested in the value of the DGR itself, we use Σ_D as our tracer throughout this paper. We note that uncertainties in the absolute value of Σ_D, as long as they do not introduce a nonlinearity within the region in question, will not affect the determination of α_{CO}.

For this study, we make use of CO $J = (2–1)$ observations from the large program HERA CO Line Emission Survey (HERACLES) on the IRAM 30 m telescope (Leroy et al. 2009b). It is important to note that we are therefore determining α_{CO} appropriate for that CO line. Since most studies quote α_{CO} for the CO $J = (1–0)$ line, throughout the paper we use a line ratio (R_{21}) to convert our measurements to the (1–0) scale. Systematic variations in R_{21} will result in errors in the (1–0) conversion factor, but the (2–1) conversion factor will not be affected since it is what we are directly deriving. Although it is convenient to discuss α_{CO} in its typical (1–0) incarnation, we note that the (2–1) conversion factor itself will be important for future studies with the Atacama Large Millimeter Array (ALMA). For nearby galaxies, at a given angular resolution, mapping in the (2–1) line is more efficient than in the (1–0) line. For high-redshift galaxies, the (1–0) line may be shifted out of ALMA's frequency coverage. Thus, α_{CO} for the (2–1) line will be useful regardless of its relationship to the (1–0) line.

This paper is laid out as follows. Section 2 presents the details of the resolved dust and gas observations we use. In Section 3, we describe the technique to simultaneously measure the DGR and α_{CO} and discuss how the procedure is optimized to deal with more distant galaxies than those in the Local Group (more details on the technique can be found in Appendix A). We present the results of performing the solution on 26 nearby galaxies in Section 4 and discuss their implications for our understanding of how the DGR and α_{CO} vary with metallicity and other ISM properties in Section 6.

2. OBSERVATIONS

We make use of observations of dust and gas from a series of surveys of nearby galaxies built upon the "Spitzer Infrared Nearby Galaxies Survey" (SINGS; Kennicutt et al. 2003). These observations include H I from "The H I Nearby Galaxies Survey" (THINGS; Walter et al. 2008), ^{12}CO $J = (2–1)$ from HERACLES (Leroy et al. 2009b, 2013), and far-IR dust emission from "Key Insights into Nearby Galaxies: A Far-Infrared Survey with Herschel" (KINGFISH; Kennicutt et al. 2011). In addition, several galaxies that were not included in THINGS have H I observations from either archival or new observations. The sample of galaxies in common among these surveys and for which we have detections of CO emission (see Schruba et al. 2012 for details on the HERACLES non-detections) consists of the 26 targets listed in Table 1.

The SINGS and KINGFISH surveys targeted galaxies with a variety of morphologies, located within 30 Mpc of the Milky Way. Due to the requirement of a CO detection for our work, all but one of the viable targets are spiral galaxies, the exception being NGC 3077, which is a starbursting dwarf. In Table 1, we list the positions, distances, orientation parameters, and the B-band isophotal radii at 25 mag arcsec^{-2} (R_{25}) for our targets. Throughout the text, we define $r_{25} = r/R_{25}$, where r is the galactocentric radius in units of arcminutes.

2.1. Dust Mass Surface Density

We use dust mass surface density maps derived from pixel-by-pixel modeling of the infrared (IR) spectral energy distribution (SED) observed by *Spitzer* and *Herschel* with models developed by Draine & Li (2007). A detailed description of the modeling for NGC 0628 and NGC 6946 is presented in Aniano et al. (2012) and the full-sample results are presented in G. Aniano et al. (in preparation). The dust models include a description of the dust properties (size distribution, composition, and optical properties of the grains) with a variable fraction of dust in the form of polycyclic aromatic hydrocarbons (PAHs). The dust is illuminated by a radiation field distribution wherein a fraction of the dust is heated by a minimum radiation field U_{min} while the rest is heated by a power-law distribution of radiation fields extending up to $U = 10^7\ U_{MMP}$, where U_{MMP} is the solar neighborhood radiation field from Mathis et al. (1983). The fraction of the dust mass heated by radiation fields where $U > 10^2\ U_{MMP}$ is typically very small, so the dust mass surface density is not very sensitive to the exact value of the upper limit on U.

The resolution of the dust mass surface density map is equivalent to that of the lowest resolution IR map included in the modeling. In order to preserve spatial resolution while still covering the peak of the dust SED, we use the dust modeling at a resolution matched to the SPIRE 350 μm map (FWHM $\sim 25''$). This limiting resolution allows us to include the following maps in the dust modeling: IRAC 3.6, 4.5, 5.8, and 8.0 μm; MIPS 24 and 70 μm; PACS 70, 100, and 160 μm; and SPIRE 250 and 350 μm. In theory, we could perform this analysis at even higher resolution using the SPIRE 250 resolution maps, which include all IRAC bands; MIPS 24 μm; all PACS bands; and SPIRE 250 μm. However, Aniano et al. (2012) found that maps where the limiting resolution exceeds MIPS 70 μm are less reliable due to the comparatively low surface brightness sensitivity of the PACS observations. At SPIRE 250 μm resolution, they find systematic errors of up to $\sim$30%–40% in the dust mass (compared to their best estimate, which includes all IRAC, MIPS, PACS, and SPIRE bands). However, when both SPIRE 250 μm and 350 μm observations are included, the systematic errors in the dust mass are $\sim$10% or less. We proceed by using the SPIRE 350 μm resolution dust modeling results.

Aside from the dust mass surface density, the Aniano et al. (2012) modeling also constrains a number of other quantities that we make use of later in interpreting the results. These quantities include $\overline{U}$, the average radiation field heating the dust; U_{min}, the minimum radiation field; f_{PDR}, the fraction of the dust luminosity that comes from dust heated by

Table 1
Galaxy Sample

Galaxy	R.A. (J2000)	Decl. (J2000)	Distance (Mpc)	i (°)	P.A. (°)	Morphology	R_{25} (′)	Solution Pixel[a] Radius (kpc)
NGC 0337	$00^h59^m50^s.1$	−07°34′41″.0	19.3	51	90	SBd	1.5	3.5
NGC 0628	$01^h36^m41^s.8$	+15°47′00″.0	7.2	7	20	SAc	4.9	1.3
NGC 0925	$02^h27^m16^s.5$	+33°34′43″.5	9.1	66	287	SABd	5.4	1.7
NGC 2841	$09^h22^m02^s.6$	+50°58′35″.2	14.1	74	153	SAb	3.5	2.6
NGC 2976	$09^h47^m15^s.3$	+67°55′00″.0	3.6	65	335	SAc	3.6	0.6
NGC 3077	$10^h03^m19^s.1$	+68°44′02″.0	3.8	46	45	I0pec	2.7	0.7
NGC 3184*	$10^h18^m17^s.0$	+41°25′28″.0	11.7	16	179	SABcd	3.7	2.1
NGC 3198	$10^h19^m55^s.0$	+45°32′58″.9	14.1	72	215	SBc	3.2	2.6
NGC 3351*	$10^h43^m57^s.7$	+11°42′14″.0	9.3	41	192	SBb	3.6	1.7
NGC 3521*	$11^h05^m48^s.6$	−00°02′09″.2	11.2	73	340	SABbc	4.2	2.0
NGC 3627*	$11^h20^m15^s.0$	+12°59′29″.6	9.4	62	173	SABb	5.1	1.7
NGC 3938	$11^h52^m49^s.4$	+44°07′14″.9	17.9	14	195	SAc	1.8	3.3
NGC 4236	$12^h16^m42^s.1$	+69°27′45″.0	4.5	75	162	SBdm	12.0	0.8
NGC 4254*	$12^h18^m49^s.6$	+14°24′59″.0	14.4	32	55	SAc	2.5	2.6
NGC 4321*	$12^h22^m54^s.9$	+15°49′21″.0	14.3	30	153	SABbc	3.0	2.6
NGC 4536*	$12^h34^m27^s.1$	+02°11′16″.0	14.5	59	299	SABbc	3.5	2.6
NGC 4569*	$12^h36^m49^s.8$	+13°09′46″.0	9.9	66	23	SABab	4.6	1.8
NGC 4625	$12^h41^m52^s.7$	+41°16′26″.0	9.3	47	330	SABmp	0.7	1.7
NGC 4631	$12^h42^m08^s.0$	+32°32′29″.0	7.6	85	86	SBd	7.3	1.4
NGC 4725	$12^h50^m26^s.6$	+25°30′03″.0	11.9	54	36	SABab	4.9	2.2
NGC 4736*	$12^h50^m53^s.0$	+41°07′13″.2	4.7	41	296	SAab	3.9	0.8
NGC 5055*	$13^h15^m49^s.2$	+42°01′45″.3	7.9	59	102	SAbc	5.9	1.4
NGC 5457[b]*	$14^h03^m12^s.6$	+54°20′57″.0	6.7	18	39	SABcd	12.0	1.2
NGC 5713	$14^h40^m11^s.5$	−00°17′21″.0	21.4	48	11	SABbcp	1.2	3.9
NGC 6946*	$20^h34^m52^s.2$	+60°09′14″.4	6.8	33	243	SABcd	5.7	1.2
NGC 7331	$22^h37^m04^s.0$	+34°24′56″.5	14.5	76	168	SAb	4.6	2.6

Notes. Distances and morphologies from the compilation of Kennicutt et al. (2011). Orientation parameters are from Walter et al. (2008) where possible, and are otherwise from the LEDA and NED databases.

[a] Solution pixels are defined in Section 3. They are the regions in which we solve for α_{CO} and the DGR.

[b] M101.

* CO $J = (1–0)$ maps available from the Nobeyama survey of nearby galaxies (Kuno et al. 2007).

$U > 100\ U_{MMP}$; and q_{PAH}, the fraction of the dust mass accounted for by PAHs with fewer than 10^3 carbon atoms.

Statistical uncertainties on Σ_D and the other derived parameters were measured by Aniano et al. (2012) with a Monte Carlo approach. In most of the regions we consider, the statistical uncertainties on the dust mass surface densities are small, but the signal-to-noise ratio (S/N) of the dust mass maps is generally a function of radius and the outskirts can have S/N ∼ 5 in some cases. Our error estimates take these uncertainties into account and are described in Section 3.3. Possible systematic effects are discussed in Section 3.5.

2.2. H I Surface Density

To trace the atomic gas surface density in our targets, we use a combination of NRAO[35] Very Large Array (VLA) H I observations from THINGS (Walter et al. 2008) and supplementary H I, observations both new and archival, described in Leroy et al. (2013). The source and angular resolution of the H I maps for our targets are listed in Table 2.

The H I maps were converted from integrated intensities to column densities using Equation (5) of Walter et al. (2008). We convolved each map with an elliptical Gaussian kernel determined by its individual beam properties to produce a circular Gaussian point spread function (PSF). We then use kernels created following the procedures in Aniano et al. (2011) to convolve the circular Gaussian to match the SPIRE PSF at 350 μm. For the H I, we assume the uncertainties to be the larger of either 0.5 $M_\odot$ pc^{-2} or 10% of the measured column density. Systematic uncertainties from H I opacity effects are discussed in Section 3.4.

2.3. CO Integrated Intensity

To trace the molecular gas distribution in our targets, we use CO $J = (2–1)$ mapping from the HERACLES survey (Leroy et al. 2009b). Integrated intensity maps were generated from the CO spectral cubes by integrating the spectra over a range in velocity around either (1) the detected CO line in that spectrum or (2) the expected CO velocity predicted from the H I velocity (since H I is detected at high S/N in almost all relevant pixels). We propagate uncertainties through these masking steps, creating in the end an integrated CO line map and an uncertainty map. The HERACLES maps have PSFs well approximated by a circular Gaussian with a FWHM of 13″.4. We convolve the maps with kernels constructed using the techniques described by Aniano et al. (2011) to match the resolution of the SPIRE 350 μm maps. We have tested the effect of error beams (i.e., the extended wings of the PSF or stray light pick-up of the IRAM 30 m telescope) on the HERACLES maps and find that the effect is less than ∼5% for all galaxies and closer to 1% for most.

Our measurements of α_{CO} directly determine the conversion factor appropriate for CO $J = (2–1)$. However, to compare with the standard CO $J = (1–0)$ factor, which is more frequently

[35] The National Radio Astronomy Observatory is a facility of the National Science Foundation operated under cooperative agreement by Associated Universities, Inc.

Table 2
H I Observation Summary

Galaxy	Source	FWHM Beam Properties		
		Major (″)	Minor (″)	P.A. (°)
NGC 0337	Archival	20.2	13.0	160.3
NGC 0628	THINGS	11.9	9.3	−70.3
NGC 0925	THINGS	5.9	5.7	30.6
NGC 2841	THINGS	11.1	9.4	−12.3
NGC 2976	THINGS	7.4	6.4	71.8
NGC 3077	THINGS	14.3	13.2	60.5
NGC 3184	THINGS	7.5	6.9	85.4
NGC 3198	THINGS	11.4	9.4	−80.4
NGC 3351	THINGS	9.9	7.1	24.1
NGC 3521	THINGS	14.1	11.2	−61.7
NGC 3938	Archival	18.5	18.2	48.6
NGC 3627	THINGS	10.0	8.9	−60.9
NGC 4236	New	16.7	13.9	69.6
NGC 4254	Archival	16.9	16.2	54.4
NGC 4321	Archival	14.7	14.1	163.4
NGC 4536	Archival, New	14.7	13.8	−11.4
NGC 4569	Archival	14.2	13.9	32.9
NGC 4625	Archival	13.0	12.5	−29.2
NGC 4631	Archival	14.9	13.3	178.1
NGC 4725	Archival, New	18.6	17.0	−20.9
NGC 4736	THINGS	10.2	9.1	−23.0
NGC 5055	THINGS	10.1	8.7	−40.0
NGC 5457	THINGS	10.8	10.2	−67.1
NGC 5713	Archival	15.5	14.9	121.9
NGC 6946	THINGS	6.0	5.6	6.6
NGC 7331	THINGS	6.1	5.6	34.3

Note. Galaxies with new H I data were observed in VLA project AL735 (PI: A. Leroy).

used, we convert to (1–0) using a fixed value of the line ratio $R_{21} = (2\text{–}1)/(1\text{–}0) = 0.7$. Due to revised telescope efficiencies, the R_{21} we use differs slightly from that used in Leroy et al. (2009b). The R_{21} we assume was found to be an appropriate average for the HERACLES sample (E. W. Rosolowsky et al., in preparation; note that we find good agreement with this R_{21} by comparing the HERACLES measurements with published CO $J = (1\text{–}0)$ measurements as described in the Appendix). We discuss the effects of assuming a fixed R_{21} on our results for the (1–0) conversion factor in Section 3.4. In order to use the α_{CO} values with CO $J = (2\text{–}1)$ observations, they should be divided by a factor of 0.7.

2.4. Ancillary Datasets

2.4.1. Metallicity

In the analysis presented in Section 4, we study the variations of α_{CO} and the DGR as a function of metallicity. Wherever possible, we make use of the metallicity measurements from Moustakas et al. (2010, hereafter M10), who derived characteristic metallicities as well as radial gradients in oxygen abundance for the SINGS sample. M10 present results using two different calibrations for the strong-line abundances—from Kobulnicky & Kewley (2004, KK04) and Pilyugin & Thuan (2005, PT05). Both calibrations are considered in the following analysis.

Our preferred metallicity measurement is a radial gradient from H II region metallicities (M10, Table 8). For several galaxies, no radial gradient measurement is available, so we use a fixed metallicity for the entire galaxy equal to the "characteristic metallicity" (M10, Table 9). In the case of NGC 4236 and 4569, the only metallicity measurements available are from the B-band luminosity–metallicity (L–Z) relationship and we use those values from M10 with no gradient. Finally, two of our galaxies are not in the M10 sample. For NGC 3077, we use the metallicity 12+log(O/H) = 8.9 given in KK04 with no gradient, from Calzetti et al. (1994). To obtain a PT05 measurement for NGC 3077, we subtract 0.6 dex, the average offset between the two calibrations found by M10. For NGC 5457 (a.k.a. M 101), a galaxy with a well-known radial metallicity gradient, we use the measurements from Bresolin (2007). These metallicities are from direct methods, so are not on the same scale as the measurements from either PT05 or KK04. The metallicities and gradients we use are listed in Table 3. These values are converted to match the r_{25} values we adopt in this work, which can be slightly different from those adopted by M10. In order to compare with the MW, we use the metallicity of the Orion Nebula H II region in the PT05 and KK04 calibrations, i.e., 12+log(O/H) = 8.5 for PT05 and 8.8 for KK04, which were obtained by applying the strong-line metallicity calibrations to the integrated spectrum of Orion from integral field spectroscopy[36] (Sánchez et al. 2007).

2.4.2. Star Formation Rate and Stellar Mass Surface Density Maps

The star formation rate (SFR) surface densities (Σ_{SFR}) are calculated from Hα and 24 μm maps using the Hα maps and the procedure described in Leroy et al. (2012). The Hα maps have been convolved to match the SPIRE 350 μm PSF assuming an initial ∼1″–2″ FWHM Gaussian PSF, although the large difference between the initial and final PSF makes this choice mostly irrelevant. We use 24 μm maps from SINGS, processed (background subtracted, convolved, and aligned) as described in Aniano et al. (2012). The Aniano et al. (2012) modeling results described in Section 2.1 are also used to remove a cirrus component unrelated to star formation from the 24 μm map, as described in Leroy et al. (2012).

We calculate the stellar mass surface density (Σ_*) from the IRAC 3.6 μm observations from SINGS, as described in Leroy et al. (2008). These calculations provide only a rough tracer of stellar mass surface density, since we do not take into account corrections for various contaminants in the 3.6 μm band (Zibetti & Groves 2011; Meidt et al. 2012).

2.5. Processing

After all maps have been convolved to the SPIRE 350 μm resolution, we sample them with a hexagonal grid with approximately half-beam spacings (i.e., 12.″5). Uncertainties in the dust mass surface density, CO integrated intensity, and H I column density are propagated through the necessary convolutions and samplings. Surface densities and other quantities have been deprojected using the orientation parameters listed in Table 1.

3. SOLVING SIMULTANEOUSLY FOR α_{CO} AND THE DGR

In order to use the dust mass surface density to trace the total gas mass surface density, we assume (1) that dust and gas are well mixed (i.e., that Equation (3) holds), (2) that the DGR is constant on ∼kiloparsec scales in our target galaxies, and (3) within a given ∼kiloparsec region, the DGR does not change between the atomic and molecular phases. Then, given multiple measurements of Σ_D, $\Sigma_{H\,I}$, and I_{CO} that span a range of CO/H I values in a kiloparsec-scale region of a galaxy, we can adjust α_{CO} until we find the value that returns the most uniform DGR for the region. This procedure makes no assumption about the value of the DGR, only that it is constant in that region. In

[36] Data available at http://www.caha.es/sanchez/orion/.

Table 3
Adopted Metallicities and Gradients

Galaxy	PT05 Central Metallicity (12 + log(O/H))	PT05 Metallicity Gradient (dex r_{25}^{-1})	KK04 Central Metallicity (12 + log(O/H))	KK04 Metallicity Gradient (dex r_{25}^{-1})	Source
NGC 0337	8.18 ± 0.07	···	8.84 ± 0.05	···	M10 Table 9
NGC 0628	8.43 ± 0.02	-0.25 ± 0.05	9.19 ± 0.02	-0.54 ± 0.04	M10 Table 8
NGC 0925	8.32 ± 0.01	-0.21 ± 0.03	8.91 ± 0.01	-0.43 ± 0.02	M10 Table 8
NGC 2841	8.72 ± 0.12	-0.54 ± 0.39	9.34 ± 0.07	-0.36 ± 0.24	M10 Table 8
NGC 2976	8.36 ± 0.06	···	8.98 ± 0.03	···	M10 Table 9
NGC 3077	8.30 ± 0.20	···	8.90 ± 0.20	···	K11
NGC 3184	8.65 ± 0.02	-0.46 ± 0.06	9.30 ± 0.02	-0.52 ± 0.05	M10 Table 8
NGC 3198	8.49 ± 0.04	-0.38 ± 0.11	9.10 ± 0.03	-0.50 ± 0.08	M10 Table 8
NGC 3351	8.69 ± 0.01	-0.27 ± 0.04	9.24 ± 0.01	-0.15 ± 0.03	M10 Table 8
NGC 3521	8.44 ± 0.05	-0.12 ± 0.25	9.20 ± 0.03	-0.52 ± 0.15	M10 Table 8
NGC 3627	8.34 ± 0.24	···	8.99 ± 0.10	···	M10 Table 9
NGC 3938	8.42 ± 0.20	···	9.06 ± 0.20	···	M10 *L–Z*
NGC 4236	8.17 ± 0.20	···	8.74 ± 0.20	···	M10 *L–Z*
NGC 4254	8.56 ± 0.02	-0.35 ± 0.08	9.26 ± 0.02	-0.39 ± 0.06	M10 Table 8
NGC 4321	8.61 ± 0.07	-0.31 ± 0.17	9.29 ± 0.04	-0.28 ± 0.11	M10 Table 8
NGC 4536	8.21 ± 0.08	···	9.00 ± 0.04	···	M10 Table 9
NGC 4569	8.58 ± 0.20	···	9.26 ± 0.20	···	M10 *L–Z*
NGC 4625	8.35 ± 0.17	···	9.05 ± 0.07	···	M10 Table 9
NGC 4631	8.12 ± 0.11	···	8.75 ± 0.09	···	M10 Table 9
NGC 4725	8.35 ± 0.13	···	9.10 ± 0.08	···	M10 Table 9
NGC 4736	8.40 ± 0.01	-0.23 ± 0.12	9.04 ± 0.01	-0.08 ± 0.10	M10 Table 8
NGC 5055	8.59 ± 0.07	-0.59 ± 0.27	9.30 ± 0.04	-0.51 ± 0.17	M10 Table 8
NGC 5457	8.75 ± 0.05	-0.75 ± 0.06	8.75 ± 0.05	-0.75 ± 0.07	B07
NGC 5713	8.48 ± 0.10	···	9.08 ± 0.03	···	M10 Table 9
NGC 6946	8.45 ± 0.06	-0.17 ± 0.15	9.13 ± 0.04	-0.28 ± 0.10	M10 Table 8
NGC 7331	8.41 ± 0.06	-0.21 ± 0.31	9.18 ± 0.05	-0.49 ± 0.25	M10 Table 8

References. Moustakas et al. (2010, M10), Kennicutt et al. (2011, K11), Bresolin (2007, B07).

addition, this procedure makes no presumptions about the value of α_{CO} or the scales over which it varies. If α_{CO} varies on small scales, our measured α_{CO} value will represent the dust (or gas) mass surface density weighted average α_{CO} for the region. We discuss this process in detail in the following sections.

A simultaneous solution for α_{CO} and the DGR can only be performed if a range of CO/H I ratios are present in the measurements. The linear dependence of Σ_{H_2} on α_{CO} provides leverage to adjust α_{CO} in order to best describe all of the points with the same DGR over a range of CO/H I ratios. An "incorrect" α_{CO} value will result in a dependence of the measured DGR on the CO/H I ratio, increasing the spread in the DGR values in the region. An illustration of this effect is shown in panel (c) of Figure 1. Finding a solution or best-fit α_{CO} is equivalent to locating a minimum in the DGR scatter at a given value of α_{CO}.

The basic procedure we use minimizing the scatter in the DGR values in the region was suggested by Leroy et al. (2011). There are, however, a variety of other techniques to solve for α_{CO} and the DGR given multiple measurements, including directly fitting a plane to I_{CO}, Σ_D, and $\Sigma_{H\,I}$. It is not clear a priori which scatter minimization technique is optimal, so we performed a set of simulations, described in the Appendix, to test various techniques and optimize the procedure for our dataset and objectives. We describe the resulting scatter minimization procedure in more detail below.

3.1. Defining the "Solution Pixel"

To perform the solution, we require multiple measurements of dust and gas tracers in the region. We also aim, however, to select the smallest possible regions, in order to ensure an approximately constant DGR. We proceed by dividing each target galaxy into hexagonal regions encompassing 37 of the half-beam spaced sampling points. We call these regions "solution pixels" (see panel (a) of Figure 1 for an example). The 37-point solution pixels are a compromise between small region sizes and a sufficient number of independent measurements needed to minimize statistical noise. The solution pixels tile the galaxy with center-to-center spacing of 37.″5. Thus, neighboring solution pixels are not independent and share ∼40% of their sampling points. The overlap between solution pixels is illustrated in Figure 1. Such a tiling is optimal because it fully samples the data. To ensure that the final results are not dependent on the placement of the solution pixels, we performed a test where we distributed the solution pixels randomly throughout the galaxies and compared the resulting radial trends in α_{CO} to what we measured using the fixed grid described above. The radial trends were in agreement, demonstrating that our results are insensitive to the exact placement of the solution pixel grid. The solution pixels correspond to physical scales ranging from ∼0.6 kpc to 3.9 kpc. We have tiled each galaxy with solution pixels out to the maximum value of r_{25} contained in the HERACLES maps.

3.2. Minimizing the DGR Scatter

For each sampling point i in the solution pixel, the measurements of $\Sigma_{D,i}$, $\Sigma_{H\,I,i}$, and $I_{CO,i}$, along with an assumed α_{CO}, determine the DGR$_i$. We step through a grid of α_{CO} values to find the α_{CO} that results in the most uniform DGR for all the DGR$_i$ values in the solution pixel. In all solutions presented

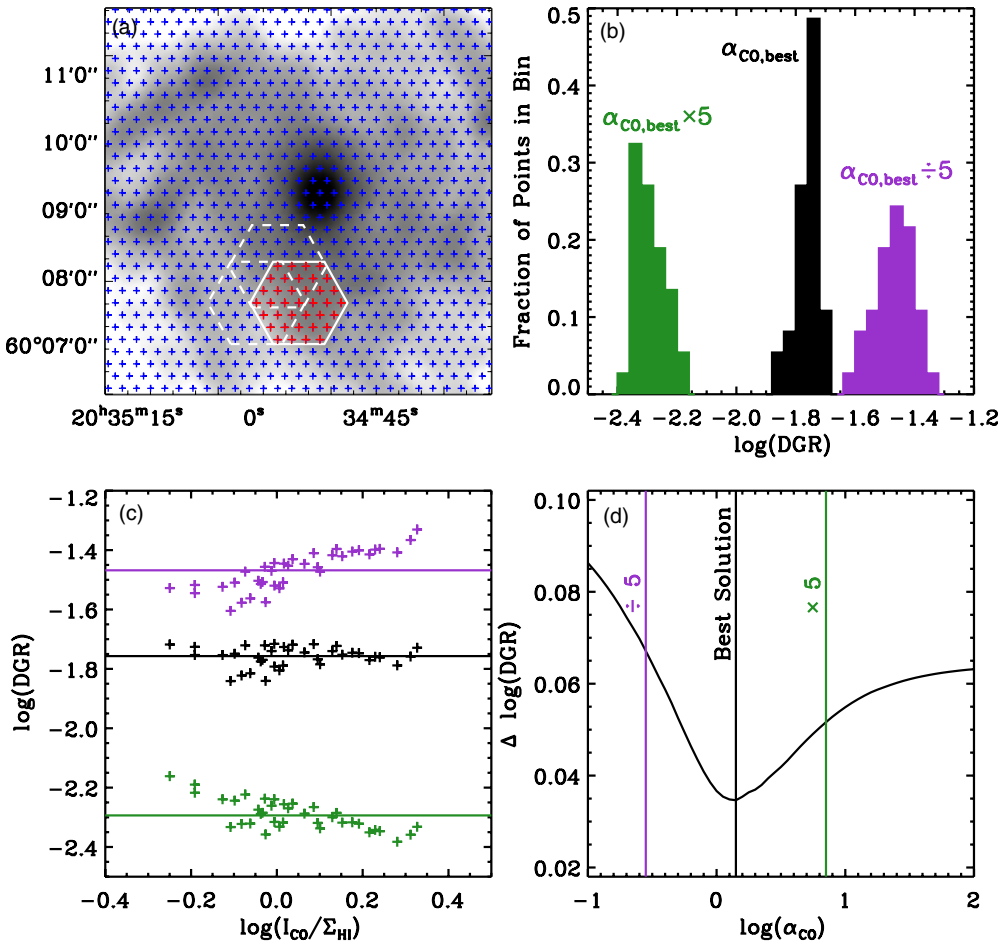

Figure 1. Illustration of the technique to determine the DGR and α_{CO} for a single solution pixel in NGC 6946. Panel (a) shows a portion of the CO map from HERACLES overlaid with the half-beam spaced sampling grid. The solution pixel in question is shown with a solid white hexagon and the 37 individual sampling points included in the solution are shown in red. Two neighboring solution pixels are also highlighted with a dashed white line to show how the pixels are arranged and that neighboring solution pixels share ~40% of their sampling points. Panel (b) illustrates that the scatter in the DGR changes as a function of α_{CO}. Here, we have plotted histograms of the measured DGR_i values in this solution pixel at three different values of α_{CO} (the optimal value in black and a factor of five above and below this value in green and purple, respectively). Panel (c) illustrates that this scatter originates from the variation of the DGR as a function of CO/H I when α_{CO} is not at the optimal value. We show this effect by plotting the 37 DGR_i values as a function of CO/H I ratio for the same three α_{CO} values shown in panel (b). The horizontal lines indicate the mean DGR for each set of points. The slope in the DGR vs. CO/H I space is minimized at the optimal α_{CO}. Finally, in panel (d), we show the scatter in the DGR at each value of the full α_{CO} grid shown in black. The three highlighted α_{CO} values are marked with vertical lines. Panel (d) highlights the fact that the DGR scatter is minimized at the best-fit $\log(\alpha_{CO}) = 0.15 \pm 0.22$ in this region. The minimization of the scatter in log(DGR), as shown in panel (d), is the technique we have determined to be the most effective for determining α_{CO} and the DGR, using tests that are described in detail in the Appendix.

(A color version of this figure is available in the online journal.)

here, we use an α_{CO} grid with 0.05 dex spacing, spanning the range $\alpha_{CO} = 0.1$–$100\ M_\odot\ pc^{-2}\ (K\ km\ s^{-1})^{-1}$.

We determine the most "uniform" DGR in a solution pixel by minimizing the scatter in the DGR_i values as a function of α_{CO}. The scatter is measured with a robust estimator of the standard deviation[37] of the logarithm of the DGR_i values—this technique appears to work best because outliers have little effect on the measured scatter because of both the logarithmic units and the outlier suppression. After measuring the scatter in the DGR at every α_{CO} value, we find the α_{CO} at which the scatter ($\Delta\log(DGR)$) is minimized. This value is taken to be our best-fit α_{CO} value for the region. We consider a solution to be found when a minimum has been located in the DGR scatter within the range of our α_{CO} grid. This outcome does not occur in every solution pixel—some pixels do not have sufficient CO/H I contrast, others have too low S/N, and, for some, the minimum is at the edge of the allowable range and the solution is not well constrained. The failed solutions are not included in our further analysis.

An illustration of the technique is shown in Figure 1 for a region in NGC 6946. In panel (a), we show the HERACLES CO $J = (2$–$1)$ map of the galaxy with our half-beam sampling grid; the hexagonal region shows the "solution pixel" in question, which includes 37 individual samples from the maps. Panels (b) and (c) show how varying α_{CO} affects the mean DGR and the scatter for the points in the region, illustrating how the scatter increases away from the best α_{CO} value. Panel (d) shows the scatter as a function of α_{CO} for the whole α_{CO} grid. A clear minimum exists for this solution pixel at $\alpha_{CO} \sim 1.4\ M_\odot\ pc^{-2}\ (K\ km\ s^{-1})^{-1}$.

3.3. Statistical Uncertainties on α_{CO} and the DGR

We judge the uncertainties on the "best-fit" α_{CO} and the DGR in several ways. First, to take into account statistical errors, we perform a Monte Carlo test on the solutions by adding random noise to our measured Σ_D, Σ_{HI}, and I_{CO} values according to each

[37] We use the IDL implementation of Tukey's biweight mean (Press et al. 2002) biweight_mean.pro.

point's measurement errors. We repeat the solution with the randomly perturbed data values 100 times and find the standard deviation of the results. We also perform a "bootstrapping" trial, which tests the sensitivity of each solution to individual measurements. In each bootstrap iteration for a given solution pixel, we randomly select 37 sampling points, with replacement, and derive the solution. The bootstrap procedure is repeated 100 times for each solution pixel and we measure the resulting standard deviation of the α_{CO} values. The standard deviations from the Monte Carlo and bootstrapping iterations are added in quadrature to produce the final quoted error for the α_{CO} values we determine. In addition, to check these uncertainties, we also estimate the scatter and bias in α_{CO} for the given technique from our simulated data trials described in the Appendix, based on the median CO S/N in the solution pixel and the measured minimum of Δlog(DGR). The uncertainties from Monte Carlo plus bootstrapping are comparable to what we expect given the simulated data trials.

3.4. Systematic Uncertainties on α_{CO}

3.4.1. Uncertainties on α_{CO} from R_{21} Variations

In the following, we report α_{CO} appropriate for the (1–0) line, since it is the canonical CO-to-H_2 conversion factor that most observational and theoretical studies utilize. To do so, we have converted between (2–1) (which we have directly measured) and (1–0) using a fixed line ratio $R_{21} = 0.7$. Deviations from this R_{21} value will result in systematic offsets in the (1–0) conversion factor, while the (2–1) conversion factor will be unaffected since it is what we have directly measured. To quantify any (1–0) α_{CO} offsets, we have investigated the variability of R_{21} in those galaxies with publicly available CO $J = (1–0)$ maps from the Nobeyama survey of nearby spiral galaxies (Kuno et al. 2007). Galaxies that have Nobeyama maps are marked with an asterisk in Table 1. The details of this comparison can be found in the Appendix. We find that deviations from $R_{21} = 0.7$ can cause small systematic shifts in α_{CO} appropriate for the (1–0) line, but the magnitude of the shifts are generally within the uncertainties on the α_{CO} solutions (i.e., typically less than 0.2 dex). We note that variations of R_{21} within a pixel would introduce additional systematic uncertainties on α_{CO}.

3.4.2. Variations of Σ_D Linearity within Solution Pixels

We assume that the dust tracer we employ (Σ_D) linearly tracks the true dust mass surface density in a solution pixel. Because we calibrate the DGR based on the values of Σ_D within each pixel, any multiplicative constant term cancels out in Equation (3) and does not affect the measurement of α_{CO}. Nonlinearities in Σ_D that are uncorrelated with the atomic/molecular phase add scatter to our measurements of α_{CO} but do not introduce systematic errors. In the following, we discuss several sources of nonlinearity in Σ_D that are correlated with the ISM phase and estimate their systematic error contribution.

1. *Variation of dust emissivity.* A variety of observations have suggested that dust emissivity increases in molecular gas relative to atomic gas (note, however, that most of the studies use CO to trace molecular gas and may interpret variations in α_{CO} as changes in emissivity). Recent work has suggested that the dust emissivity increases by a factor of $\sim$2 between the atomic and molecular ISM (Planck Collaboration et al. 2011a; Martin et al. 2012). If the dust in molecular regions has a higher emissivity, Σ_D will overestimate the amount of dust there, causing us to overestimate the amount of gas. In that case, we would recover a higher α_{CO} than actually exists. As a first approximation, our measured α_{CO} would be too high by the change in emissivity between atomic and molecular phases, a factor of $\sim$2 based on the previously discussed results.
2. *Variation of the DGR.* Evidence from the depletion of gas phase metals in the MW suggests that the DGR increases as a function of the H_2 fraction. To estimate the magnitude of such effects, we use the results of Jenkins (2009). From the minimum level of depletion measured in the MW to complete depletion of all heavy elements, the DGR varies by a factor of four. A large fraction of this change in the DGR comes from the depletion of oxygen, however, which may not predominantly be incorporated into dust as it is depleted (see the discussion in Section 10.1.4 of Jenkins 2009). Excluding oxygen, the possible change in the DGR is a factor of two. Using the correlation between the depletion and the H_2 fraction from Figure 16 of Jenkins (2009), we find that for 10%–100% H_2 fractions (as are appropriate for our regions), the possible variation in the DGR is a factor of two (or less, depending on the contribution of oxygen). As in the case of dust emissivity variations, the effect of the DGR increasing in molecular gas would be to artificially increase our measured α_{CO} by the same factor as the increase in the DGR.
3. *Systematic biases in measuring Σ_D from SED modeling.* Because warm dust will radiate more strongly per unit mass than cold dust at all wavelengths, the SED will not clearly reflect the presence of cold dust unless it dominates the mass. This fact means that the SED fitting technique is not sensitive to cold dust contained in giant molecular cloud (GMC) interiors ($A_V \gtrsim 1$) at our spatial resolution. The fraction of the dust mass in these interiors, assuming a spherical cloud with uniform density and total $A_V \approx 8$ mag, is $\sim$40%; this estimate agrees well with the recent extinction mapping measurements of MW GMCs of Kainulainen et al. (2011) and Lombardi et al. (2011). If we underestimate the mass of dust by missing cold dust in GMC interiors, we would underestimate the amount of molecular gas and adjust α_{CO} downward. The magnitude of this effect is at a factor of $\sim$2 level and is opposite in direction to what we expect for dust emissivity or the DGR increase in molecular clouds.

To summarize, variations of the DGR and dust emissivity between atomic/molecular gas could both bias our α_{CO} results toward higher values by factors of $\sim$2. Systematic biases in accounting for cold dust in the SED modeling act in the opposite direction (i.e., biasing α_{CO} toward lower values), also by a factor of $\sim$2.

3.4.3. Opaque H I

The H I maps we use have not been corrected for any optical depth effects (Walter et al. 2008). H I observations of M31 at high spatial and spectral resolution have suggested there may be large local opacity corrections on 50 pc scales (Braun et al. 2009). To estimate the importance of any opaque H I, we have used the corrected and uncorrected maps of M31, provided to us by R. Braun. Convolving to 500 pc spatial resolution, the average resolution element in M31 has a 20% correction to the H I column density. Choosing only regions with $N_H > 10^{21}$ cm^{-2}, the average correction is $\sim$30%. Essentially all resolution elements have opacity corrections less than a factor of two.

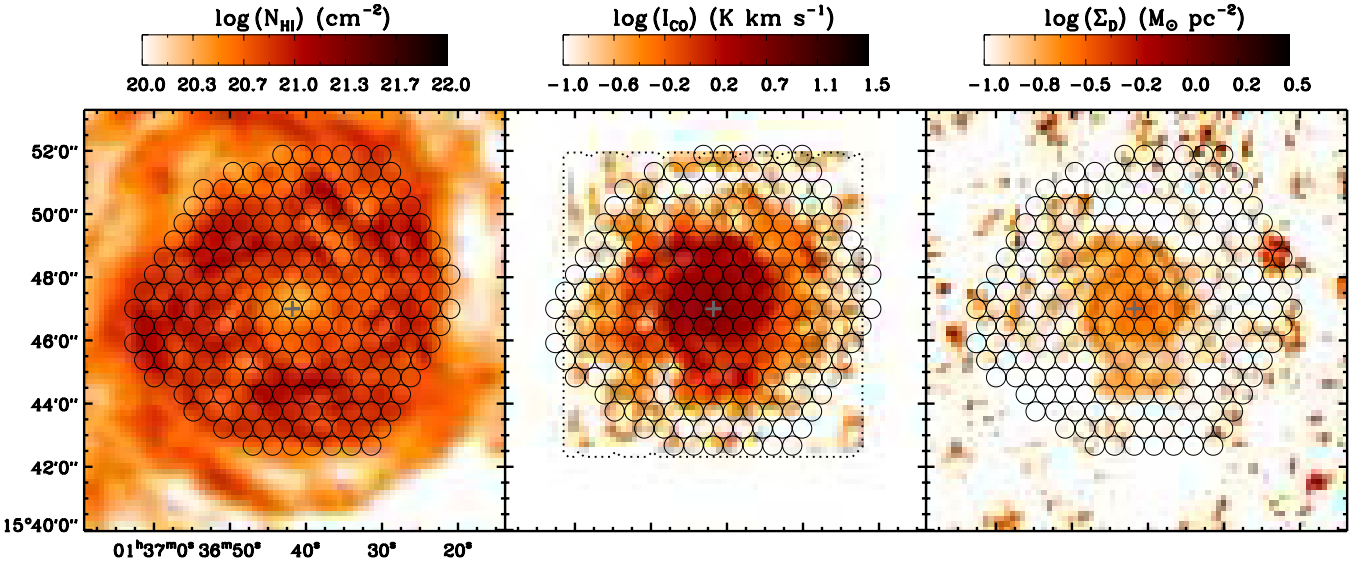

Figure 2. H I, CO, and Σ_D maps for NGC 0628, from left to right ($D = 7.2$ Mpc; $1'' = 35$ pc). The centers of the pixels in which we perform the simultaneous α_{CO} and DGR solutions are shown as circles overlaid on the images. The gray cross in each panel shows the central solution pixel for the galaxy. In the middle panel, the coverage of the HERACLES CO map is shown with a dotted line. Similar plots for all galaxies in the sample can be found in the Appendix.

(A color version of this figure is available in the online journal.)

If opaque H I exists at the level Braun et al. (2009) found in M31, it would have two main effects on our solutions for α_{CO}. First, on average, the optically thin estimate for the atomic gas mass would be too low, resulting in our procedure determining a DGR that is too high (excess dust compared to the amount of gas). In the molecular regions, then, we will expect too much gas based on that same DGR, and consequently artificially increase α_{CO}. Second, since the opaque H I features do not appear to be spatially associated with molecular gas (see Braun et al. 2009, Section 4.1, for a further discussion), these features will act as a source of intrinsic scatter in the DGR. In the Appendix, we explore the effect of intrinsic scatter on our solution technique. At the level of opaque H I in M31, we do not find an appreciable bias in the recovered α_{CO} due to scatter. We expect the magnitude of the systematic effects due to opaque H I, if it exists, to be well within the statistical uncertainties we achieve on the α_{CO} measurements.

3.5. Systematic Uncertainties on the DGR

3.5.1. Absolute Calibration of Σ_D

As we have discussed above, as long as Σ_D is a linear tracer of the true dust mass surface density within a given solution pixel, its absolute calibration has no effect on the α_{CO} value we measure. The same is not true for the DGR value. Any uncertainties on the calibration of Σ_D will be directly reflected in the DGR measurement. The Σ_D values we used are from fits of the Draine & Li (2007) models to the IR SED using the MW $R_V = 3.1$ grain model. The extent to which the appropriate dust emissivity κ_ν deviates from the value used by this model represents a systematic uncertainty on the DGR values we derive. Our knowledge of κ_ν in different environments is limited, but there are constraints from observations of dust extinction curves and depletions in the Large Magellanic Cloud (LMC) and Small Magellanic Cloud (SMC; cf. Weingartner & Draine 2001), where measured R_V values can deviate significantly from the canonical value of 3.1. Draine et al. (2007) demonstrated that the Σ_D values decreased by a factor of $\sim$1.2 when the LMC or SMC dust model was used instead of the MW $R_V = 3.1$ model. Given that our sample is largely dominated by spiral galaxies and hence does not probe environments with metallicities comparable to those of the SMC (due to the faintness of CO in such regions and our S/N limitations), we expect that the systematic uncertainties on our DGR when comparing with other results from Draine & Li (2007) model fits is small. It is important to note, however, that different dust models, even fit to the same $R_V = 3.1$ extinction curve, have systematic offsets in their dust mass predictions due to different grain size distributions, grain composition, etc. Therefore, the comparison of our DGR values to results from studies not using the Draine & Li (2007) models will show systematic offsets.

4. RESULTS

4.1. NGC 0628 Results Example

We divided each of the 26 galaxies in our sample into solution pixels and performed the simultaneous solution for the DGR and α_{CO} in each pixel. As an example, we present the results for NGC 0628 in the following section. The results for all solution pixels in all galaxies can be found in the Appendix.

Figure 2 shows, from left to right, the H I, CO, and Σ_D maps used in our analysis. The circles overlaid on the maps represent the centers of the solution pixels we have defined. Figure 3 shows the same circles representing the solution pixel centers. The left panel shows the pixel centers now filled in with a color representing the best α_{CO} solution for that pixel. In the middle panel, a gray scale shows the uncertainty on that α_{CO} solution. The DGR values are shown in the panel on the right. Finally, in Figure 4, we show these measured α_{CO} values as a function of galactocentric radius (r_{25}). For comparison, Figure 4 also shows the local MW $\alpha_{CO} = 4.4\ M_\odot\ \mathrm{pc}^{-2}\ (\mathrm{K\ km\ s}^{-1})^{-1}$ value with a solid horizontal line (dotted lines show a factor of two above and below; see Section 5.1 for details on the measurement of the MW value). We note that the MW may show a gradient of α_{CO} with radius (also discussed in Section 5.1), but for purposes of comparison with the most widely used conversion factor, we use a constant α_{CO} on all plots.

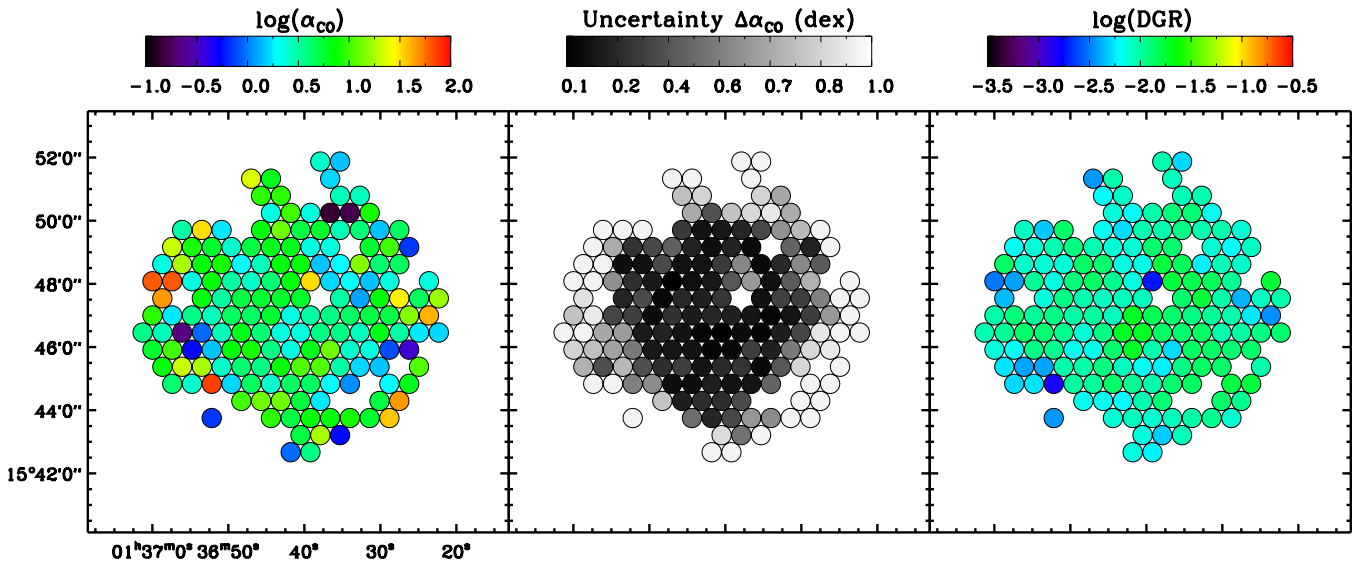

Figure 3. Results of the simultaneous α_{CO} and DGR solutions for NGC 0628. The centers of the solution pixels are represented with circles, as shown on Figure 2. The left panel shows the resulting α_{CO}, the middle panel shows the uncertainty on that value, and the panel on the right shows the DGR. Solution pixels where the technique failed are not shown. For NGC 0628, it is clear that where there are good solutions (as judged by the uncertainty on α_{CO} in the middle panel), most of the values are close to the MW value of $\log(\alpha_{CO}) = 0.64$. In pixels with good solutions, the DGR varies smoothly across the galaxy, which shows that our assumption of a single DGR in each solution pixel is self-consistent.

(A color version of this figure is available in the online journal.)

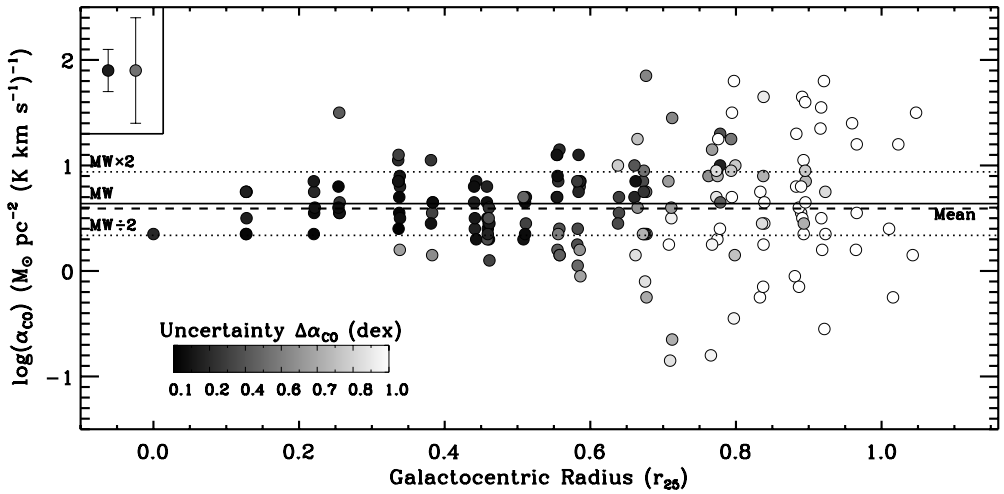

Figure 4. α_{CO} solutions for NGC 0628 as a function of galactocentric radius (in units of r_{25}). The solid horizontal line shows the MW value of $\alpha_{CO} = 4.4\ M_\odot\ \mathrm{pc}^{-2}\ (\mathrm{K\ km\ s}^{-1})^{-1}$ (note that the MW could possibly have a gradient in α_{CO} with radius that we do not show here). The dotted lines show a factor of two above and below the MW value. The dashed horizontal line shows the average value for NGC 0628. The gray scale color of the points represents the uncertainty on α_{CO} as shown in Figure 3—darker points have lower uncertainties. For comparison with the gray color table, two representative error bars for the α_{CO} solutions are shown in the top left corner of the plot. For NGC 0628, almost all of the high confidence α_{CO} solutions are within a factor of two of the MW value.

In general, NGC 0628 shows a α_{CO} value consistent with the MW value within a factor of two at all galactocentric radii. Outside a radius of $r_{25} \sim 0.6$, we find few good solutions. There is a weak trend for lower α_{CO} at smaller radii, with the central solution pixel having a conversion factor $\alpha_{CO} = 2.2\ M_\odot\ \mathrm{pc}^{-2}\ (\mathrm{K\ km\ s}^{-1})^{-1}$. Recent work by Blanc et al. (2013) found consistent results for α_{CO} by inverting the SFR surface density map using a fixed molecular gas depletion time.

4.2. Completeness of Solutions

The technique we have used to solve for the DGR and α_{CO} simultaneously only works if there is sufficient S/N in the CO map and a range of CO/H I ratios in each solution pixel. These two constraints impose limits on where in the galaxies we can recover solutions. In order to perform statistical tests on our sample of α_{CO} and DGR values, we need to understand what biases these limits introduce into our results. For example, the failure of the technique in regions with low CO S/N generally limits our good solutions to the inner parts of galaxies, where metallicities tend to be higher. In order to judge the existence of trends in α_{CO} versus metallicity, we therefore need to understand where we have achieved good solutions.

To investigate these effects, we have examined the fraction of solution pixels that have solutions and the uncertainty on the derived α_{CO} values as a function of the range of CO/H I ratios and mean I_{CO} in a pixel. In general, the H I in our target galaxies has a quite flat radial profile, while the CO drops off approximately exponentially (Schruba et al. 2011). Because of these trends, wherever there is sufficient signal in CO to achieve

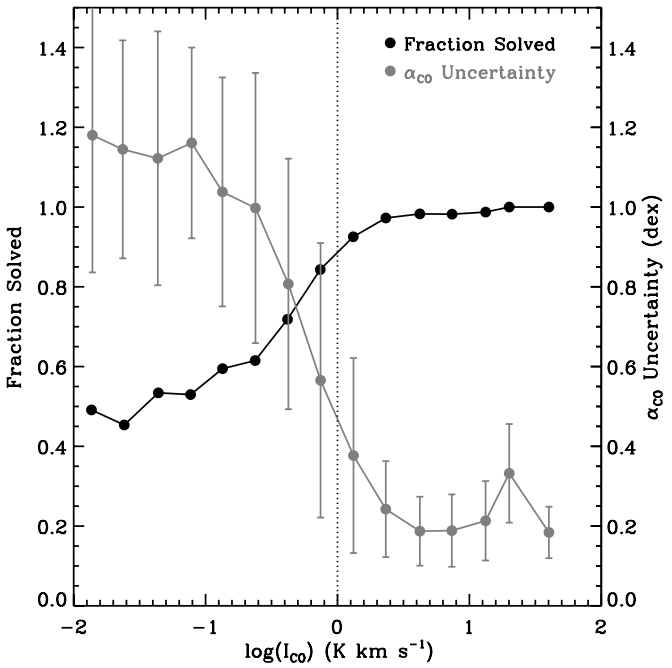

Figure 5. Completeness and quality of our α_{CO} solutions as a function of the mean I_{CO} in a solution pixel. The black points show the fraction of solution pixels where a solution was found. The gray points show the mean uncertainty on α_{CO} with error bars showing the standard deviation. For $I_{CO} > 1$ K km s^{-1}, >90% of solution pixels have solutions and their typical uncertainty is <0.5 dex. We use this 90% completeness cut to select a well-defined sample of α_{CO} measurements for statistical analysis in this work.

a good solution, the CO/H I range is adequate as well. Thus, we find that the mean I_{CO} of a solution pixel is the best predictor for the existence and quality of a solution. Figure 5 shows the fraction of pixels with solutions and the average uncertainty on the solutions as a function of mean I_{CO}. We identify a cut-off at $I_{CO} > 1$ K km s^{-1} above which we obtain solutions >90% of the time and those solutions have an average uncertainty of <0.5 dex. For any statistical analysis that follows, we use only pixels above this cut-off.

4.3. Properties of Full-sample α_{CO} Solutions

In Tables 4 and 5, we list the average α_{CO} derived galaxy by galaxy and for the full sample. These averages only include solution pixels where $I_{CO} > 1$ K km s^{-1}. The first two columns of Table 5 list the mean and standard deviation of the individual solution pixel measurements. This approach treats each solution pixel equally, regardless of how strongly it contributes to the total molecular gas mass. The third column instead lists the mean α_{CO} derived from the total Σ_{H_2} and the total I_{CO} for the galaxy (above $I_{CO} = 1$ K km s^{-1}), which is equivalent to a mean where the pixels are weighted by their I_{CO}, values. If a single α_{CO} value were to be applied to the data, this value would be the optimal quantity to use. For most galaxies, the CO-weighted mean is higher than the straight mean of the solution pixels. This result is due to the fact that the molecular gas is not evenly distributed across the galaxy and the area-weighted average is different then the molecular gas-weighted average.

Figure 6 shows several histograms illustrating the distribution of our measured α_{CO} values. The mean, derived with several different weighting schemes, is listed in Table 5. The top panels of Figure 6 show histograms of all solution pixels while the bottom panels show histograms of the galaxy averages from Table 4. On these histograms, we highlight galaxies with high

Table 4
Galaxy Average α_{CO}

Galaxy	Mean α_{CO}	Std. Dev. (dex)	CO Weighted Mean α_{CO}	Number of Measurements
NGC 0337	22.4	16.2−31.0 (0.14)	21.8	2
NGC 0628	3.9	2.1−7.4 (0.28)	5.1	67
NGC 0925	10.0	6.8−14.7 (0.17)	10.0	1
NGC 2841	5.0	2.5−10.3 (0.31)	5.7	19
NGC 2976	3.3	0.9−12.5 (0.58)	4.7	18
NGC 3077	4.6	2.3−9.4 (0.31)	5.4	7
NGC 3184	5.3	2.9−9.5 (0.26)	6.3	43
NGC 3198	11.0	6.4−18.9 (0.24)	11.9	11
NGC 3351	2.7	1.0−6.9 (0.41)	2.9	28
NGC 3521	7.6	4.9−11.8 (0.19)	7.3	42
NGC 3627	1.2	0.4−3.3 (0.44)	1.8	43
NGC 3938	5.5	4.1−7.5 (0.13)	5.8	19
NGC 4236	...	...	...	0
NGC 4254	3.4	2.1−5.7 (0.22)	4.7	46
NGC 4321	2.2	1.1−4.6 (0.32)	2.2	57
NGC 4536	2.6	1.0−6.7 (0.41)	2.6	13
NGC 4569	1.1	0.3−4.1 (0.57)	1.2	14
NGC 4625	...	...	...	0
NGC 4631	10.8	5.6−19.5 (0.26)	9.8	40
NGC 4725	1.2	0.4−3.2 (0.44)	1.8	7
NGC 4736	1.0	0.5−2.0 (0.29)	1.1	33
NGC 5055	3.7	1.9−7.4 (0.30)	4.0	86
NGC 5457	2.3	1.1−4.8 (0.32)	2.9	142
NGC 5713	4.6	1.7−12.6 (0.44)	5.4	13
NGC 6946	2.0	0.9−4.4 (0.35)	1.8	158
NGC 7331	9.8	6.2−15.3 (0.20)	10.7	32

Notes. Averages include only solution pixels with $I_{CO} > 1$ K km s^{-1}. The number of measurements meeting this criterion are shown in the last column of the table.

inclinations ($i > 65°$) in green. It is clear that the high inclination galaxies tend to have higher α_{CO} values on average than the more face-on galaxies. In the highest inclination galaxies, the pixel will include contributions from gas at larger radii, this gas tends to have a lower DGR and be less molecular-gas-rich. This result is equivalent to the challenge faced by Leroy et al. (2011) in the SMC, where some of the H I along the line of sight originates in an essentially dust-free envelope, and in M31, where regions along the minor axis of the galaxy have contributions from gas and dust at a variety of radii. In addition, optical depth effects for H I may be accentuated for highly inclined galaxies. All galaxies with $i > 65°$ show average α_{CO} values above the mean (except for NGC 0925, which has a somewhat uncertain inclination; de Blok et al. 2008). We thus eliminate all galaxies with $i > 65°$, leaving 782 total α_{CO} measurements.

In Table 5, we list the average values of α_{CO} for the full galaxy sample. Excluding the high inclination galaxies, we find an average $\alpha_{CO} = 2.6\ M_\odot$ pc^{-2} (K km s^{-1})$^{-1}$ for the individual solution pixel results. Weighted by I_{CO}, the average value is slightly higher, $\alpha_{CO} = 2.9\ M_\odot$ pc^{-2} (K km s^{-1})$^{-1}$. To avoid highly resolved galaxies like NGC 5457 and 6946 contributing more points to the average, we also calculate averages where each galaxy contributes uniformly. These averages are listed in the last two columns of Table 5. The average value for our sample, $\alpha_{CO} = 3.1\ M_\odot$ pc^{-2} (K km s^{-1})$^{-1}$, is only slightly lower than what is found in the MW disk.

The standard deviation in α_{CO} is 0.38 dex, when all lines of sight are treated equally (with our I_{CO} and inclination cut-offs). A key question we would like to answer is to what degree this scatter represents (1) the true scatter within each galaxy,

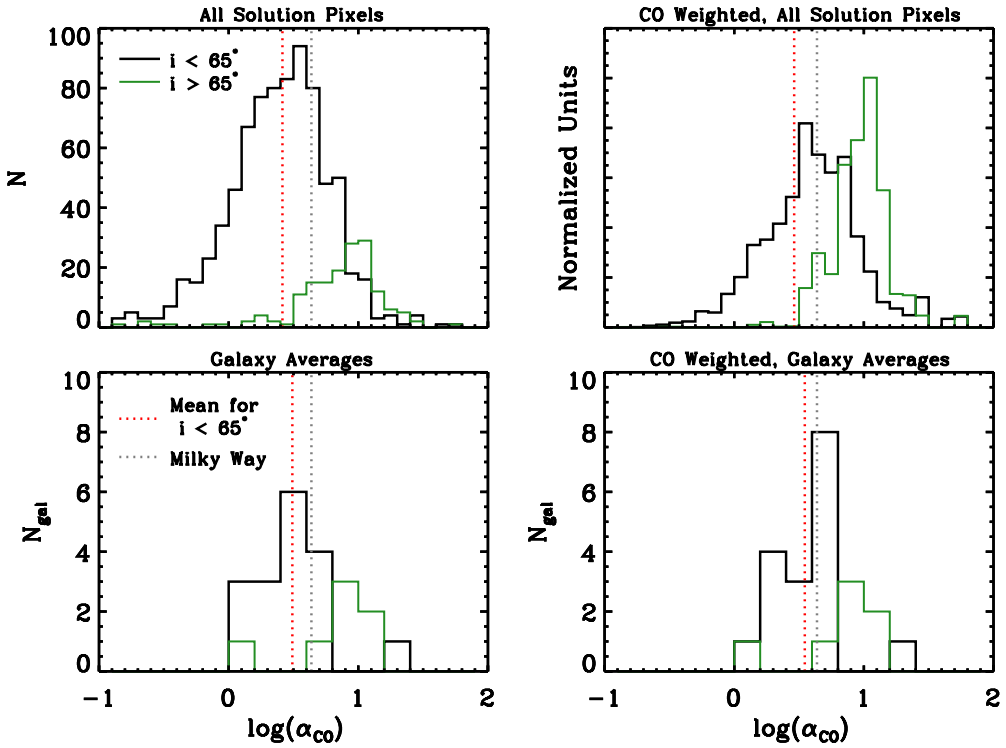

Figure 6. Histograms showing the distribution of α_{CO} results with various weighting schemes. The averages are reported in Table 5. The panels show histograms of galaxies with $i < 65°$ in black and galaxies with $i > 65°$ in green. In each panel, we highlight the mean value of α_{CO} for galaxies with $i < 65°$ with a dotted vertical red line and the Milky Way α_{CO} in gray. These histograms include solution pixels above the $I_{CO} > 1$ K km s^{-1} cutoff. The top left panel shows the histogram of the solution pixels. The top right panel shows those same values weighted by their I_{CO}—this methodology makes pixels contribute to this histogram in proportion to their molecular gas mass. The bottom panels show histograms of the average α_{CO} from each galaxy as listed in Table 4. Galaxies with high inclinations tend to show a higher than average α_{CO}, because the solution pixels include gas and dust at a range of radii. On average, we find α_{CO} values slightly lower than the MW value in our sample.

(A color version of this figure is available in the online journal.)

Table 5
Sample Average α_{CO}

Sample	Mean α_{CO} All Lines of Sight	Std. Dev. (dex)	CO Weighted Mean α_{CO}	Gal. Weighted Mean α_{CO}	Gal and CO Weighted Mean α_{CO}
Incl $< 65°$	2.6	1.0−6.6 (0.41)	2.9	3.1	3.5
Incl $> 65°$	7.2	3.0−17.6 (0.39)	8.2	6.5	6.7

Note. Averages include only solution pixels with $I_{CO} > 1$ K km s^{-1}.

(2) the galaxy-to-galaxy offsets, or (3) the variation of α_{CO} as a function of local parameters. If the scatter comes from variations with local environmental parameters, we may be able to generate a prescription for α_{CO} as a function of other observables. In the following sections, we explore the variations of α_{CO} within and among our galaxies to understand if and why α_{CO} varies.

4.4. Radial Variations in α_{CO}

In Figure 7, we present a summary of the α_{CO} values we find as a function of galactocentric radius. Plots of α_{CO} from each individual galaxy as a function of r_{25} are presented in the Appendix. Each individual solution that makes our I_{CO} and inclination cut is shown in Figure 7 as a gray circle. We also display the mean and standard deviation of the α_{CO} values in 0.1 r_{25} bins for each galaxy (this mean treats all solution pixels equally). The top panel of Figure 7 shows the measured α_{CO} values and the bottom panel shows those same values normalized by each galaxy's average α_{CO} from Table 4.

The average radial profile of our galaxies is mostly flat as a function of r_{25}, but almost all galaxies show a decrease in α_{CO} in the inner ∼0.2 r_{25} compared to their average value. The mean central decrease is ∼0.3–0.4 dex, but it can be as much as 0.8 dex. For several galaxies, this decrease leads to a central α_{CO} value that is an order to magnitude lower than the MW α_{CO} (e.g., NGC 4736, 5457, and 6946). The central depression persists even after correcting for differences in R_{21} (see the following section for further discussion).

Normalizing each galaxy by its average α_{CO} and making each galaxy contribute equally to the average leads to a much smaller scatter at $r_{25} > 0.3$; this result can be seen in the bottom panel of Figure 7 where the radial profiles show much less scatter than the individual measurements, which is not the case in the top, unnormalized, panel. Inside that radius, the scatter in the normalized α_{CO} profiles is reduced, but not by as much as outside that radius, indicating that individual galaxies show different central profiles of α_{CO}. The overall conclusions to be drawn from Figure 7 are: (1) outside $r_{25} \sim 0.3$, most of the scatter in our α_{CO} measurements can be explained by galaxy-to-galaxy

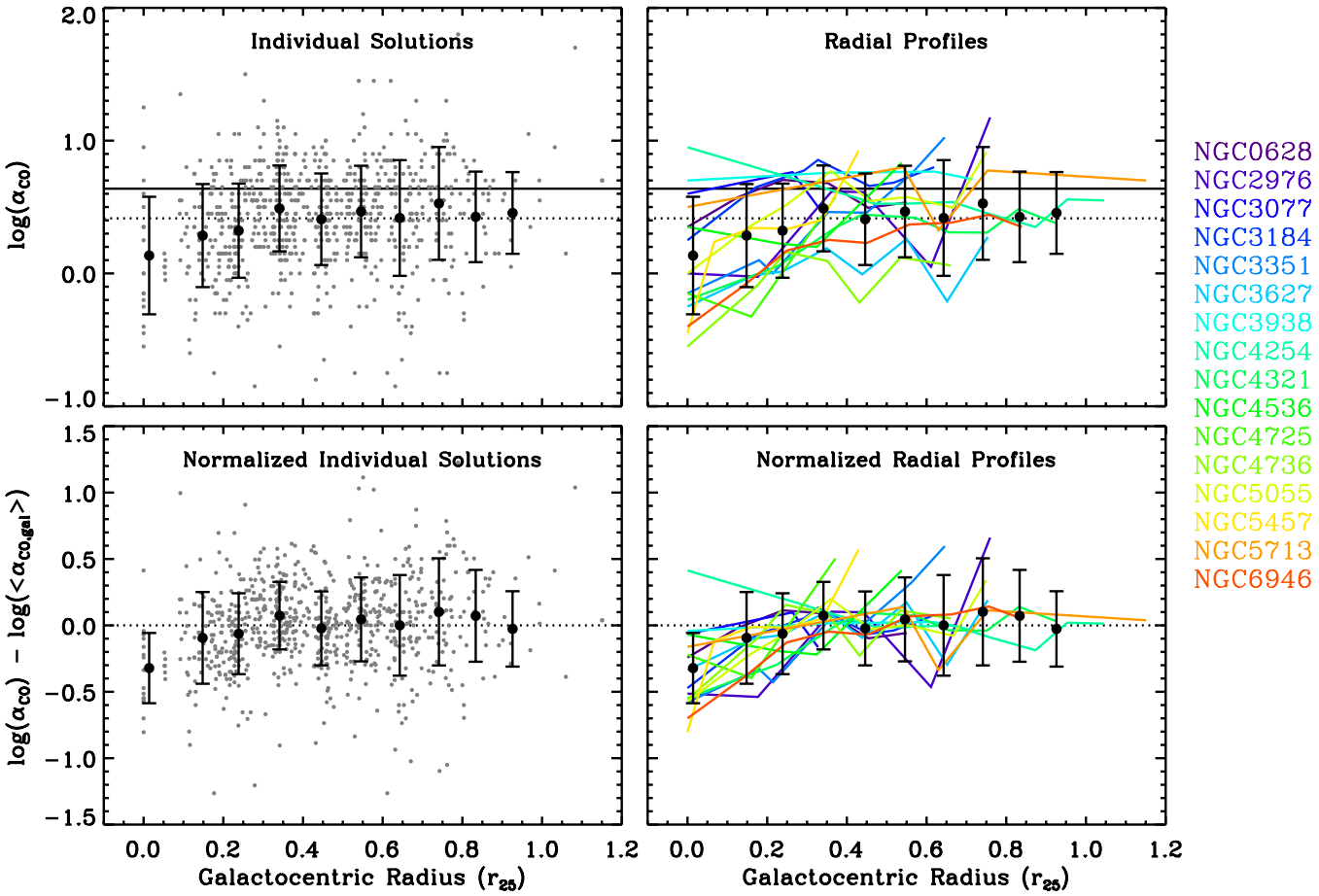

Figure 7. Solutions for α_{CO} vs. galactocentric radius (r_{25}). The top left panel shows the α_{CO} solutions and the bottom-left panel shows the same values normalized by each galaxy's average α_{CO} (listed in Table 4). All individual solutions are shown as gray points. The mean and standard deviation of all of the solutions in 0.1 r_{25} bins are shown with black symbols (this mean treats all lines of sight equally). The solid black horizontal line in the top panel shows α_{CO} for the Milky Way. The dotted black horizontal line shows the average, with no weighting, of all solution pixels: $\alpha_{CO} = 2.6\ M_{\odot}\ pc^{-2}\ (K\ km\ s^{-1})^{-1}$. In the right panels, the radial profile for each galaxy is shown with a solid colored line overlaid with the same binned average from the left-hand panels. The average α_{CO} radial profile of our galaxies is mostly flat as a function of r_{25}, with a decrease in α_{CO} toward the center of the galaxy. On average, the central α_{CO} value is ~0.3 dex lower than the rest of the galaxy.

(A color version of this figure is available in the online journal.)

differences, (2) inside that galactocentric radius, galaxy-specific trends in α_{CO} dominate the scatter, and (3) in general, the inner region of galaxies shows a lower α_{CO} value than the rest of the disk.

4.5. α_{CO} in Galaxy Centers

In Table 6, we list the central α_{CO} values and compare them to the MW value and the mean for the galaxy. Almost all of the central solution pixels have α_{CO} lower than the galaxy mean. The galaxies NGC 3351, 3627, 4321, 4736, 5457, and 6946 show α_{CO} values a factor of five or more lower than the MW value, at the 3σ confidence level. For NGC 4736, 5457, and 6946, in particular, the central solution pixel has a α_{CO} value an order of magnitude below the MW value. Only one galaxy, NGC 0337, shows a central α_{CO} higher than the MW value at a 3σ confidence level. In Table 6, we also list the CO (2–1)/(1–0) ratio measured as described in Section 3.4.1. While the central solution pixels do tend to have higher R_{21} values than the value we adopted, the difference is less than a factor of two in all cases and does not alter our main conclusions about the low (1–0) conversion factor in these regions. In particular, for the 10 galaxies with measured R_{21} and $i < 65°$, the central α_{CO} corrected for R_{21} is still on average 0.3 dex lower (i.e., a factor of two) than the galaxy average.

The central solution pixels can be outliers from the rest of the pixels in our sample in the sense of having high CO/H I ratios. Since there are relatively few solution pixels with these conditions, they may not have been well represented in the simulated data we used to test the accuracy of the solution technique. High CO/H I ratios could bias the results: if the S/N of the H I maps is almost always higher than the S/N of the CO maps, the DGR scatter could be reduced in these conditions purely by decreasing the importance of CO in assessing the gas mass surface density. Since this bias would move the α_{CO} results toward lower values in the centers, we performed a test to judge whether our low central α_{CO} measurements could be due to this effect. The details of the test are described in the Appendix. In brief, we generated simulated datasets with known α_{CO} values where the $N_{H\,I}$, I_{CO}, and Σ_D S/N is matched to the observations in each central solution pixel. We performed Monte Carlo trials to see how well the known input α_{CO} was recovered. In all cases, we found no evidence for a bias in the central solution pixel.

Taking into account the offset from R_{21} variations, our results show that the central α_{CO} in NGC 3351, 3627, 4321, 4736, 5457, and 6946 is lower than the MW value by a factor of 4–10. Many of these galaxies show α_{CO} values closer to the MW value at larger radii, in line with the general trend seen in Figure 7. For NGC 3627, the mean α_{CO} for the galaxy is

Table 6
Central α_{CO} Measurements

Galaxy	$\log(\alpha_{CO,Cen}) \pm \sigma$	$\Delta_{MW} = \log(\alpha_{CO}/\alpha_{CO,MW})$	Δ_{MW}/σ	$\Delta_{mean} = \log(\alpha_{CO}/\langle\alpha_{CO}\rangle)$	Δ_{mean}/σ	R_{21}	$\log(R_{21}/0.7)$
NGC 0337	$+1.25 \pm 0.17$	$+0.61$	3.6	-0.10	0.6	...	...
NGC 0628	$+0.35 \pm 0.24$	-0.29	1.2	-0.24	1.0	...	...
NGC 2976	$+0.00 \pm 0.49$	-0.64	1.3	-0.51	1.0	...	...
NGC 3077	$+0.60 \pm 0.17$	-0.04	0.2	-0.06	0.4	...	...
NGC 3184	$+0.25 \pm 0.16$	-0.39	2.5	-0.47	3.0	0.77 ± 0.05	$+0.04$
NGC 3351	-0.15 ± 0.14	-0.79	5.6	-0.58	4.1	1.10 ± 0.24	$+0.19$
NGC 3627	-0.25 ± 0.14	-0.89	6.3	-0.34	2.4	0.54 ± 0.05	-0.12
NGC 3938	$+0.70 \pm 0.19$	$+0.06$	0.3	-0.04	0.2	...	...
NGC 4254	$+0.95 \pm 0.82$	$+0.31$	0.4	$+0.41$	0.5	1.03 ± 0.06	$+0.17$
NGC 4321	-0.20 ± 0.17	-0.84	4.8	-0.55	3.1	1.25 ± 0.16	$+0.25$
NGC 4536	$+0.35 \pm 0.13$	-0.29	2.2	-0.07	0.5	1.26 ± 0.28	$+0.26$
NGC 4625	$+1.05 \pm 0.41$	$+0.41$	1.0	...	...	...	...
NGC 4725	-0.15 ± 0.71	-0.79	1.1	-0.22	0.3	...	...
NGC 4736	-0.55 ± 0.17	-1.19	6.9	-0.56	3.2	1.35 ± 0.09	$+0.29$
NGC 5055	$+0.00 \pm 0.25$	-0.64	2.6	-0.57	2.3	1.10 ± 0.08	$+0.20$
NGC 5457	-0.45 ± 0.20	-1.09	5.5	-0.80	4.1	0.90 ± 0.08	$+0.11$
NGC 5713	$+0.50 \pm 0.25$	-0.14	0.6	-0.16	0.6	...	...
NGC 6946	-0.40 ± 0.31	-1.04	3.4	-0.70	2.3	1.07 ± 0.14	$+0.19$

Note. Galaxies with $i > 65°$ have been omitted from the table.

low as well, suggesting that the central region is not distinct from the rest of the disk (this galaxy is an interacting member of the Leo Triplet, so it is unique in our sample). Conversely, examination of the individual galaxy α_{CO} measurements as a function of radius (shown in the Appendix) for NGC 3351, 4321, 4736, 5457, and 6946 demonstrates that these galaxies show an unresolved region of lower-than-average α_{CO} values in their centers (note that our solution pixel grid oversamples the data, so an unresolved central depression affects the $r_{25} = 0$ point and the six adjacent solution pixels). The closest galaxy that shows a central depression is NGC 4736 at $D = 4.66$ Mpc. At this distance, our solution pixel covers a region of radius 0.8 kpc. Even for this nearby example, we do not resolve the central depression. We tested whether the depressions were resolved using a grid of independent solution pixels (i.e., not overlapping) and found that the depression only affected the central pixel, consistent with it being unresolved. We note that our ability to detect any central depression may be a function of the galaxy's distance due to the increased size of the central solution pixel. Even at $D = 14.3$ Mpc, however, we detect a clear central depression in NGC 4321.

The type of nuclear activity in each galaxy is not a good predictor for whether or not it displays a central α_{CO} depression. Of the galaxies that show the clearest central depression, NGC 3351, 5457, and 6946 are classified as star-formation or H II region dominated, while NGC 4321 and 4736 have signatures of active galactic nucleus (AGN) or low-ionization nuclear emission-line region activity (for details on the nuclear classifications; see Kennicutt et al. 2011). Several galaxies with flat radial α_{CO} profiles do show evidence for AGN activity: NGC 3627, 4254, and 4725, for example. Enhanced AGN activity could affect molecular gas properties in the nuclei (e.g., Krips et al. 2008), but the relatively weak AGNs present in the KINGFISH galaxies may not dominate on the kiloparsec scales we study here.

To summarize, we find that several galaxies in our sample show central α_{CO} values that are substantially lower than the MW value and also well below the galaxy average. This phenomenon appears to take the form of a depression in the central region that is unresolved by our solution pixel grid. We discuss these central regions and the physical conditions that may lead to low α_{CO} values further in Section 6.3.

4.6. Correlations of α_{CO} with Environmental Parameters

Variations in α_{CO} may be related to variations in the local environmental conditions including metallicity, ISM pressure, interstellar radiation field strength, gas temperature, dust properties, or other variables. Correlations between α_{CO} and quantities that trace these environmental conditions may allow us to identify the drivers of α_{CO} variations. These correlations may also provide tools to predict the appropriate α_{CO} in a given environment. In the following, we examine the correlations of our measured α_{CO} with several observables that trace ISM conditions. For each tracer, we use the average value in each solution pixel. The physical interpretation of these correlations or lack thereof is discussed in Section 6.1.

In Figure 8, we plot our measured α_{CO} values as a function of the average radiation field intensity ($\overline{U}$), the PAH fraction (q_{PAH}), metallicity ($12 + \log(O/H)$), stellar mass surface density (Σ_*), SFR surface density (Σ_{SFR}), and the dust mass surface density (Σ_D). Each panel shows the individual measurements as gray symbols and the average for the galaxies as red symbols. The MW α_{CO} is highlighted with a horizontal gray line and the mean α_{CO} treating all solution pixels equally ($\alpha_{CO} = 2.6\ M_\odot\ pc^{-2}\ (K\ km\ s^{-1})^{-1}$) is shown as a dashed horizontal line. Overlaid on each panel is the binned mean and standard deviation and a linear fit to the gray points. In Table 7, we list the linear fit results as well as the rank correlation (RC) coefficient for each panel and its significance in standard deviations away from the null hypothesis. The RC coefficients suggest there are significant correlations between α_{CO} and all of the variables except metallicity. Due to possible inconsistencies between various metallicity measurements and incomplete knowledge of metallicity gradients in some galaxies, we examine the trends with metallicity separately in Section 4.6.1.

Several other radiation field properties are measured from the dust SED modeling. These include U_{min}, the minimum radiation field heating the dust, and f_{PDR}, the fraction of the

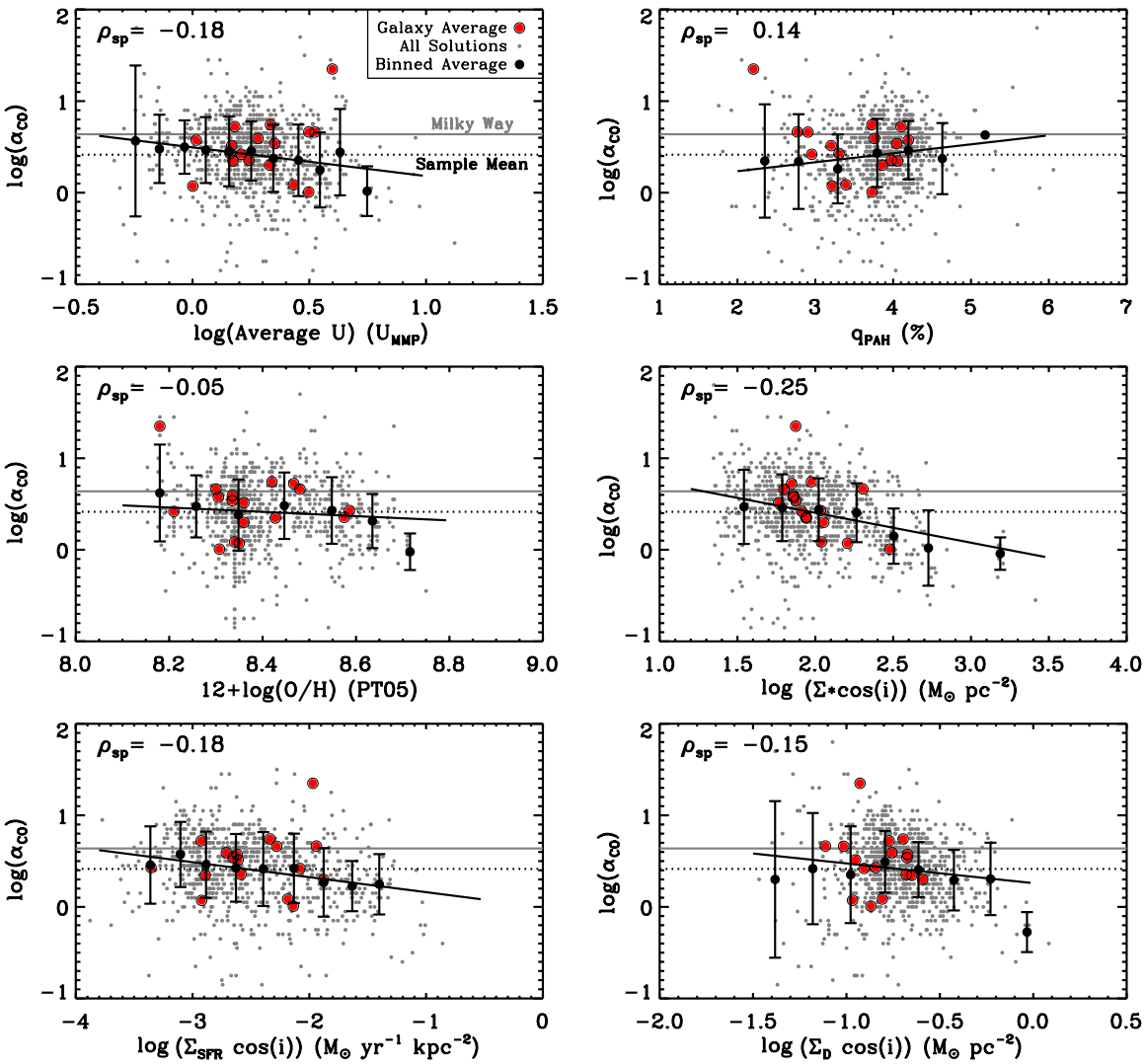

Figure 8. α_{CO} as a function of environmental parameters. The panels show α_{CO} plotted vs. average radiation field intensity ($\overline{U}$; top left) and PAH fraction (q_{PAH}; top right) from the Aniano et al. (2012) fits, metallicity (12 + log(O/H); middle left), stellar mass surface density (Σ_*; middle right), star-formation rate surface density (Σ_{SFR}; lower left) and dust mass surface density (Σ_D; lower right). The solid gray line shows the Milky Way α_{CO} and the dotted black line shows the sample average $\alpha_{CO} = 2.6\ M_\odot\ pc^{-2}\ (K\ km\ s^{-1})^{-1}$, treating all solution pixels equally. Individual α_{CO} solutions above our I_{CO} and inclination cuts are shown with gray symbols. The mean and standard deviation of those values in bins are shown with black circles and error bars. A linear fit to the measurements is shown with a black line. The mean values for all galaxies are shown with red circles. The Spearman rank correlation coefficient for each panel is listed in the top left. All variables except for metallicity show a statistically significant correlation with α_{CO}. None of these correlations allow α_{CO} to be predicted with significantly better precision than the scaling with r_{25}. However, the extreme values of Σ_{SFR} (>0.5 $M_\odot\ yr^{-1}\ kpc^{-2}$) and Σ_* (>1000 $M_\odot\ pc^{-2}$) are always associated with low α_{CO} and are located in galaxy centers.

(A color version of this figure is available in the online journal.)

Table 7
α_{CO} Correlation Properties

log(α_{CO}) vs.	Correlation[a]	σ from	Linear Fit[b]	
Variable	Coeff.	Null	Offset	Slope
r_{25}	+0.19	5.2	0.29	+0.29
log($\overline{U}$)	−0.18	5.0	0.50	−0.31
q_{PAH} (%)	+0.14	3.9	0.11	+0.10
12 + log(O/H)	−0.05	1.4	2.39	−0.24
log(Σ_*)	−0.26	7.1	1.05	−0.33
log(Σ_D)	−0.15	4.1	0.26	−0.22
log(Σ_{SFR})	−0.18	5.1	0.00	−0.16

Notes. These correlations are shown in Figure 8.
[a] Spearman rank correlation coefficient.
[b] Correlation with metallicity using a homogeneous sample of metallicity measurements is discussed in Section 4.6.1.

dust luminosity that arises in "photodissociation region (PDR) like" regions where $U > 100\ U_{MMP}$. We have investigated the dependence of α_{CO} on these quantities and find weak trends with low significance.

The existence of a correlation between α_{CO} and environmental parameters does not directly identify the cause of the variations in α_{CO}, particularly since all of the parameters change radially to first order. In Figure 9, we illustrate the radial variations of the same variables by plotting them normalized by their average value as a function of r_{25}. All of the variables show significant correlations with radius. Table 8 lists the correlation coefficients and linear fits to the normalized radial profiles of the parameters. In all cases, the correlation of the variables with r_{25} is more significant than the correlation of α_{CO} with those variables.

If all of the variations of these parameters were primarily related to radius, we would not expect to find stronger correlations between α_{CO} and any parameter than between α_{CO} and radius.

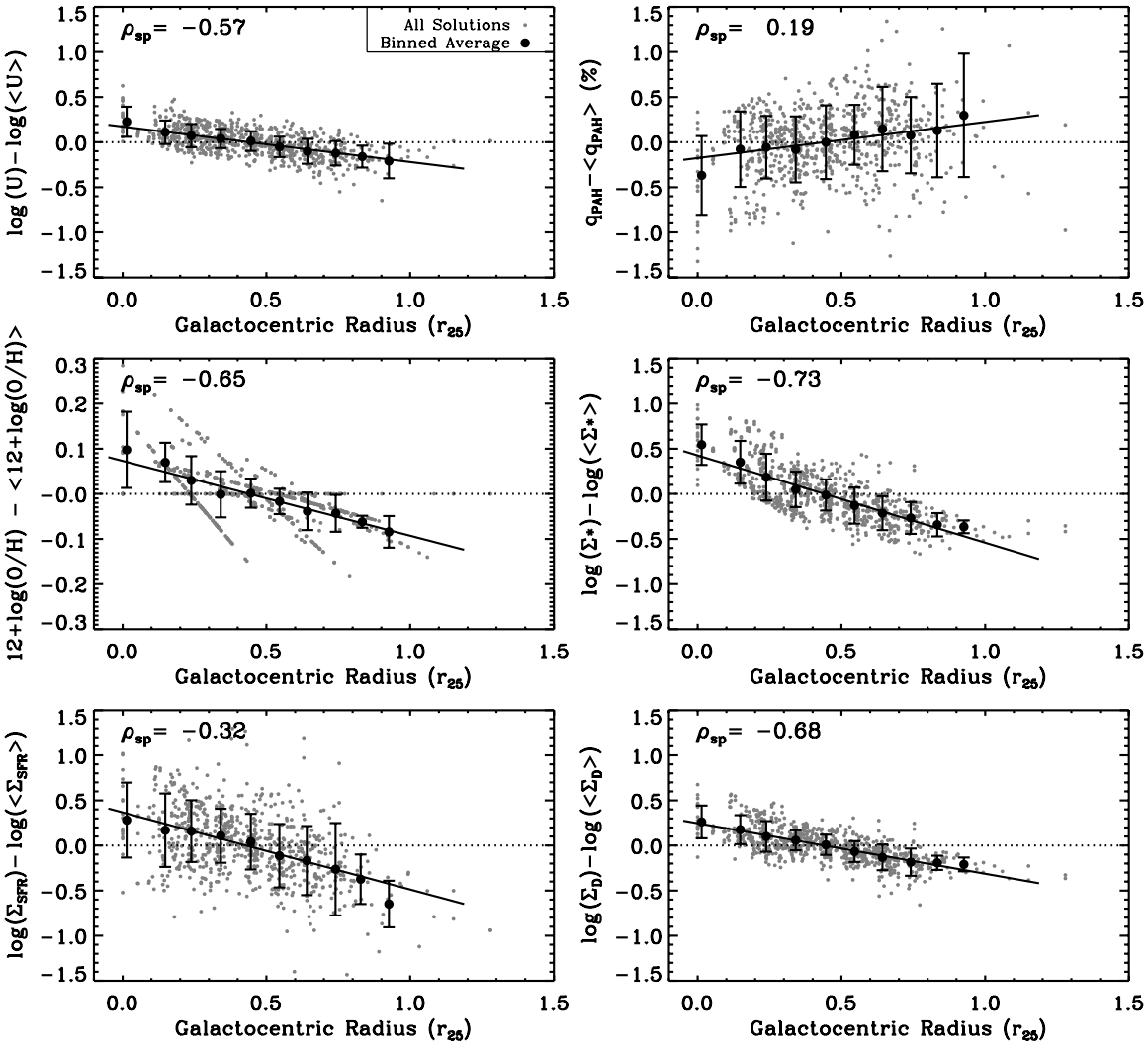

Figure 9. Normalized environmental parameters as a function of galactocentric radius r_{25}. In each panel, we show the average value of each quantity in the solution pixel, normalized by the mean value for the galaxy, with gray circles. The mean and standard deviation of the binned, normalized values are shown with black circles and error bars. A linear fit is shown with a solid black line. The Spearman rank correlation coefficient for each panel is listed in the top left. All parameters (radiation field strength, PAH fraction, metallicity, stellar mass surface density, star-formation rate surface density, dust mass surface density, and α_{CO}) show significant radial correlations. Since we have assumed radial gradients in the metallicity for many galaxies, normalized metallicity directly reflects the slopes of these gradients. In general, these radial trends are much stronger than the correlations between the variables and α_{CO} presented in Figure 8.

Table 8
Correlation Properties versus r_{25}

Variable vs.	Correlation[a]	σ from	Linear Fit	
r_{25}	Coeff.	Null	Offset	Slope
$\log(\alpha_{CO}/\langle\alpha_{CO}\rangle_{gal})$	+0.18	5.0	−0.10	+0.23
$\log(\overline{U}/\langle\overline{U}\rangle_{gal})$	−0.57	15.9	0.17	−0.39
$q_{PAH}/\langle q_{PAH}\rangle_{gal}$	+0.19	5.3	−0.17	+0.40
$\log((O/H)/\langle O/H\rangle_{gal})$	−0.65	18.2	0.07	−0.17
$\log(\Sigma_*/\langle\Sigma_*\rangle_{gal})$	−0.73	20.5	0.43	−0.97
$\log(\Sigma_D/\langle\Sigma_D\rangle_{gal})$	−0.68	19.1	0.25	−0.56
$\log(\Sigma_{SFR}/\langle\Sigma_{SFR}\rangle_{gal})$	−0.31	8.8	0.37	−0.86

Notes. These correlations are shown in Figure 9.
[a] Spearman rank correlation coefficient.

Our results suggest, however, that the correlation between α_{CO} and Σ_* is stronger ($r_s = -0.25$) and more significant (7.1σ) than the correlation with radius r_{25} ($r_s = +0.19$, 5.2σ). One possible explanation is that our Σ_* measurement may trace the stellar profile better than r_{25} itself. Other explanations for the correlation of α_{CO} with Σ_* will be discussed in Section 6.1.

Figure 7 illustrates that the normalized radial profile of α_{CO} shows a factor of $\sim$2 standard deviation in a typical radial bin. This uncertainty can be explained primarily by the uncertainty on our α_{CO} solutions themselves, which is typically close to a factor of $\sim$2. It is therefore unlikely that we could predict α_{CO} as a function of other variables to better precision than a factor of $\sim$2 unless the galaxy average α_{CO} is highly correlated with that variable. In general, the galaxy averages shown in Figure 8 do not appear to be more tightly correlated with the environmental parameters. Figure 8 thus illustrates that aside from outliers at the extremes of these plots, the minimum standard deviation of α_{CO} in these bins is a factor of two or more and correlations with environmental parameters do not allow us to predict the behavior of α_{CO} within the galaxies better than our normalized radial profile.

As previously discussed, the average profile of α_{CO} versus radius is mostly flat with a central depression in some galaxies. Many of the environmental parameters we plot in Figures 8

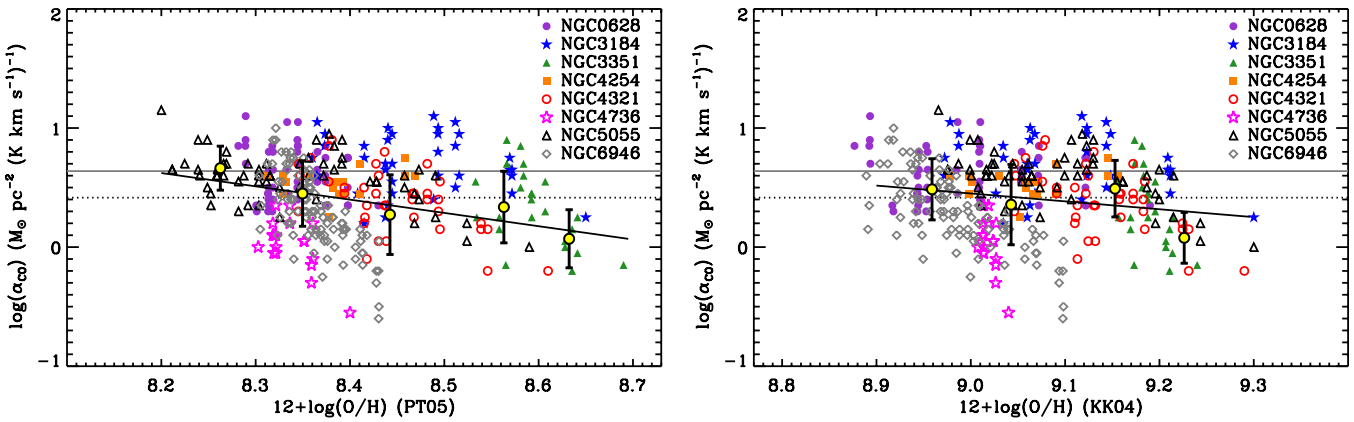

Figure 10. Measured α_{CO} values as a function of metallicity for galaxies with H II region abundance gradients from M10 with the PT05 (left) and KK04 (right) calibrations. Only measurements with uncertainties less than <0.3 dex are shown. The mean and standard deviation in 0.1 dex bins of metallicity are shown with yellow circles and black error bars. A linear fit to $\alpha_{CO}(Z)$ is overlaid with a solid black line. The correlation of α_{CO} with metallicity is weak for both calibrations. In particular, it is clear that galaxies with shallow metallicity gradients like NGC 6946 can still span a wide range of α_{CO} values, whereas those galaxies with large gradients, like NGC 3184, may have essentially constant α_{CO} values.

(A color version of this figure is available in the online journal.)

and 9 show radial trends extending over the entire range we cover, although the normalized trends generally span less than an order of magnitude. This range does not provide the leverage necessary to separate the dominantly radial correlations of multiple variables. Future studies attempting to associate changes in α_{CO} with environmental parameters will need either higher precision measurements of α_{CO} or observations spanning a greater range of environments.

One possible way to overcome the limitations of separating various radial trends is to normalize all of the variables by their mean in radial bins and then search for residual trends between them. We have investigated such non-radial variations in 0.1 r_{25} bins and, in general, find only very weak trends. NGC 4254 is one of few galaxies that shows a marginally significant correlation—the normalized α_{CO} measurements correlate with normalized $\overline{U}$ and Σ_* at the level of 4σ–5σ from the Spearman RC coefficient. In both cases, the correlation is positive, such that α_{CO} increases in regions with higher $\overline{U}$ and Σ_* compared to the average in that radial bin. NGC 6946 also shows a correlation at the 5σ level between normalized α_{CO} and f_{PDR}. In this case, the correlation is negative, meaning that α_{CO} decreases in regions with high f_{PDR}.

NGC 6946 is unique in that the non-radial structure is clearly visible in the maps of α_{CO} shown in the Appendix. The low α_{CO} values in that galaxy appear to track the spiral arm structure seen in the I_{CO} and Σ_D maps. To quantify this observation, we have investigated the correlation between the radially normalized α_{CO}, I_{CO}, Σ_D, and Σ_{HI} values. These correlations are weak (all are $<5\sigma$ significance in the Spearman RC) but more widespread. NGC 3627, 4254, 4321, 5457, and 6946 all show some degree of correlation at $>3\sigma$ with radially normalized I_{CO}, Σ_{HI}, or Σ_D values. For all galaxies aside from NGC 6946, the correlations are positive, in the sense that the conversion factor is higher where there is more H I and dust or more CO emission. NGC 6946 shows negative correlations with all of these parameters.

4.6.1. α_{CO} versus Metallicity

Metallicity has been suggested by several theoretical and observational studies to be an important driver for α_{CO} variations. Unfortunately, metallicity measurements in nearby galaxies are often very uncertain and subject to systematic errors from different calibrations and techniques. In Figure 8, we show our α_{CO} measurements as a function of metallicity from the PT05 calibration (middle left panel). Our measurements span ~0.5 dex in metallicity with no statistically significant trend in α_{CO}. One possible reason for the lack of a clear trend in this figure is that we have combined metallicity measurements obtained with different techniques. In addition, many of the galaxies in our sample lack constraints on possible gradients.

To explore any metallicity trends that may be washed out due to systematic effects when combining metallicities from different sources, we isolate a sample of galaxies with uniformly determined metallicities from M10 and plot those separately in Figure 10. We have eliminated galaxies whose metallicities have been determined from integrated spectrophotometry (those listed as "M10 Table 9" in Table 3) because the drift scan observations were not always along angles that allow a robust gradient measurement. We also isolate our highest confidence α_{CO} measurements by showing only those with uncertainties less than 0.3 dex (a factor of ~2). We show metallicities with both the PT05 and KK04 calibrations for comparison.

In general, there is a slight negative correlation of α_{CO} with metallicity for this subsample. With the PT05 calibration, we find a RC coefficient of $r = -0.2$, which is 3.8σ from the null result given the number of measurements. Using the KK04 metallicities, we find $r = -0.1$ at 2.0σ from the null result. If we remove the S/N cut on the α_{CO} measurements, the correlations in both PT05 and KK04 essentially disappear, yielding results that are less than 1σ from the null result.

The weakness of the correlation between α_{CO} and metallicity suggests that in the regions of the galaxies we are studying, metallicity may not be the primary driver of α_{CO} variations. Along these lines, it is interesting to note the contrast between a galaxy like NGC 6946, which has a relatively shallow metallicity gradient, and galaxies like NGC 0628 and 3184, which are thought to have much steeper gradients. NGC 6946 has α_{CO} values spanning a range of an order of magnitude, while NGC 0628 and 3184 have much smaller ranges—the opposite of what we would expect if their metallicity gradients were the dominant factor controlling α_{CO}.

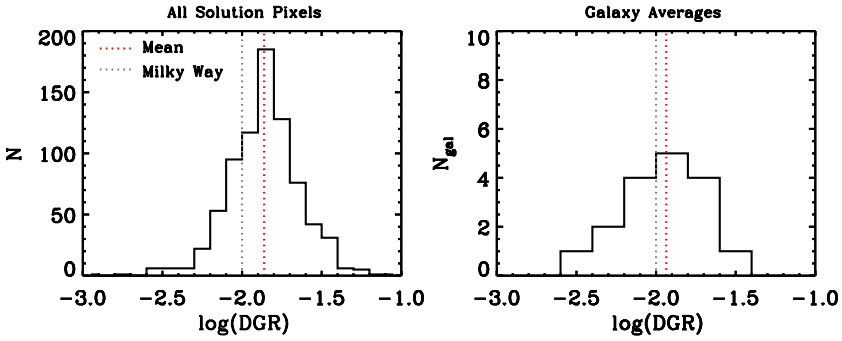

Figure 11. Histograms of the measured DGR values for all solution pixels (left) and galaxies (right) in our sample. The dotted red line shows the mean value for the sample and the dotted black line shows the local MW DGR of 0.01 for comparison. The average DGR for our sample is slightly higher than in the MW. The standard deviation of the DGR measurements is 0.22 dex, which is smaller than the scatter in the α_{CO} values for these same pixels.

(A color version of this figure is available in the online journal.)

4.7. Properties of the Full-sample DGR Solutions

In the Appendix, we show the measured DGR for all galaxies and solution pixels in figures similar to Figure 3. The DGR we report is the mean value for all of the individual sampling points in a solution pixel. Generally, the scatter in the DGR_i values within a solution pixel is small (<0.1 dex). This result means that the uncertainty on the α_{CO} value generally dominates the uncertainty on the DGR as well. Therefore, it is important to note that the errors in the DGR and α_{CO} values are highly correlated. We assign a representative uncertainty on the DGR using the $\pm 1\sigma$ bounds on α_{CO}. In general, when good solutions are obtained, the DGR measurements vary smoothly across the galaxy. This result supports our key assumption that the DGR varies on scales larger than our solution pixels. The smoothness of the DGR maps can be seen by inspecting the figures in the Appendix and the results for NGC 0628 shown in Figure 3.

In Figure 11, we show a histogram of all of the measured DGR values for our galaxies that comply with our cuts in inclination and I_{CO}. The average of our measurements treating all lines of sight equally is $\log(DGR) = -1.86$ with a standard deviation of 0.22 dex. This finding is slightly higher than the value typically adopted for the solar neighborhood of $\log(DGR_{MW}) = -2.0$. Forcing all galaxies to contribute equally to the average despite differing numbers of solution pixels gives $\log(DGR) = -1.96$. The lower scatter in the DGR measurements for all solution pixels compared to the α_{CO} measurements, despite the uncertainty on α_{CO} dominating the uncertainty on the DGR, is due to the contribution of H I to the total gas mass surface density. Because H I makes up some fraction of the gas mass, the DGR has a smaller possible range over which to vary compared with α_{CO}.

4.8. Correlations of the DGR with Environmental Parameters and Radius

The DGR may also vary as a function of environmental parameters. To explore any such trends, we show our measured DGR values as a function of the same tracers we have previously studied in Figure 12. We list the correlation coefficients and linear fit parameters in Table 9.

The DGR shows significant correlations with galactocentric radius, metallicity, and Σ_*. Even with heterogeneously determined metallicities, it shows a much clearer trend with $12+\log(O/H)$ than α_{CO} does over the same range. A correlation of the DGR with metallicity is expected—given the high depletions of elements such as Mg, Si, Ca, and Ti in the local area of the MW, to first order the mass of dust should be proportional to the amount of heavy elements.

Table 9
DGR Correlation Properties

log(DGR) vs.	Correlation[a]	σ from	Linear Fit[b]	
Variable	Coeff.	Null	Offset	Slope
r_{25}	−0.33	9.2	−1.71	−0.35
$\log(\overline{U})$	+0.01	0.3	−1.87	+0.02
q_{PAH} (%)	+0.00	0.1	−1.85	+0.00
$12+\log(O/H)$	+0.26	7.3	−6.50	+0.55
$\log(\Sigma_*)$	+0.28	7.9	−2.27	+0.21
$\log(\Sigma_{SFR})$	+0.03	0.8	−1.79	−0.03

Notes. These correlations are shown in Figure 8.
[a] Spearman rank correlation coefficient.
[b] Correlation with metallicity using a homogeneous sample of metallicity measurements is discussed in Section 4.8.

In Figure 13, we show the DGR as a function of metallicity for the same sample of galaxies in Figure 10. In addition to the best linear fit, shown with a dotted black line, we also plot a prediction for the linear scaling of the local MW DGR with metallicity (solid black line). The dashed lines above and below show a factor of two higher and lower DGRs. The scaling of the plot is such that it covers three orders of magnitude, the same range covered in Figure 10. It is clear that the DGR values have much less scatter than the α_{CO} values over the same range of metallicity—a product of the limited allowable range of DGRs set by the fact that some dust is associated with H I.

The DGR values show a stronger correlation with metallicity than the α_{CO} values do. With the PT05 calibration, we find a RC coefficient of 0.35, which is significant at the 6.4σ level. For KK04, the correlation coefficient is 0.39 at 6.9σ. In a given metallicity bin, the standard deviation of the DGR values is ∼0.15 dex for PT05 and ∼0.18 for KK04. This result suggests that, on average, we should be able to predict DGRs to better than a factor of two given the metallicity in one of these calibrations. In addition, we do not see evidence for major galaxy-to-galaxy offsets in the DGR versus metallicity plots, which distinguishes the DGR and α_{CO} behaviors; most galaxies appear to have similar slopes in the plots.

Neither the KK04 nor PT05 calibration values fall directly along the line of the scaled MW DGR. On the PT05 scale, almost all of our sample has higher DGRs for a given metallicity than the MW scaling, while the opposite is true on the KK04 scale. For purposes of scaling the MW metallicity, we have

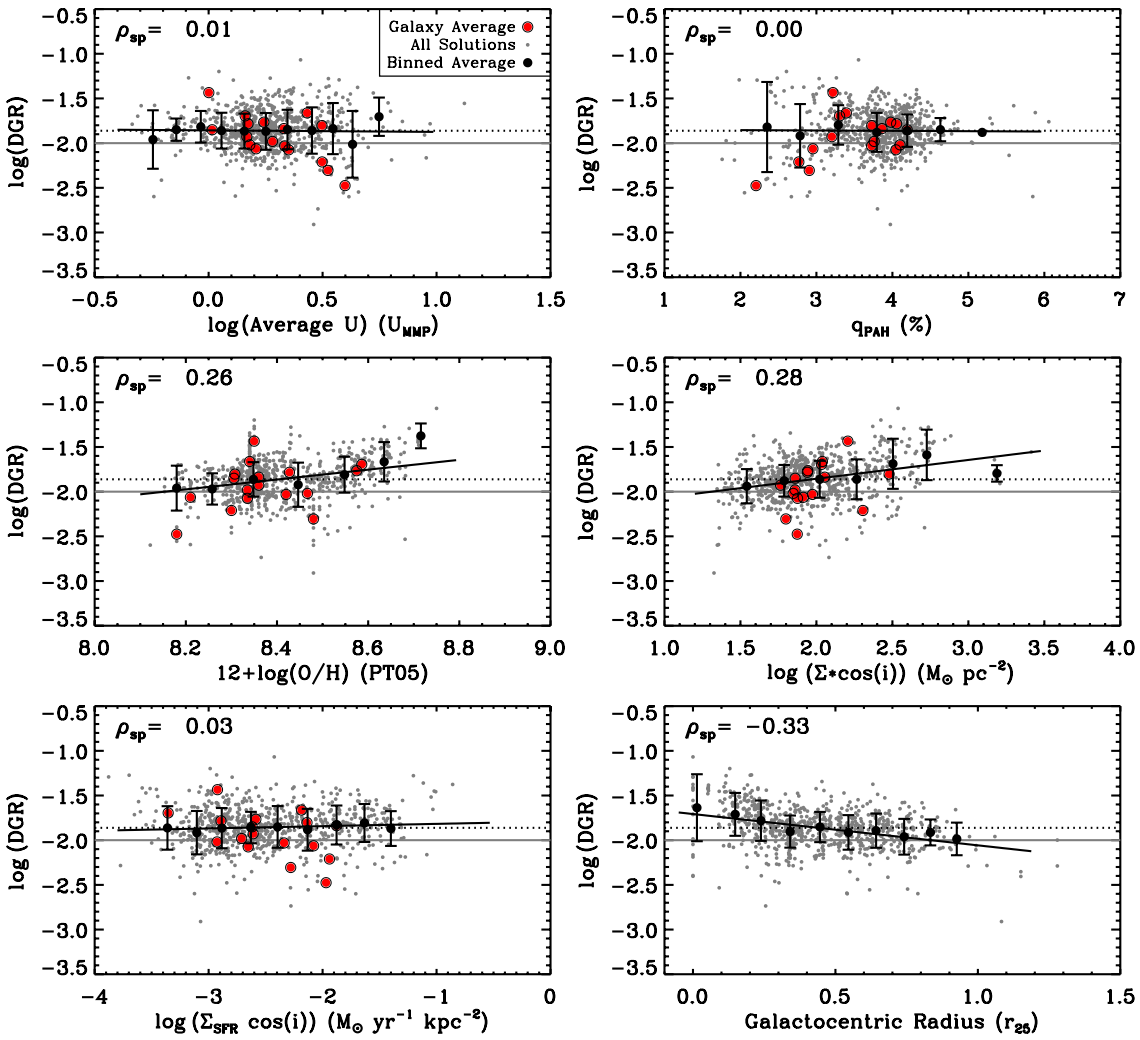

Figure 12. DGR as a function of environmental parameters. The panels show the DGR plotted vs. average radiation field intensity ($\bar{U}$; top left) and PAH fraction ($q_{\rm PAH}$; top right) from the Aniano et al. (2012) fits, metallicity (12 + log(O/H); middle left), stellar mass surface density (Σ_*; middle right), star-formation rate surface density ($\Sigma_{\rm SFR}$; lower left), and galactocentric radius (r_{25}; lower right). The solid gray line shows the Milky Way DGR and the dotted black line shows the sample average. Each individual solution above our $I_{\rm CO}$ and inclination cuts is shown with a gray symbol. The mean and standard deviation of those values in bins are shown with black circles and error bars. A linear fit to the measurements is shown with a black line. The mean values for all galaxies are shown with red circles. The Spearman rank correlation coefficient for each panel is listed in the top left. The DGR shows statistically significant correlations with r_{25}, 12 + log(O/H), and Σ_*.

(A color version of this figure is available in the online journal.)

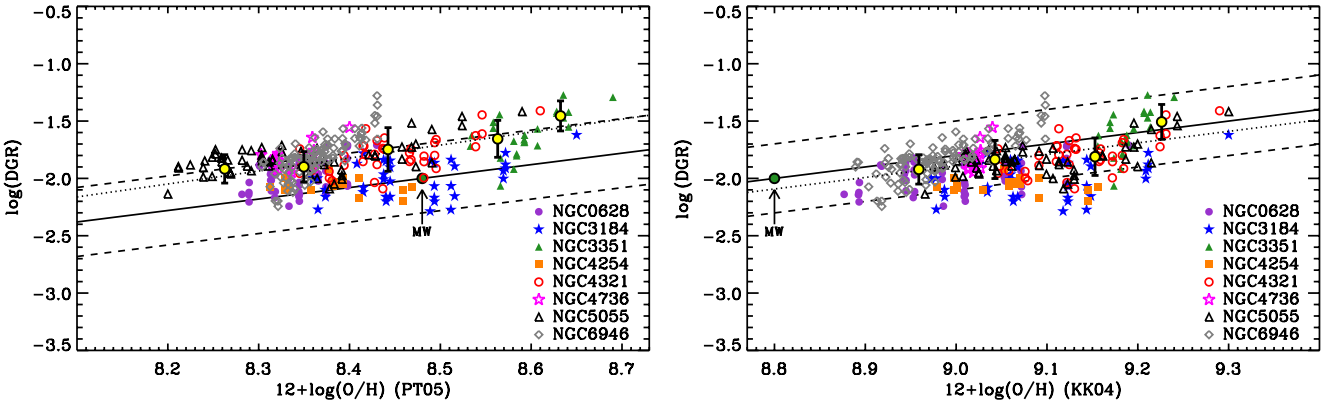

Figure 13. Measured DGR values as a function of metallicity for galaxies with H II region abundance gradients from M10 with the PT05 (left) and KK04 (right) calibrations. Only solutions where the uncertainty in $\alpha_{\rm CO}$ is less than 0.3 dex are shown, although the significance of the correlation between the DGR and Z is relatively unchanged if all points are included. A linear fit to DGR(Z) is overlaid with a dotted black line. There is a clear correlation of the DGR with Z. The best-fit slope is slightly below linear, but if NGC 3184 is removed the correlation is consistent with a linear relationship. The yellow circles show the mean DGR in bins of 0.1 dex in metallicity with error bars representing the standard deviation in those bins. The solid black line shows a linear scaling of the MW DGR and metallicity, with dashed lines above and below showing a factor of two difference from the MW. On the PT05 scale, our sample appears to have a higher DGR for a given metallicity compared to the MW, while the opposite is true on the KK04 scale.

(A color version of this figure is available in the online journal.)

used strong-line abundance measurements calculated from the integrated spectrum of the Orion Nebula.

The best linear fit to the data is shown with a dotted line in both the PT05 and KK04 panels. This fit is parameterized by the following equation, where uncertainties have been determined using bootstrapping:

$$\log(\mathrm{DGR}) = a + b(12 + \log(\mathrm{O/H}) - c). \quad (4)$$

For the PT05 measurements, we find the following constants:

$$a = -1.86 \pm 0.01$$
$$b = 0.85 \pm 0.11$$
$$c = 8.39.$$

For the KK04 measurements, the constants are:

$$a = -1.86 \pm 0.01$$
$$b = 0.87 \pm 0.11$$
$$c = 9.05.$$

In these equations, the constant c is the mean metallicity of the sample of points. We use this parameterization in order to avoid covariance in the offset (a) and slope (b). In both cases, the slope is below unity. It can be seen in Figure 13 that the flatter-than-unity slope is mainly due to NGC 3184 (blue stars). Leaving this galaxy out of the fits produces slopes of 1.13 ± 0.10 and 1.01 ± 0.11 for the PT05 and KK04 calibrations, respectively. Omitting this galaxy also increases the significance of both correlations by 1σ–2σ.

We note that it is necessary to use the same strong-line metallicity calibration that we have (i.e., KK04 or PT05) in order to predict the DGR (or α_{CO}) using our fits. To the extent that applying our DGR(Z) relation is merely an interpolation over a given metallicity range, there is relatively little uncertainty introduced in the process. Any systematic errors in the metallicity scale itself are minimized if the same scale is used in the calibration and the application.

5. COMPARISON TO THE LITERATURE

5.1. Measurements of α_{CO} in the Milky Way and Nearby Galaxies

The local region of the MW is seen to have a conversion factor close to $\alpha_{\mathrm{CO}} = 4.4\ M_{\odot}\ \mathrm{pc}^{-2}\ (\mathrm{K\ km\ s}^{-1})^{-1}$. This standard value has been recovered to within a factor of two by various techniques: γ-ray measurements (Digel et al. 1996; Abdo et al. 2010); virial masses (Solomon et al. 1987); and dust (Dame et al. 2001; Pineda et al. 2008; Planck Collaboration et al. 2011b). A number of studies of the Galactic center, however, have found very different answers. Using γ-ray observations, Strong et al. (2004) found evidence that α_{CO} in the Galactic center was a factor of 5–10 lower than in the disk. Similar results using dust as a tracer for total gas mass have been found by Sodroski et al. (1995), who suggest that α_{CO} is lower by a factor of 3–10. Dahmen et al. (1998) modeled multiple ^{12}CO, ^{13}CO, and C^{18}O lines and found that the standard conversion factor from the disk overestimated the molecular gas mass in the Galactic center by an order of magnitude. Thus, several independent measurements suggest that the MW has a α_{CO} value near its center that is between 3 and 10 times lower than that in the solar neighborhood. The properties of the transition from the standard disk value to this lower number are not well constrained, although γ-rays provide some hint of a gradient (Strong et al. 2004).

The agreement among the various techniques in the Galactic center provides confidence in the resulting low α_{CO}. On their own, each technique is subject to a number of important systematic uncertainties. For γ-ray modeling, a key limitation is our knowledge of the cosmic ray distribution. In the case of multi-line modeling approaches, it is not clear that the approximations involved adequately represent the variety of excitation conditions in the molecular gas (Mao et al. 2000; Bayet et al. 2006). Virial mass-based techniques rely on the assumption that the clouds are in virial equilibrium, with gravity opposed primarily by turbulent motions. If magnetic stresses and thermal pressures are significant, or if GMCs are actually not self-gravitating, the virial technique may fail to reflect the true conversion factor, particularly in regions like the Galactic center (e.g., Dahmen et al. 1998).

Measurements of α_{CO} using various techniques in nearby galaxies have provided somewhat contradictory results. Virial mass studies of GMCs in nearby galaxies tend to find α_{CO} values very similar to the MW disk (Wilson 1995; Bolatto et al. 2008), even in galaxy centers (Donovan Meyer et al. 2012) and in low-metallicity galaxies like the SMC (Bolatto et al. 2008). In contrast, a number of studies using dust-based techniques have found very high α_{CO} values in low-metallicity galaxies, suggesting substantial amounts of "dark molecular gas" or "CO-free H_2" around GMCs (Israel 1997; Dobashi et al. 2008; Leroy et al. 2009a, 2011). Leroy et al. (2011) used dust to trace the total amount of gas and determine α_{CO} for the major galaxies of the Local Group. Their results suggested that (1) at low metallicity, α_{CO} can be well above the standard MW value, (2) in the central few kiloparsecs of M31, the conversion factor was slightly lower than the standard value, and (3) the 10 kpc ring of M31, M33, and the LMC (which collectively span ~0.5 dex in metallicity) all showed α_{CO} values in agreement with the MW value. Studies of the centers of several nearby galaxies with "large velocity gradient" (LVG) or related modeling have found evidence for α_{CO} up to an order of magnitude lower than the MW value (e.g., Weiß et al. 2001; Israel 2009a, 2009b).

The study presented here is the first to create maps of α_{CO} in galaxies outside the Local Group. Therefore, we are able to study α_{CO} across a range of environments and connect the various trends that have been found in previous works. We find that for $I_{\mathrm{CO}} > 1\ \mathrm{K\ km\ s}^{-1}$, α_{CO} is relatively constant for a range of radii and metallicities in galaxies. In the central ~kiloparsec, we observe that galaxies often show a lower-than-average α_{CO} value, sometimes by up to factors of 10. These low α_{CO} values we find in several galaxy centers are not unprecedented, given the results from multi-line modeling studies and the evidence that the Galactic center shows a similar depression. Our lowest metallicities are still above the transition abundance seen by Leroy et al. (2011), where galaxies in the Local Group began to display much higher α_{CO} (i.e., $12 + \log(\mathrm{O/H}) \lesssim 8.2$). The picture that emerges from the synthesis of these literature results is one where α_{CO} is generally around the standard MW value with a factor of ~2 variability in the disks of galaxies, in the regime where CO is bright and metallicity is greater than $\sim 1/2\ Z_{\odot}$, with some galaxies showing lower α_{CO} in their central kiloparsec.

5.2. Direct Comparison of α_{CO} with Virial Mass Measurements

In several cases, our α_{CO} measurements overlap with previous ^{12}CO $J = (1\text{–}0)$ virial mass based studies. Bolatto et al. (2008) derived GMC properties and virial masses for NGC 2976 and

Table 10
Literature α_{CO} Measurements

Galaxy	Regan et al. (2001)	3σ Below MW	Literature α_{CO} Measurements	
	Central Excess?	α_{CO} (This Study)	Type	Reference
NGC 0628	N	N		
NGC 2976	...	N	VM	B08
NGC 3077	...	N	VM	B08
NGC 3351	Y	Y		
NGC 3521	N	N		
NGC 3627	Y	Y		
NGC 4321	Y	Y		
NGC 4631	...	N	ML	I09
NGC 4736	Y	Y	VM	DM13
NGC 5055	Y	N[a]		
NGC 6946	Y	Y	VM, ML	DM12a, IB01, MT04, W02
NGC 7331	N	N	ML	IB99

Notes. VM: virial mass; ML: multi-line modeling.
[a] 2.6σ below MW α_{CO}.
References. B08: Bolatto et al. (2008); DM12a: Donovan Meyer et al. (2012); DM13: Donovan Meyer et al. (2013); I09: Israel (2009b); IB99: Israel & Baas (1999); IB01: Israel & Baas (2001); M01: Meier et al. (2001); MT04: Meier & Turner (2004); R01: Regan et al. (2001); W02: Walsh et al. (2002).

3077. Their results for NGC 3077 are in good agreement with previous studies by Meier et al. (2001) and Walter et al. (2002). Recently, Donovan Meyer et al. (2012) and Donovan Meyer et al. (2013) determined α_{CO} in the central regions of NGC 6946 and 4736, respectively, using virial masses. In Table 10, we provide a summary of the galaxies in our sample with existing literature measurements. Figure 14 shows a comparison between these literature virial mass-based α_{CO} measurements with the values derived in this study. In almost all cases, we find a lower α_{CO} using the dust-based technique than the virial mass technique.

For NGC 2976, Bolatto et al. (2008) found conversion factors ~4 times larger than the MW value, on average. Almost all of our measurements for NGC 2976 show α_{CO} being consistent with the MW value, within their uncertainties. The central solution pixel has α_{CO} a factor of 4–5 below the MW value. In contrast, the virial mass and dust-based techniques are in agreement for NGC 3077, both returning a conversion factor consistent with that of the MW. The center of NGC 6946 stands out in our study as a place with a particularly low α_{CO}. However, virial mass measurements find α_{CO} more consistent with the MW value. Figure 14 illustrates that the discrepancy decreases with radius for NGC 6946—many of the points with galactocentric radii closer to $r_{25} \sim 0.2$ agree with our dust-based measurements. We will discuss the discrepancy between the virial and dust-based α_{CO} values in galaxy centers further in Section 6.3. It is interesting to note that the normalcy of NGC 3077, currently undergoing a starburst, compared to the also highly star-forming centers of 4736 and 6946, suggests that conditions other than just high star-formation surface density must contribute to determining α_{CO}.

5.3. Direct Comparison with Multi-line Modeling Techniques

The center of NGC 6946 has been observed extensively in molecular gas lines and modeled in a variety of ways. Israel & Baas (2001) modeled ^{12}CO and ^{13}CO lines plus [C I] (492 GHz) observations and found a conversion factor ~10 times lower than the MW value in the center. Using LVG modeling of multiple CO isotopomers including $^{12}C^{18}O$, Walsh et al. (2002) found a conversion factor 4–5 times below the MW value. Similarly, Meier & Turner (2004) used an LVG analysis of $C^{18}O$ observations, in addition to multiple CO lines, to argue that the central region had a conversion factor four times below the MW value. All of these studies suggest a central α_{CO} between 4–10 times lower than the MW value, in good agreement with what we observe with dust, but in contrast with the virial mass results.

Several other galaxies in our sample have been modeled with multi-line techniques, however they are at high inclination and therefore do not have reliable α_{CO} measurements from our work. Israel (2009b) used multiple ^{12}CO and ^{13}CO lines plus [C I] (492 GHz) observations toward the central region of NGC 4631 to constrain α_{CO} and found a value six times lower than the standard MW value. Similarly, Israel & Baas (1999) argued for $\alpha_{CO} \sim 5$ times lower than the MW value in the center of NGC 7331. In both of these highly inclined galaxies, we find α_{CO} a factor of two or more higher than the MW α_{CO}. This result is due to the failure of our technique at high inclinations.

5.4. Comparison with CO Exponential Disk Profiles

Regan et al. (2001) found that approximately half of their sample of galaxies observed in the BIMA SONG survey showed excess CO emission in their centers compared to the extrapolation of their best-fit exponential disk profile. They argued that this result could be due to enhanced reservoirs of molecular gas in the centers or a change in the conversion factor. Table 6 lists the central excess classification for the galaxies in our sample studied by Regan et al. (2001). Indeed, we find that in every case where these authors found excess CO above the exponential profile, we find a conversion factor significantly below the MW value. Conversely, for the three galaxies we have observed and that they found to *not* have an excess, we find conversion factors consistent with the MW value or slightly higher. Similar results are found when comparing with the radial profiles determined from the HERACLES CO maps we utilize in this study (see radial profiles in Schruba et al. 2011). In general, the offset between the central α_{CO} and galaxy average α_{CO} from our measurements is similar in magnitude to the excess observed at the centers compared to the extrapolated exponential disk profile.

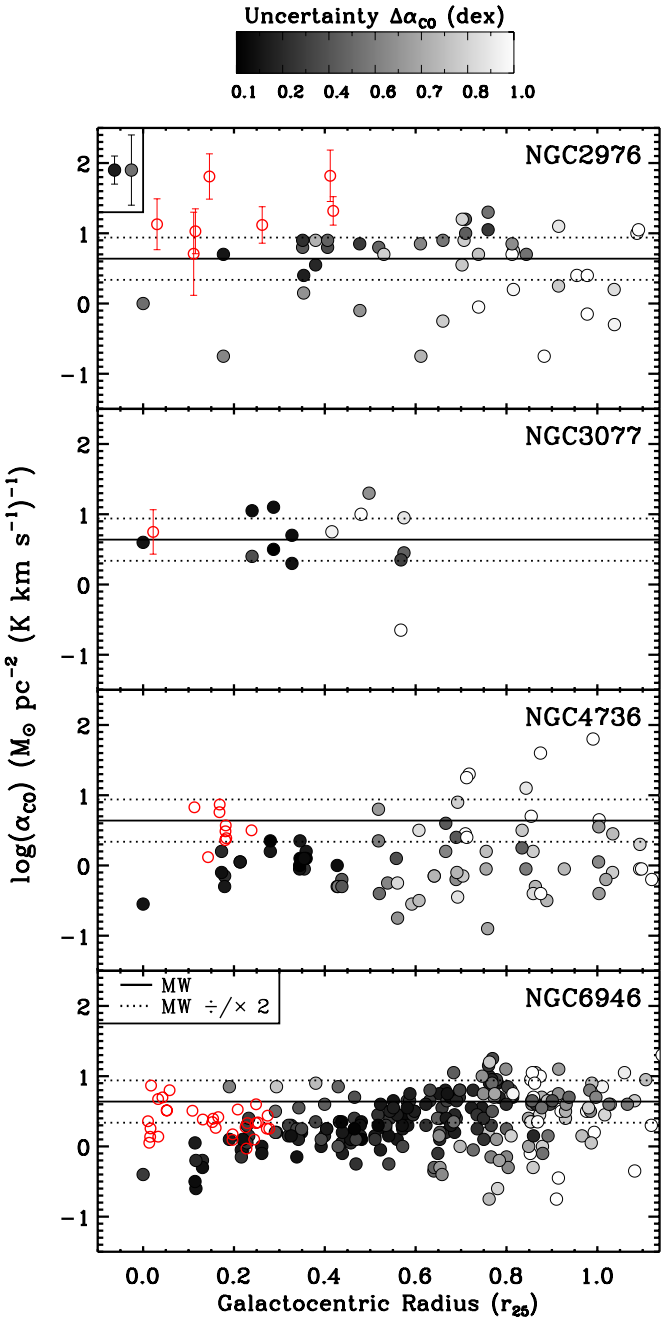

Figure 14. Comparison between virial mass-based measurements of α_{CO} from the literature (shown with red circles) and the results of this study. The gray-scale color table for the points from this study shows the uncertainty on each α_{CO} measurement, as in Figure 4. Sample error bars for comparison with the gray-scale color table are shown in the top left corner of the top plot. Virial mass α_{CO} measurements for NGC 2976 and 3077 are taken from Bolatto et al. (2008). Measurements for NGC 4736 and 6946 are from Donovan Meyer et al. (2013) and Donovan Meyer et al. (2012), respectively. For all of the targets, except NGC 3077, there is a discrepancy between the virial mass and the dust-based α_{CO}. At larger radii, the two measurements are in better agreement in NGC 6946.

(A color version of this figure is available in the online journal.)

6. DISCUSSION

6.1. Drivers of α_{CO} Variations

In the following, we explore the correlations or lack thereof between α_{CO} and parameters that may influence it. Since our resolution elements are large compared to an individual GMC, our α_{CO} value is an average over a population of GMCs, including any molecular gas that may be in a more diffuse phase and not in self-gravitating clouds.

For an individual, self-gravitating, turbulence-supported molecular cloud, there are several key parameters that influence α_{CO}: the density and temperature of the gas and the fraction of the mass that exists in the "CO-dark" phase (where H_2 self-shields and CO is photodissociated). The general dependence of α_{CO} on density and temperature can be illustrated using a simple model—a spherical, homogeneous cloud where self-gravity is opposed primarily by turbulence and ^{12}CO $J = (1–0)$ is optically thick. Following the derivation in Draine (2011),

$$\alpha_{CO} = 3.4 n_3^{0.5} (e^{5.5/T_{ex}} - 1)\ M_\odot\ \mathrm{pc}^{-2} (\mathrm{K\ km\ s^{-1}})^{-1}. \quad (5)$$

Here, n_3 is the H nucleon density $n_H = 10^3 n_3$ cm^{-3} and T_{ex} is the excitation temperature. Real molecular clouds are certainly not spherical and homogenous, but this model allows us to understand the basic dependence of α_{CO} on density and temperature (note that simulated molecular clouds with a non-spherical, non-homogenous structure show similar basic scalings; Shetty et al. 2011). Molecular clouds with increased density will have higher α_{CO} while clouds with increased temperature will have lower α_{CO}.

Because CO is optically thick at solar metallicity, the abundance of C or O does not directly influence α_{CO}. However, metallicity may indirectly influence α_{CO} by altering the density or temperature structure of the gas, since the heating and cooling rates may be affected by metallicity or correlate with metallicity. At lower metallicities, the transition between ionized and neutral carbon to CO may shift relative to the H I/H_2 transition due to a lack of dust shielding, leading to layers of "CO-dark" H_2 (Tielens & Hollenbach 1985; van Dishoeck & Black 1988; Wolfire et al. 1993; Kaufman et al. 1999; Bell et al. 2006). α_{CO} will increase when there are significant amounts of gas in these layers. Recent work by Wolfire et al. (2010) used PDR modeling and a spherical model for a turbulent molecular cloud to study variations in the conversion factor. These authors found that the "dark molecular gas" fraction (i.e., the fraction of the molecular cloud mass where H_2 exists but CO is photodissociated) depends primarily on the extinction through the cloud or the DGR. Studies of simulated molecular clouds have also found a dependence of α_{CO} on extinction through the cloud (Glover & Mac Low 2011).

The simple model we have described above assumes that the cloud's self-gravity is balanced by turbulence. If there are other forces that contribute to the virial equation, α_{CO} may be altered. For a self-gravitating cloud, an increase in the pressure on the surface of the cloud will lead to a larger velocity dispersion. Because CO is optically thick, the amount of emission that "escapes" in the CO line is directly tied to the velocity dispersion of the cloud and increasing the velocity dispersion increases the CO emission for the same mass of H_2. Therefore, if a self-gravitating cloud were subject to significant external pressure, we would expect a lower α_{CO}. Conversely, if magnetic fields play an important role in supporting the cloud, this effect would lower the velocity dispersion and raise α_{CO}. In ultra-luminous infrared galaxies (ULIRGs), the molecular gas may not be in individual self-gravitating clouds, but instead in a large-scale molecular medium where stellar mass contributes to the gravitational potential (e.g., Downes & Solomon 1998). In this case, the velocity dispersion is larger than what would be expected from the gas mass alone and the CO emission is enhanced for a given gas mass (resulting in a lower α_{CO}).

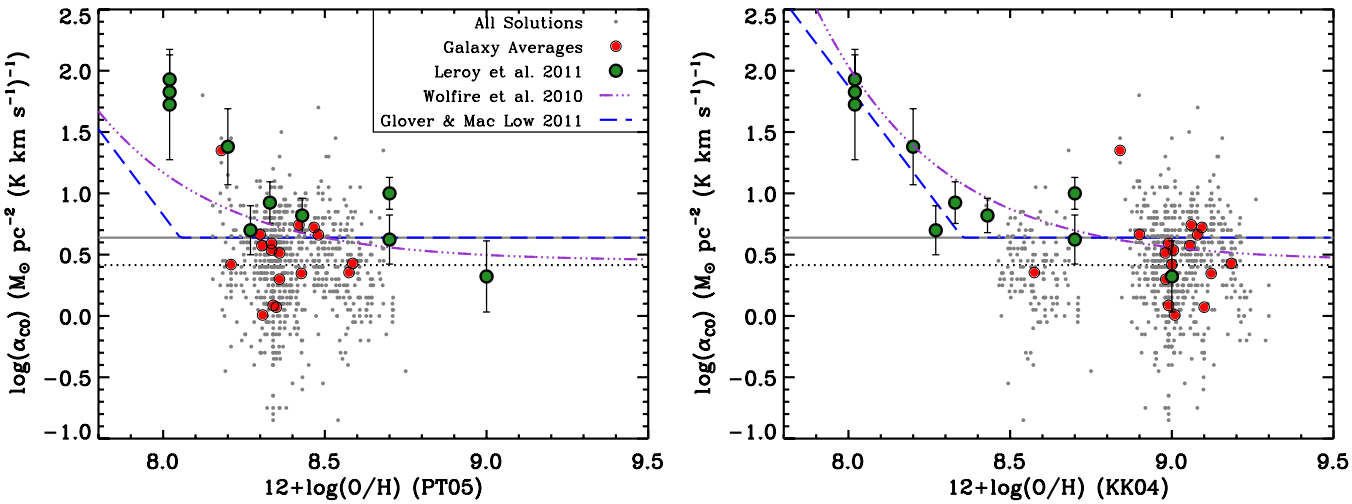

Figure 15. α_{CO} as a function of metallicity compared to previous measurements and models. The left panel shows measurements with the PT05 calibration while the right panel shows measurements with the KK04 calibration. Measurements from this paper are shown as gray points (individual solutions) and red circles (galaxy averages). We show all of the solution pixels where $I_{CO} > 1$ km s^{-1} and $i > 65°$, regardless of the source of the metallicity measurement (i.e., without the requirement of having measured H II region metallicities from M10). Measurements of α_{CO} in Local Group galaxies from Leroy et al. (2011) are shown with green circles. The MW α_{CO} is shown with a gray line and the average of our solution pixels with no weighting is shown with a dotted black line. Predictions based on the model of Wolfire et al. (2010) are shown with a purple dot-dashed line and those based on Glover & Mac Low (2011) are shown with a dashed blue line. These predictions assume a linear dependence of the DGR on metallicity and a fixed gas mass surface density for molecular clouds of $\Sigma_{GMC} = 100\ M_\odot$ pc^{-2}. The model predictions are normalized to have $\alpha_{CO} = 4.4\ M_\odot$ pc^{-2} (K km s^{-1})$^{-1}$ at the metallicity adopted for the Milky Way in each calibration. Note that the metallicities we use for NGC 5457 are not from strong-line calibrations, so they appear in the same position in both plots. Regardless of the metallicity calibration, our measurements do not extend to low enough metallicities to constrain the effects of "CO-dark" H_2.

(A color version of this figure is available in the online journal.)

In a ∼kiloparsec region of a galaxy, many individual molecular clouds will be averaged together in our measurement. Therefore, another factor that could contribute to the variation of our measured α_{CO} is changes in the cloud populations. In addition, any significant component of diffuse CO emission would be included as well. Several studies have suggested that CO emission from diffuse gas may not be negligible, even in the local area of the MW (Liszt & Lucas 1998; Goldsmith et al. 2008). Interestingly, it appears that locally, α_{CO} is similar in diffuse molecular gas and self-gravitating GMCs (Liszt et al. 2010). Recent work by Liszt & Pety (2012) has shown that under differing environmental conditions, the conversion factor appropriate for diffuse gas can vary substantially. Therefore, depending on the amount of diffuse molecular gas and the local conditions in a galaxy, α_{CO} may be very different from what is observed in the local area of the MW. The contribution of diffuse molecular gas with a different α_{CO} has been cited previously as a cause for discrepancies between different techniques for measuring α_{CO} in M51 (Schinnerer et al. 2010).

To summarize our theoretical expectations, α_{CO} measured in ∼kiloparsec regions of nearby galaxies can vary as a function of environment for many reasons: changes in the excitation temperature and density of the gas or contributions from pressure or magnetic support in self-gravitating clouds; envelopes of "CO-dark" gas; changes in the molecular cloud population; or contributions from diffuse CO emission. Unfortunately, directly measuring temperature, density, and velocity dispersion in large samples of extragalactic GMCs is challenging due to the need to resolve individual clouds in multiple molecular gas emission lines. Therefore, we are left with more indirect tracers of changes to the GMC properties. In Section 4.6, we examined the correlation of α_{CO} with $\overline{U}$, q_{PAH}, metallicity, Σ_*, Σ_{SFR}, Σ_D, and galactocentric radius.

The average radiation field $\overline{U}$, measured from the dust SED, could influence α_{CO} through the gas excitation temperature. If photoelectric heating dominates over other heat sources (e.g., cosmic rays) at the $\tau_{CO} \sim 1$ surface, then the intensity of the radiation field may play a role in determining T_{ex} (Wolfire et al. 1993). Likewise, q_{PAH} and metallicity could both influence the efficiency of the photoelectric effect (Bakes & Tielens 1994; Röllig et al. 2006), thereby changing the heating rate. We expect that Σ_{SFR} should be responsible for higher $\overline{U}$ in many regions. Enhanced SFRs leading to higher radiation field intensities has been suggested as the explanation for the observed high α_{CO} in several outer-disk molecular clouds in M33 (Bigiel et al. 2010). If the gas excitation temperature were affected by the radiation field or photoelectric heating, we would expect negative correlations (i.e., lower α_{CO} at higher $\overline{U}$, Σ_{SFR}, q_{PAH}, etc.). The correlations we observe between α_{CO} and $\overline{U}$, q_{PAH}, and Σ_{SFR} are generally weak. $\overline{U}$ and α_{CO} show the strongest association and the slope of the trend is negative, with lower α_{CO} at higher $\overline{U}$. This result is consistent with the expectation of higher radiation field intensities leading to warmer molecular gas temperatures, but the correlation is weak and other variables may play a more important role.

We see a weak trend of α_{CO} with metallicity. Since our observations are limited to regions with metallicities similar to or higher than that of the MW, we may not expect to see a strong correlation between α_{CO} and metallicity. The fraction of gas mass in the layer where CO is photodissociated is predicted to be ∼30% at the MW metallicity/DGR (Wolfire et al. 2010). Thus, increasing the DGR should only have a minimal effect on the conversion factor at MW metallicity and above. To illustrate this point, in Figure 15 we plot our α_{CO} measurements as a function of metallicity and overlay the Leroy et al. (2011) Local Group measurements and the models of Wolfire et al. (2010) and Glover & Mac Low (2011). The model predictions are normalized to $\alpha_{CO} = 4.4\ M_\odot$ pc^{-2} (K km s^{-1})$^{-1}$ at the MW metallicity (i.e., $12 + \log(O/H) = 8.5$ in PT05 and 8.8 in KK04; from the Orion Nebula). Both models assume a linear scaling of

the DGR with metallicity and a fixed gas mass surface density for molecular clouds. The model predictions are discussed in detail in Leroy et al. (2013). In both calibrations, our measurements do not extend into the regime where "CO-dark" H_2 dominates α_{CO}. We note that an investigation of the α_{CO}–DGR relationship using our results would require taking into account the strong correlation of the uncertainties in these parameters.

The strongest correlation we observe for α_{CO} is that with Σ_*. This correlation is the only one that is stronger than the correlation of α_{CO} with galactocentric radius r_{25}. In essence, our definition of r_{25} is based on a scale length of the stellar disk, defined by a B-band surface brightness, so it is possible the stronger correlation of α_{CO} with Σ_* is due to it being a better proxy for the disk scale length than r_{25}. In addition, of the environmental parameters we have available for our analysis, Σ_* is the most straightforward to measure and may show the smallest systematic uncertainties. α_{CO}/Σ_* may be the strongest correlation simply because the other parameters are more uncertain. The question remains, however, as to why α_{CO} would correlate with the stellar mass surface density. There are a number of possibilities: pressure contributions to GMC virial balance, enhanced fractions of diffuse CO emission correlated with ISM pressure, changes to the population of GMCs, or other effects. We do not speculate here about what causes this correlation, but rather note that observations of multiple molecular gas lines at GMC resolution will help understand these trends and are possible with ALMA.

Although we see some evidence for weak correlations between α_{CO} and environmental variables, it is not possible with this dataset to distinguish the cause of these variations. Our primary result is that in regions with $I_{CO} > 1$ K km s^{-1} in these galaxies, α_{CO} is mostly insensitive to environment except in the central regions. This result may be due to our limited S/N for each individual α_{CO} measurement plus the relatively small range of environmental conditions we probe. Another possibility is that in the disks of most galaxies, the properties of molecular gas are insensitive to environment because most of the gas resides in molecular clouds that are not under significant external pressure or subject to enhanced turbulence or magnetic fields. The conversion factor appropriate for such clouds should be similar to the standard MW value.

6.2. Comparison with Galaxy Simulations

Because of the resolution of our observations, our measurements average over a population of molecular clouds. This result means that environmental variations in the cloud population can also be responsible for changes in α_{CO}. Therefore, it is interesting to compare our results to what has been found with galaxy simulations, despite the fact that these simulations are forced to adopt a sub-grid model that prescribes α_{CO} for unresolved clouds. In Figure 16, we show our measured α_{CO} values as a function of the average I_{CO} in each solution pixel. Due to our completeness cut, we have no points below 1 K km s^{-1}. The mean and standard deviation of the α_{CO} measurements in bins of 0.25 K km s^{-1} are shown with black circles and error bars.

Overlaid on Figure 16 we show the predictions of two recent simulations. Feldmann et al. (2012, F12) couples full galaxy simulations with the Glover & Mac Low (2011) cloud-based conversion factor predictions assuming a fixed gas temperature and either a constant line width of 3 km s^{-1} or a virial scaling. The Narayanan et al. (2012, N12) predictions include sub-grid semi-analytic models for the chemical and thermal state

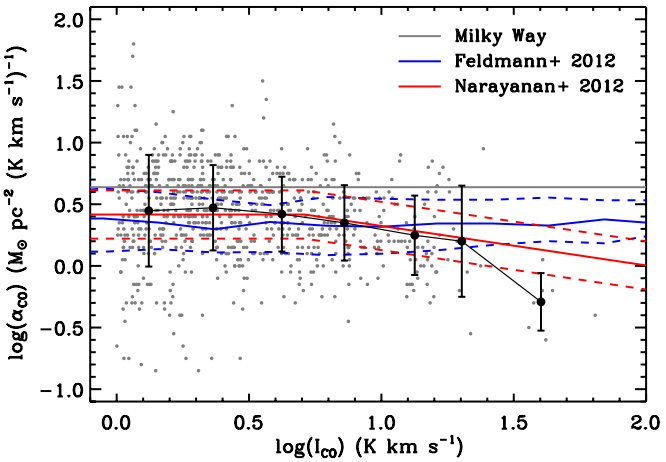

Figure 16. A comparison between our α_{CO} measurements and the predictions of simulations by Narayanan et al. (2012) and Feldmann et al. (2012). On the x-axis, we show the average I_{CO} in a given solution pixel. All solutions above our I_{CO} and inclination cuts are shown as gray circles. The simulation predictions are shown at three possible metallicities: $Z = Z_\odot$ in a solid line and a factor of two above and below that with dashed lines (for Feldmann et al. (2012) we show $Z = Z_\odot$, $3 \times Z_\odot$, and $0.3 \times Z_\odot$). The mean and standard deviation in 0.25 K km s^{-1} bins are shown with black circles and error bars. The predictions from the simulations have been divided by a filling factor of three to correct for our different resolutions. In general, the average behavior of our α_{CO} measurements agrees well with the predictions of these models except at the highest I_{CO}.

(A color version of this figure is available in the online journal.)

of the gas and dust. In the N12 models, the temperature of the molecular gas is not fixed and depends on heating by cosmic rays and, in dense regions, on energy transfer with dust. For both models, it is necessary to adopt a filling factor or clumping correction due to the difference in resolution between the simulations and our observations. The simulations of F12 and N12 both have ~60–70 pc resolution, so we apply the same correction to both. For purposes of comparing with the trend of our observed α_{CO} as a function of CO integrated intensity, we have adopted a filling factor correction of three. This correction factor is larger than purely the ratio of the resolutions because our beam will contain more than one molecular cloud. Verifying that this absolute scaling is correct would require a more detailed investigation that is beyond the scope of this paper.

We find that the predicted trends of α_{CO} with CO integrated intensity from N12 and F12 match the average observed behavior well, although both underpredict α_{CO} in the central regions of some galaxies. There is considerable scatter around this trend, however. F12 argue that on ~kiloparsec scales metallicity is the primary driver of the conversion factor variations. This metallicity dependence reflects, to first order, the Glover & Mac Low (2011) dependence between α_{CO} and extinction through the cloud with the addition that F12 assume a metallicity-dependent DGR. Our α_{CO} results do not show a strong dependence on metallicity, but may not extend to low enough metallicities to clearly distinguish such variations. N12 do see a decrease in α_{CO} in regions with high SFR surface densities due to enhanced gas temperatures and velocity dispersions, similar to what we have found in some galaxy centers.

6.3. Low Central α_{CO} and Discrepancies with Virial Mass Based Measurements

For some galaxy centers in our sample, we measure α_{CO} values lower than the typical MW value by factors of 5–10. In-

terestingly, the virial mass-based α_{CO} measurements for several of these regions do not agree with the values found here, instead recovering α_{CO} values close to that of the MW. From Figure 14, we found that the discrepancy between virial mass and dust-based α_{CO} decreases with radius for NGC 6946—suggesting that this discrepancy is a property of the galaxy centers rather than an issue with the resolution of the virial mass techniques (which tends to be comparable to the size of the GMCs). For NGC 6946, results of multi-line modeling studies are generally in much better agreement with our results. In the following, we discuss processes that could lower α_{CO} measured from dust and multi-line modeling techniques, while leaving virial mass-based α_{CO} values similar to those of the MW.

For self-gravitating GMCs, all three techniques should derive a lower α_{CO} if the gas excitation temperature were changing independently of the other variables. In contrast, if the velocity dispersion of the cloud changed due to external pressure or additional sources of turbulence, the virial and dust techniques could arrive at different results. In such a situation, the measured line width would suggest a larger virial mass and the cloud's CO emissivity would also increase. Thus, one could derive a conversion factor similar to the MW value from the comparison of CO to virial mass since both have increased. Oka et al. (1998a) have suggested that external pressure in the Galactic center can account for up to an order of magnitude change in the conversion factor. However, Donovan Meyer et al. (2012) found that GMCs in NGC 6946 did not generally show enhanced velocity dispersions at a given size or luminosity, in contrast to the Galactic center clouds identified by Oka et al. (1998b). At the resolution of our CO maps, we cannot distinguish between changes in GMC internal velocity dispersion (which would affect α_{CO}) and changes in the velocity dispersion within the population of clouds, so we cannot test whether there is enhanced velocity dispersion in GMCs with our measurements.

It is possible that molecular gas in the centers of some galaxies is not in self-gravitating GMCs. If that is the case, the velocity dispersion may reflect other hydrodynamical processes and the virial mass estimate will be incorrect. For instance, if the molecular gas is not in GMCs but rather in a larger-scale molecular medium that is gravitationally bound to the stars and gas, the velocity dispersion will be larger and more CO emission will be produced for a given amount of gas. This explanation has been suggested by Downes et al. (1993) and Downes & Solomon (1998) to explain the properties of molecular gas in the nuclear disks of ULIRGs (see also recent work by Papadopoulos et al. 2012). Another option is a contribution to the CO emission from diffuse molecular gas, which could potentially have a lower α_{CO} than GMCs (Liszt et al. 2010).

The dust-based and multi-line modeling α_{CO} results may agree better than the virial results in galaxy centers because they do not assume a relationship between the velocity dispersion and the mass of molecular gas, which would cause issues in the cases outlined above. At the moment, only NGC 6946 (out of our $i < 65^{\circ}$ galaxies) has both virial and multi-line modeling results. In the other galaxies, we may be able to find some indication of how optical depth, excitation, and velocity dispersion affect α_{CO} by examining the ratios of ^{12}CO and ^{13}CO lines. A. Usero et al. (in preparation) present measurements of ^{13}CO and ^{12}CO lines toward regions of several HERACLES galaxies. Selecting all of their pointings toward the disks of galaxies in our sample (in regions above our I_{CO} and inclination cuts), the uncertainty weighted mean of $R_{12/13} = {}^{12}\mathrm{CO}\ J = (1\text{–}0)/{}^{13}\mathrm{CO}\ J = (1\text{–}0)$ is 8.24 ± 0.11. The only galaxy centers with ^{13}CO measurements are NGC 0628, 3184, 5055, and 6946. NGC 0628, 3184, and 5055 show $R_{12/13}$ values consistent with or slightly lower than the average disk value. NGC 6946, on the other hand, has $R_{12/13} = 18.53 \pm 0.81$. The high $R_{12/13}$ for the center of NGC 6946 has been noted in several previous studies (Paglione et al. 2001; Israel & Baas 2001; Meier & Turner 2004).

6.4. Dust-to-gas Ratio

As shown in Figures 12 and 13, we observe a good correlation of the DGR with metallicity. Unlike most previous studies of the DGR resolved within galaxies, we made no assumption about α_{CO} in determining these values. Although we do not probe a wide range of metallicity due to the limitations on CO S/N, it is clear in Figure 13 in particular that the DGR is correlated with metallicity with less than a factor of two scatter over 0.5 dex in metallicity. A linear dependence of the DGR on metallicity suggests a constant fraction of heavy elements are locked up in dust grains. Chemical evolution and dust life-cycle models have varying predictions for the dependence of the DGR on metallicity (Dwek 1998; Lisenfeld & Ferrara 1998; Hirashita et al. 2002). Most of the dramatic differences between the models, however, occur at lower metallicities and observations of dwarf galaxies may provide more leverage on distinguishing between models (e.g., Herrera-Camus et al. 2012).

6.5. Recommendations on Choosing α_{CO}

Due to the requirements on CO S/N to apply the technique we have used, our measurements only tell us about α_{CO} above $I_{CO} = 1$ K km s^{-1} in the galaxies we have targeted. Generally, this requirement limits us to the inner parts of galaxies ($<r_{25}$), where metallicities are comparable to those in the MW disk. However, these are the regions where H_2 contributes most significantly to the total gas mass (Schruba et al. 2011), so applying our conversion factor results to unresolved galaxies should work reasonably well for recovering the total H_2 mass. A forthcoming paper extending our study to the H I dominated regions of the KINGFISH galaxies will test this assertion. Note that our recommendations are only applicable to spiral galaxies with metallicity similar to that of the MW.

For an unresolved galaxy, we recommend adopting our galaxy-based average α_{CO} of 3.1 $M_{\odot}$ pc^{-2} (K km s^{-1})$^{-1}$ with uncertainty of 0.3 dex (a factor of $\sim$2). These values are the mean and standard deviation of the average value for all galaxies with inclinations less than 65°.

In dealing with resolved galaxies, we recommend adopting a flat radial α_{CO} profile for regions with $I_{CO} > 1$ K km s^{-1}, except in the central $\sim 0.1 r_{25}$, where the average α_{CO} is a factor of two lower. When dealing with a single galaxy, our average radial profile from Figure 7 suggest that the α_{CO} values have $\sim$0.2 dex of scatter in each radial bin (0.3 dex for the central bin). Therefore, for studies of molecular gas within a single galaxy, the relative values of α_{CO} adopted from this profile have a factor of $\sim$1.5 uncertainty. When comparing resolved galaxies, it is necessary to further recognize that the absolute normalization of the radial profiles, i.e., the galaxy average value, has an additional 0.3 dex uncertainty.

In the case where additional information about the galaxy is available, such as profiles of stellar mass surface density, SFR surface density, or line ratios of ^{12}CO (2–1)/(1–0) or ^{12}CO/^{13}CO, we suggest using these maps to pick out regions that may have α_{CO} values very different from the mean. These regions have $\Sigma_* \gtrsim 1000\ M_{\odot}$ pc^{-2}, $\Sigma_{SFR} \gtrsim 0.1\ M_{\odot}$ yr^{-1} kpc^{-2}, or $R_{21} \gtrsim 1$ at our working resolution of $\sim$1 kpc. In these regions,

α_{CO} can be 5–10 times lower than the MW α_{CO}, and are often systematically lower than the average radial profile.

7. SUMMARY AND CONCLUSIONS

The availability of high angular resolution far-IR maps from the *Herschel Space Observatory* and sensitive ^{12}CO $J = (2–1)$ and H I maps has recently allowed us to trace dust and gas mass surface densities in nearby galaxies on ∼kiloparsec scales. On these scales, we expect (and have verified) that the DGR is approximately constant. Therefore, we are able to combine the dust mass surface density maps with matched resolution CO and H I data to solve simultaneously for α_{CO} and the DGR. The solution technique finds the α_{CO} that best minimizes the scatter in the DGR values in ∼kiloparsec regions across the galaxies. We have performed a thorough investigation into the efficacy of this technique, using data from the KINGFISH key program on *Herschel*, the large IRAM 30 m survey HERACLES, and the THINGS H I survey with the VLA. Our tests show that above $I_{CO} \sim 1$ K km s^{-1}, we reliably achieve accurate solutions for α_{CO}. We have used a fixed ratio between the (2–1) and (1–0) lines to present our α_{CO} results on the more typically used ^{12}CO $J = (1–0)$ scale and have shown using literature measurements that variations in the line ratio do not affect our results in these galaxies.

We find that the average α_{CO} for the galaxies in our sample is 3.1 $M_\odot$ pc^{-2} (K km s^{-1})$^{-1}$. This value is slightly lower than the MW $\alpha_{CO} = 4.4$ $M_\odot$ pc^{-2} (K km s^{-1})$^{-1}$, but the MW value is well within the standard deviation of our measurements. Treating all 782 solutions independently (instead of weighting each galaxy equally), we find $\alpha_{CO} = 2.6$ $M_\odot$ pc^{-2} (K km s^{-1})$^{-1}$ with 0.4 dex standard deviation. In all averages, we have removed galaxies with inclinations higher than 65° since our solution pixel samples gas along the line-of-sight with a range of DGRs and therefore does not conform to our main assumption—that the DGR is constant in the solution pixels.

Within the galaxies, we observe a relatively flat α_{CO} profile as a function of galactocentric radius aside from in the galaxy centers. Normalizing each galaxy by its average α_{CO}, the average galaxy shows a factor of ∼2 lower α_{CO} in its center. In several galaxies, this central value can be factors of three or more lower than the galaxy average. In several notable cases, the central α_{CO} value is factors of 5–10 lower than the standard MW $\alpha_{CO} =$ 4.4 $M_\odot$ pc^{-2} (K km s^{-1})$^{-1}$.

We have investigated the correlations between α_{CO} and environmental parameters in an attempt to isolate factors that drive variations in α_{CO}. The strongest correlation we find is between α_{CO} and stellar mass surface density (Σ_*). If the strength of this correlation relative to the other parameters is real and not due to issues with measuring the other parameters, there are a number of possible explanations for why α_{CO} should depend on stellar mass surface density. These explanations include the influence of ISM pressure on both molecular clouds and a more diffuse molecular medium. Distinguishing among these possibilities will require ALMA observations that resolve individual GMCs in multiple molecular gas lines across a range of extragalactic environments.

We do not observe a strong correlation between α_{CO} and metallicity in our galaxies. In the range of metallicities we have sampled, this conclusion is not unexpected. The abundance of C or O does not play a major role in determining α_{CO} at these metallicities since CO is optically thick in molecular clouds. The metallicity primarily influences α_{CO} through the effects of dust shielding (due to the dependence of the DGR on metallicity). Models and simulations have suggested that dust shielding can influence the amount of gas in "CO-dark" layers of GMCs, but at MW metallicity, only ∼30% of the gas is in this layer. At lower metallicities, a strong dependence of α_{CO} on metallicity has been observed using the same technique we employ (Leroy et al. 2011).

In the centers of several galaxies, we find α_{CO} values 5–10 times lower than that of the MW α_{CO}. These regions are also significantly below the average α_{CO} for their galaxy. Comparison of our measured α_{CO} with values from the literature shows good agreement between our dust-based results and multi-line modeling results. In contrast, our α_{CO} values in these regions can be much lower than α_{CO} determined from virial mass-based techniques. The discrepancy with virial mass measurements becomes smaller at larger galactocentric radii, suggesting this discrepancy is a particular property of the gas in galaxy centers. At the resolution of our observations, the central region with low α_{CO} is unresolved ($\lesssim$kiloparsec). We suggest several explanations for the low α_{CO} value and the fact that it is not reflected in virial masses: ISM pressure contributions to GMC virial balance, increases in molecular gas temperature, and/or a more diffuse molecular medium similar to what is found in ULIRGs. With the limited amount of ^{13}CO and other molecular line observations in this region, it is not possible to distinguish among these scenarios, but NGC 6946 at least shows some evidence for lower CO optical depth toward its center. As explored in Leroy et al. (2013), these galaxy centers show enhanced star-formation efficiencies when we apply our α_{CO}, close to what is seen along the "starburst sequence" in ULIRGs (e.g., Daddi et al. 2010).

In addition to α_{CO}, we also simultaneously measure the DGR in all of our regions. On average, we find $\log(\mathrm{DGR}) = -1.86$ when all solution pixels are treated equally, with a standard deviation of 0.22 dex. When we force each galaxy to contribute equally, the average is essentially indistinguishable from the MW DGR. Unlike α_{CO}, the DGR is well correlated with metallicity, with a slope slightly shallower than linear (although this slope is mainly due to NGC 3184 being offset from the main trend; removing this object from the sample produces a slope consistent with a linear relation). The approximately linear dependence of the DGR on metallicity agrees with the predictions of dust evolution models, but our measurements do not cover a wide enough metallicity range to distinguish among them.

The results presented here suggest a picture where α_{CO} is slightly lower than the typical value of 4.4 $M_\odot$ pc^{-2} (K km s^{-1})$^{-1}$ in the disks of most galaxies, and mainly constant as a function of radius despite changes in metallicity, radiation field intensity, and SFR surface density. Galaxy centers appear to be a different regime, where external pressure or changes in the character of molecular gas (i.e., mostly confined to self-gravitating GMCs versus a more diffuse molecular medium) may bring about large changes in α_{CO}. Through the galaxy, however, the DGR appears to be an approximately linear function of metallicity. The simple behavior of the DGR provides a unique tool to study the ISM in nearby galaxies, if we can obtain measurements of metallicity gradients with trustworthy calibration.

We thank the referee for useful comments that helped to improve the quality of the manuscript. K.S. thanks R. Shetty, S. Glover, R. Klessen, D. Narayanan, and A. Stutz for helpful conversations. The authors thank R. Feldmann and N. Gnedin

for helpful comments regarding the comparison of our measurements to their simulations. K.S. is supported by a Marie Curie International Incoming Fellowship. A.D.B. wishes to acknowledge partial support from a CAREER grant NSF-AST0955836, NASA-JPL1373858, and from a Research Corporation for Science Advancement Cottrell Scholar award.

This work is based on observations made with *Herschel*. *Herschel* is an ESA space observatory with science instruments provided by European-led Principal Investigator consortia and with important participation from NASA. PACS has been developed by a consortium of institutes led by MPE (Germany) and including UVIE (Austria); KU Leuven, CSL, IMEC (Belgium); CEA, LAM (France); MPIA (Germany); INAF-IFSI/OAA/OAP/OAT, LENS, SISSA (Italy); IAC (Spain). This development has been supported by the funding agencies BMVIT (Austria), ESA-PRODEX (Belgium), CEA/CNES (France), DLR (Germany), ASI/INAF (Italy), and CICYT/MCYT (Spain). SPIRE has been developed by a consortium of institutes led by Cardiff University (UK) and including University of Lethbridge (Canada); NAOC (China); CEA, LAM (France); IFSI, University of Padua (Italy); IAC (Spain); Stockholm Observatory (Sweden); Imperial College London, RAL, UCL-MSSL, UKATC, University of Sussex (UK); and Caltech, JPL, NHSC, University of Colorado (USA). This development has been supported by national funding agencies: CSA (Canada); NAOC (China); CEA, CNES, CNRS (France); ASI (Italy); MCINN (Spain); SNSB (Sweden); STFC (UK); and NASA (USA). HIPE is a joint development by the Herschel Science Ground Segment Consortium, consisting of ESA, the NASA Herschel Science Center, and the HIFI, PACS and SPIRE consortia. This research has made use of the NASA/IPAC Extragalactic Database (NED) which is operated by the Jet Propulsion Laboratory, California Institute of Technology, under contract with the National Aeronautics and Space Administration. This research has made use of NASA's Astrophysics Data System Bibliographic Services.

APPENDIX A

TECHNIQUE FOR SIMULTANEOUSLY DETERMINING THE DGR AND α_{CO}

Prior to choosing the technique described in Section 3, we explored a variety of possible ways to simultaneously constrain the DGR and α_{CO}. The various techniques represent, in essence, different ways to judge how uniform the DGR is in the region in question, at any given value of α_{CO}. After defining these variations on the essential technique, we construct simulated datasets with a known α_{CO} and DGR and realistic statistical errors and intrinsic scatter to test the solution techniques. These simulated data tests allow us to optimize the performance of the technique given the properties of our dataset.

A.1. Potential Techniques

The general procedure for finding the most "uniform" DGR in the solution pixel given spatially resolved measurements of $\Sigma_{H\,I}$, Σ_D, and I_{CO} is to step through a grid of α_{CO} values, calculate the DGR at each sampling point in the solution pixel using that α_{CO}, measure some statistic that can be used to judge how uniform the DGR values are across the region, and, finally, either minimize or maximize that statistic as a function of α_{CO}. Below, we describe the various statistics we have tested to judge the uniformity of the DGR values in a given region. The reason we investigate all of these possible statistics is because each weights outliers differently, and it is not obvious a priori which will work best to recover the underlying α_{CO}. For techniques that involve minimizing scatter in the DGR, we use three different statistics to measure scatter: the standard deviation (RMS), the median absolute deviation (MAD), and a robust estimator of the standard deviation from Tukey's biweight (BIW; Press et al. 2002).

1. *Minimum fractional scatter in the DGR (FS)*. At each value of α_{CO}, we calculate the DGR for all points in the region in question. We then divide each DGR value by the mean DGR in the region and measure the scatter of the resulting values (with RMS, MAD, and BIW statistics).
2. *Minimum logarithmic scatter in the DGR (LS)*. At each α_{CO}, we calculate the scatter of the logarithm of the DGR values (with RMS, MAD, and BIW). This technique is similar to the minimization of fractional scatter, but with a different weighting for the individual points. This method also throws away data points with negative values, since their logarithm is undefined.
3. *Maximum correlation coefficient of* Σ_D *and* Σ_{Gas} *(LC or RC)*. At each value of α_{CO}, we compute the linear correlation (LC) and rank correlation (RC) coefficients between Σ_D and $\Sigma_{gas} = \Sigma_{H\,I} + \alpha_{CO} I_{CO}$. The best α_{CO} value will maximize the correlation between these two quantities.
4. *Minimum* χ^2 *of best-fit plane to* I_{CO}, $N_{H\,I}$, *and* Σ_D *(PF)*. The Σ_D, $\Sigma_{H\,I}$, and Σ_{H_2} values describe a plane with two free parameters. At each value of α_{CO}, we fit a plane to the measurements to determine the DGR. The best value of α_{CO} will be the one that minimizes the χ^2 of the best-fit plane.
5. *Minimum correlation coefficient of the DGR versus* $I_{CO}/N_{H\,I}$ *(CHC)*. In this technique, we search for the α_{CO} value that minimizes the correlation of the DGR with $I_{CO}/N_{H\,I}$. This technique weights the points differently depending on how much local Σ_{gas} depends on α_{CO}.

A.2. Definition of the "Solution Pixel" Size and Location

A key aspect of the technique we use to constrain the DGR and α_{CO} is defining the region over which we assume there to be one value each of the DGR. Under ideal circumstances, the regions would be as small as possible given the resolution of the maps. Realistically, however, there are several considerations that must be taken into account when defining the regions, including covering an adequate range of CO/H I ratios, having enough points to measure scatter accurately, and keeping the region to ~kiloparsec scales over which it is reasonable to assume that the DGR is indeed constant.

To complement the hexagonal, half-beam spaced grid with which we sampled the original data (i.e., our "sampling points"), we again use hexagonal spacings to define the "solution pixels" as the individual samples can be divided naturally into concentric hexagons. We tested a variety of solution pixel sizes ranging from 19-point to 271-point hexagons.

We found that 37-point solution pixels were a good compromise between size and solution quality. Because of the underlying half-beam spaced sampling grid, the 37 point solution pixel contains ~9 independent measurements. For the next smallest possible hexagon (19-points), there are not sufficient numbers of independent measurements to reliably judge the scatter in the DGR.

In order to fully sample the map, the center of each hexagonal pixel is offset by 1/2 of the spacing from its neighbor. This technique results in the "solution pixels" not being independent—each neighboring pixel shares ~40% of the same data (the

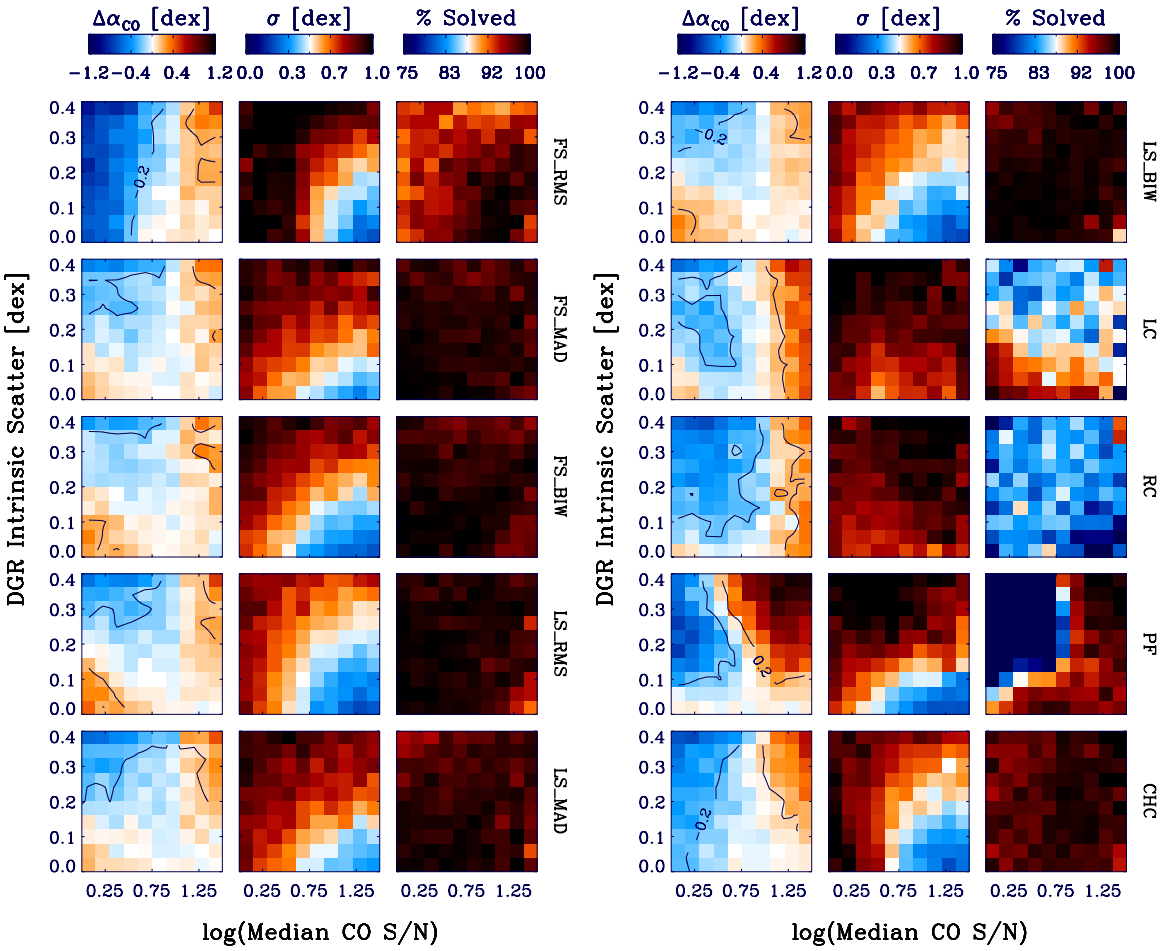

Figure 17. Results of simulated data tests to optimize the solution technique. Columns correspond to: left, the difference between the known input α_{CO} and the recovered best-solution α_{CO} ($\Delta\alpha_{CO}$); middle, the standard deviation of the difference between input and recovered α_{CO} (σ); and right, the fraction of trials in each bin where a solution is achieved. The results are presented as two-dimensional histograms, binned in CO S/N and the simulated intrinsic scatter added to the data. The rows show results for the various solution techniques described previously. From top to bottom in the left panel these are: minimization of the fractional scatter using the mean (FS_RMS), median (FS_MAD), and robust mean (FS_BIW) and the minimization of the logarithmic scatter using the mean (LS_RMS) and median (LS_MAD). In the right panel, we show minimization of the logarithmic scatter using the robust mean (LS_BIW), minimizing the linear correlation coefficient (LC), minimizing the rank correlation coefficient (RC), minimizing the χ^2 of the best-fit plane (PF), and minimizing the correlation coefficient between the DGR and $I_{CO}/\Sigma_{H\,I}$ (CHC). The contours in the $\Delta\alpha_{CO}$ column show the regions of parameter space where the difference in the input and recovered α_{CO} is less than 0.2 dex. The LS_BIW technique minimizes the difference between input and recovered α_{CO} and achieves a small σ over the largest area, although the distinction from FS_BIW is not large.

(A color version of this figure is available in the online journal.)

oversampling can be exactly described as $n^2/(3n^2 - 3n + 1)$ for concentric hexagons).

A.3. Test of the Solution Technique with Simulated Data

We have investigated the efficacy of the various techniques using simulated data modeled on our observations. Our goal is to identify the technique or techniques that return the most accurate values of α_{CO} and the DGR over the range of conditions and S/N levels in our dataset. We also aim to characterize any biases in the recovered α_{CO} as a function of input α_{CO} and S/N. In performing these tests, it is important to model the simulated data on our real observations because the ability of the techniques to judge the DGR uniformity depends not only on the S/N of the measurements but also on the range of CO/H I ratios. Since CO and H I can be correlated, anti-correlated, or independent of each other on kiloparsec scales, depending on the state of the ISM, it is difficult to generate a reasonable set of simulated data from scratch that encompasses the range of CO/H I behaviors in the observations. Therefore, we expect the best test of the technique will come from simulated data that are closely modeled on the observations. In the following, we describe how the simulated data are generated and discuss the results of the test.

The simulated data are generated via a Monte Carlo procedure in which we randomly choose a galaxy from our sample (listed in Table 1) at SPIRE 350 μm resolution, choose a solution pixel, and create simulated data based on the selected CO, H I, and Σ_D samples. For each trial, we randomly sample a range of α_{CO} values between 0.5 and 50 $M_\odot$ pc^{-2} (K km s^{-1})$^{-1}$ and intrinsic scatter per axis (evenly divided among the I_{CO}, $\Sigma_{H\,I}$, and Σ_D axes, for lack of better knowledge of the sources of intrinsic scatter) between 0.0 and 0.4 dex. We note that because of the properties of lognormal distributions, the scatter in the DGR is not simply $\sqrt{3}\times$ the input intrinsic scatter per axis, so we approximate it after the fact using the input scatter per axis and the mean H_2/H I ratio for the simulated measurements.

Our procedure is the following: (1) select the observations with the sampling described above, (2) use the I_{CO} and $\Sigma_{H\,I}$

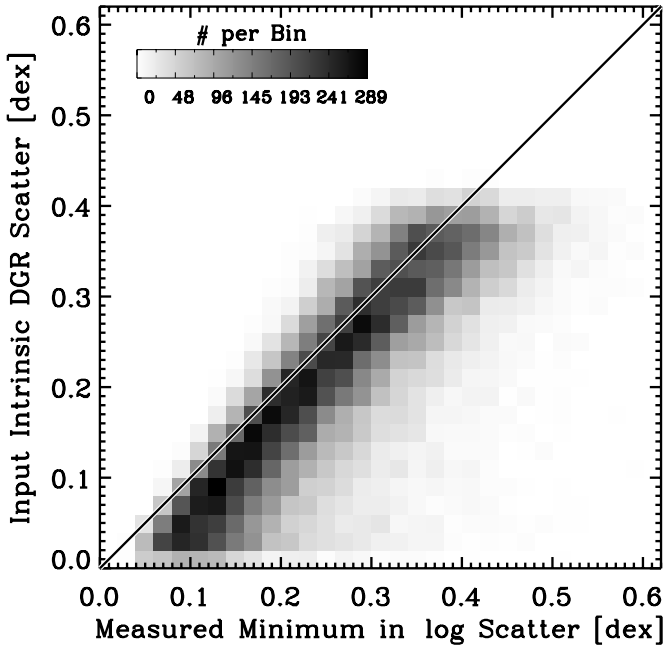

Figure 18. Results of simulated data tests comparing the known input intrinsic scatter in the DGR with the recovered minimum in the DGR scatter. The gray scale represents the number of trials falling in a given bin. We have uniformly sampled input intrinsic scatter values between 0.0 and 0.4 dex. The line shows a one-to-one relationship.

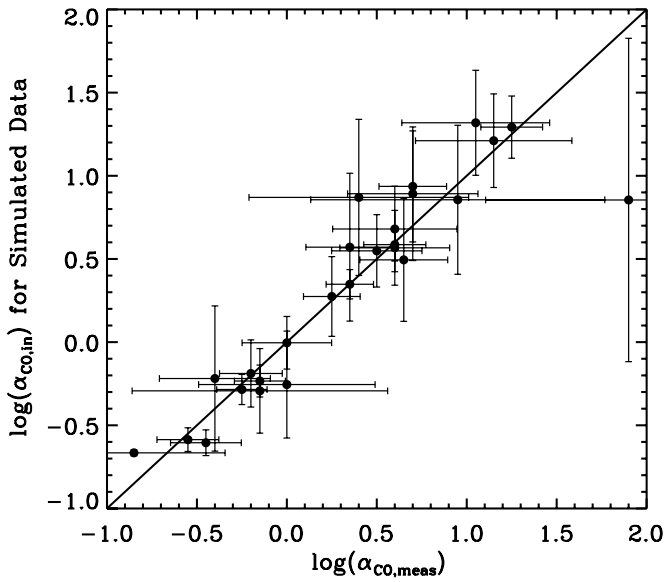

Figure 19. Results of simulated data tests focused on the galaxy centers, where high CO S/N and high CO/H I ratios could bias the recovered α_{CO}. The *x*-axis shows the measured $\alpha_{CO,meas}$ and uncertainty for each of the 26 central points in our sample. The *y*-axis shows the mean and standard deviation of the *known, input* $\alpha_{CO,in}$ values from the simulations where we recovered $\alpha_{CO,out}$ equal to the value we measured. This test shows that the α_{CO} values we measured in the galaxy centers are not biased within their uncertainties.

measurements along with the random α_{CO} value to create a simulated Σ_{gas} vector, (3) calculate the DGR value that preserves the average S/N level of the Σ_D measurements and create a simulated, noise-free Σ_D vector by multiplying the Σ_{gas} from step 2 by this DGR, (4) apply the randomly selected intrinsic scatter to each axis, and (5) add simulated measurement errors according to the observed uncertainties in the I_{CO}, $\Sigma_{H\,I}$, and Σ_D maps. These simulated measurements are then used as inputs

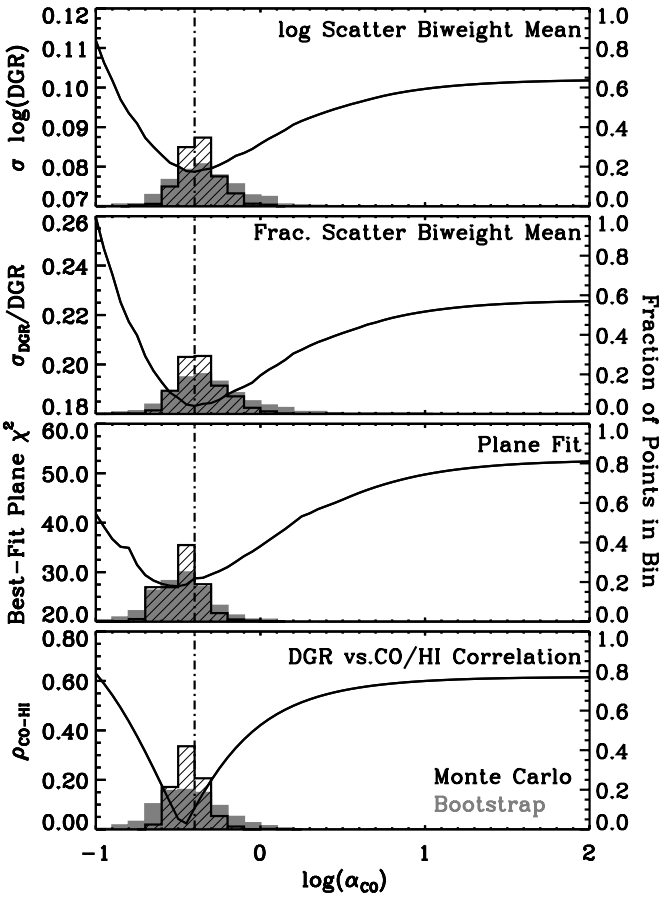

Figure 20. Solution for the central region of NGC 6946. The panels show different statistics we use to measure the uniformity of the DGR in a given solution pixel, all showing a clear minimum at $\alpha_{CO} = 0.4 M_\odot$ pc^{-2} (K km s^{-1})$^{-1}$. A thorough discussion of the various statistics is presented in Appendix A.1. From top to bottom, we show: the scatter in log(DGR) measured using the robust biweight mean (LS_BIW); the fractional scatter of the DGR determined with the biweight mean (FS_BIW); the χ^2 of the best-fit plane to I_{CO}, $\Sigma_{H\,I}$, and Σ_D (PF); and the correlation coefficient between the DGR and the CO/H I ratio (CHC). The dot-dashed vertical line shows the solution for α_{CO} from the LS_BIW technique, which we adopt in the rest of the study. The agreement between different techniques (i.e., minimizing scatter in the DGR, plane-fit, and minimizing the correlation between the DGR and CO/H I) illustrates the high confidence of this solution and shows that it is not an artifact of the solution technique.

to solve for α_{CO} and the DGR using the techniques described above.

From this Monte Carlo simulation, we can then choose the technique that is the most robust (i.e., most frequently achieves a solution) and accurate (i.e., gets closest to the known input α_{CO}). In Figure 17, we show the results of this simulation for the techniques we have outlined. The panels show (left) the mean difference between the input and recovered α_{CO} value, (middle) the standard deviation of the difference of the input and recovered α_{CO}, and (right) the percent of the Monte Carlo trials that achieve a solution. These values are binned in a two-dimensional space defined by the intrinsic scatter added to the simulated data and the median S/N of the simulated CO measurements.

It is clear that the FS and LS techniques provide the least bias in the recovered α_{CO} over the relevant range of intrinsic scatter and S/N (except for the FS_RMS, which is significantly biased at low CO S/N). The correlation coefficient (LC and RC), planefit (PF), and CO/H I correlation (CHC) techniques

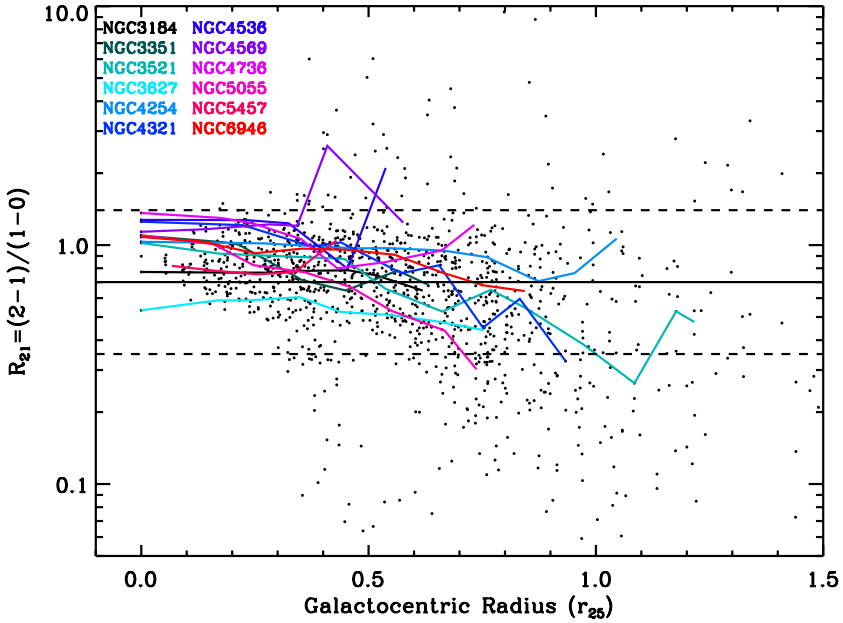

Figure 21. Ratio of the CO $J = (2–1)$ and (1–0) intensities measured from HERACLES and the Nobeyama observations, respectively. The black points show all of the individual measurements from the solution pixels and the colored lines show radial profiles, binned by $0.1r_{25}$. The value we have assumed for converting our (2–1) α_{CO} measurements to the more commonly used (1–0) scale is shown with a solid black line ($R_{21} = 0.7$) and the dashed lines show factors of two above and below that value. The variations of R_{21} are generally less than a factor of two, which is less than the uncertainty on most of our α_{CO} measurements. Note that variations in R_{21} only affect the (1–0) α_{CO}, since we are directly measuring the conversion factor appropriate for the (2–1) line.

(A color version of this figure is available in the online journal.)

all provide much more limited regions with low bias in the recovered α_{CO}, as well as having a lower fraction of solutions. In general, the MAD based techniques have slightly less bias toward the low CO S/N region, but show a larger scatter between the input and recovered α_{CO}. Overall, we find that the LS_BIW (robust BIW mean of the logarithmic scatter) is the technique that shows the best performance in accuracy, precision, and robustness over the range of characteristics of our dataset.

In addition to helping us choose the best technique, the tests with simulated data also allow us to investigate how the measured minimum in the logarithmic scatter corresponds to the known intrinsic scatter added to the simulated data. In addition to being an interesting quantity scientifically, the measured scatter can also help us to identify which region of the parameter space a given solution falls in, thereby allowing us to judge how biased we expect it to be given our knowledge from these simulated data tests. Figure 18 shows a comparison of the known input intrinsic scatter with the measured minimum in the logarithmic scatter for the LS_BIW technique. Most of the outliers come from regions with low CO S/N. At very low levels of intrinsic scatter, the measured scatter is larger due to the influence of observational uncertainties. In general, however, the measured minimum log scatter is a very good proxy for the intrinsic scatter in the DGR.

Based on these results with simulated data, we can use the measured median CO S/N and the measured minimum of the scatter in the DGR values to predict how biased and how uncertain a given determination of α_{CO} is for our dataset. To this end, we use the measured minimum in the DGR scatter as an estimate of the intrinsic DGR scatter (it is biased slightly higher, but this effect is minor and represents a conservative estimate of the intrinsic scatter). Then, using this value and the median CO S/N in the solution pixel, we interpolate in the grid presented in Figure 17 for "LS_BIW" to predict the bias inherent in the technique.

A.4. Testing for Bias at High CO S/N and Low $\Sigma_{H\,I}$

One of the key results of our work is the measurement of low α_{CO} values in the centers of some galaxies (see Section 6.3). These locations are outliers from the average solution pixel in the sense of having high CO S/N and often a relative deficiency in $\Sigma_{H\,I}$. Since these locations make up a small subset of all solution pixels, our Monte Carlo simulations from the previous section may not adequately judge the bias of the technique in these regions since they are not sampled frequently enough (only 26 out of ∼900 solution pixels). We therefore perform a separate Monte Carlo simulation for the galaxy centers in order to verify that these low α_{CO} values are not due to biases in the technique (we have demonstrated that the average pixel in the sample is not biased using the experiment in the previous section).

The results of the technique are biased if the simulation returns an α_{CO} systematically different from the true α_{CO}. For this test, we will define several different α_{CO} values. First, $\alpha_{CO,meas}$ is the measured value for a given solution pixel; we do not know if this measured value is biased as it is only what we have measured for that pixel given the true data. Second, $\alpha_{CO,in}$ is a known α_{CO} value we have used to generate the simulated data. Finally, $\alpha_{CO,out}$ is the α_{CO} value that we recover for $\alpha_{CO,in}$ using our solution technique.

The essence of this test is that we take a range of $\alpha_{CO,in}$ values and map them to their $\alpha_{CO,out}$ values by generating simulated data given $\alpha_{CO,in}$ and running it through our solution technique. This simulated data generation proceeds as described in the previous section and is designed to preserve the CO/H I ratio and S/N of the measurements for a given pixel. In addition to observational noise, we also add intrinsic scatter between 0.01 and 0.1 dex to the simulated data, which reflects the level of intrinsic scatter we have found in the real solutions. For each solution pixel, we generate 10^4 random $\alpha_{CO,in}$ values that span our range of $\alpha_{CO} = 0.1–100$.

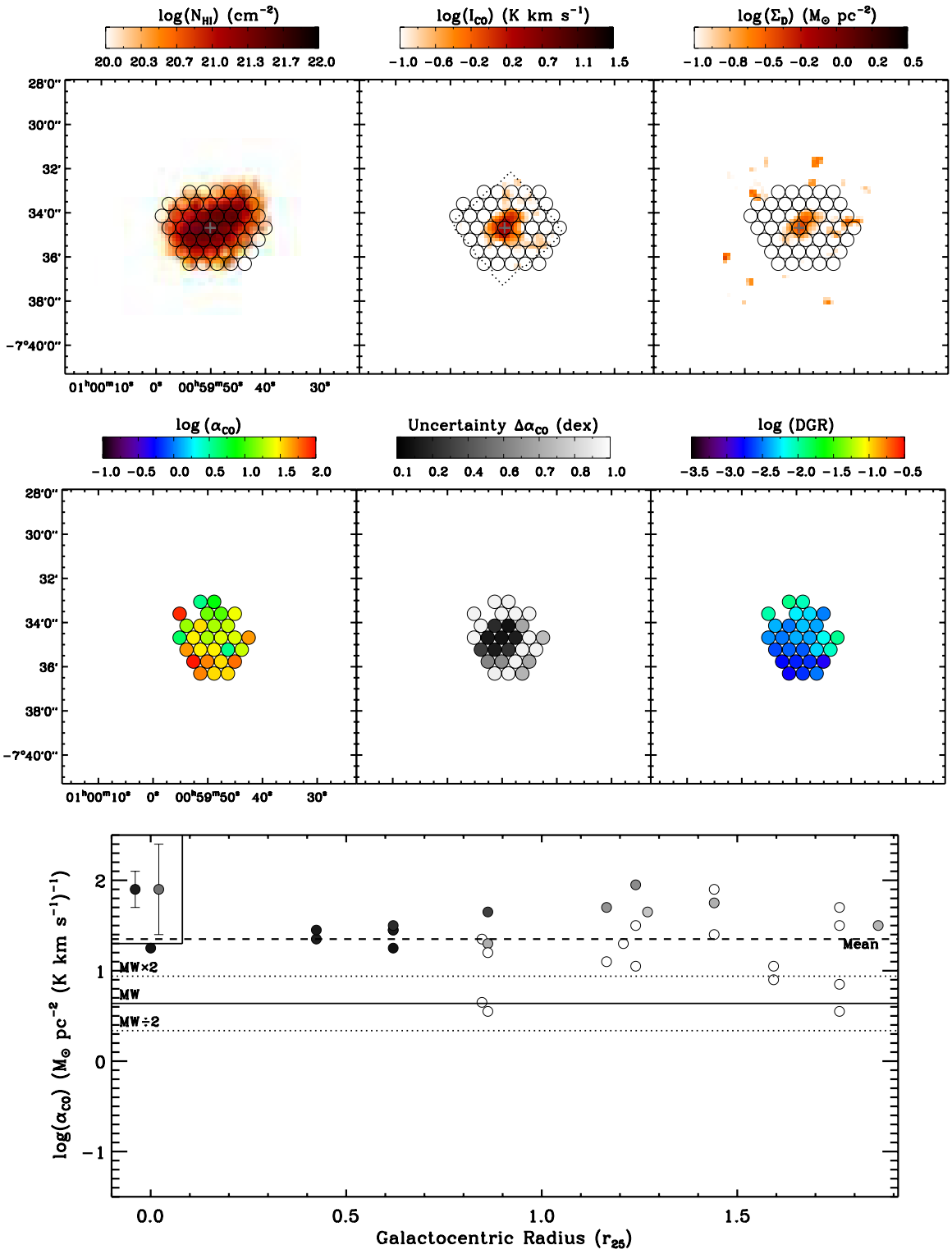

Figure 22. Results for NGC 0337 ($D = 19.3$ Mpc; $1'' = 94$ pc).

(The complete figure set (75 images) and a color version of this figure are available in the online journal.)

With this simulation, we can determine for any given value of $\alpha_{CO,out}$ which values of $\alpha_{CO,in}$ ended up there. If a solution is biased, the correspondence between $\alpha_{CO,in}$ and $\alpha_{CO,out}$ will not be one-to-one. For example, a bias may make us consistently recover $\alpha_{CO,out} = 1\ M_\odot\ pc^{-2}\ (K\ km\ s^{-1})^{-1}$ when $\alpha_{CO,in} = 0.1\ M_\odot\ pc^{-2}\ (K\ km\ s^{-1})^{-1}$.

In judging the biases of the actual solutions for our central solution pixels, we then select all of the $\alpha_{CO,out}$ measurements equal to $\alpha_{CO,meas}$ and find the mean and standard deviation of the $\alpha_{CO,in}$ values that gave those results. In Figure 19, we show a plot of the mean and standard deviation of the relation between the $\alpha_{CO,in}$ values and the $\alpha_{CO,meas}$ values. This figure shows that within the uncertainties of α_{COmeas}, none of the central pixel measurements show a bias.

In addition, a second check on these low central α_{CO}, at least for NGC 6946, is shown in Figure 20 where we

show the minimization curve for several techniques toward its central solution pixel. All techniques agree within their errors, highlighting the minimum at $\alpha_{CO} \sim -0.4$. This result emphasizes that the low α_{CO} found in the center is not an artifact of the particular technique we are using, but can be recovered via minimization of scatter in the DGR, minimization of the correlation coefficient between CO/H I and the DGR, and minimization of the χ^2 of the best-fit plane to CO, H I, and Σ_D.

A.5. Summary of Investigations into the Solution Technique

To summarize, we have tested a number of variations on the basic technique of finding the most "uniform" DGR in a given region by stepping through a grid of α_{CO} values. We created simulated data with known α_{CO} and DGR intrinsic scatter matched to the range of S/N in our dataset. Via a Monte Carlo simulation, we found the robust mean of the logarithmic scatter to be the technique that spans the range of CO S/Ns and possible intrinsic DGR scatters with the highest accuracy and rate of success. Given knowledge of the CO S/N for a region and the measured minimum of the logarithmic scatter, we can use the simulated data tests to constrain how biased our α_{CO} measurement can be. We have also specifically checked that the central regions of galaxies, which only comprise 26 pixels out of the sample, are not biased due to their sometimes unusual CO/H I ratios. We found no significant bias for these solutions and show in addition that a variety of techniques can reproduce the low central α_{CO} solutions, not just the minimization of the DGR scatter.

A.6. Variations in R_{21}

In Figure 21, we show the measured CO (2–1)/(1–0) line ratio in the solution pixels we have defined for each galaxy (the black points) and in radial profiles (colored lines). The assumed R_{21} is shown with a horizontal solid black line and factors of two above and below that value are marked with black dashed lines. There are variations in R_{21}, but in regions with good CO S/N (the only regions in which we will achieve good solutions) these variations are generally less than a factor of two away from the R_{21} we have assumed. This deviation is within the uncertainties on the α_{CO} solutions, which typically have 0.2 dex uncertainty, at minimum.

APPENDIX B

ATLAS OF GALAXIES AND RESULTS

In this Appendix, we present the results for individual solution pixels in all of the galaxies we have considered. In the top panels of Figure 22, we show the H I, CO, and Σ_D maps at matched resolution. The circles overlaid on these figures show the central position of each of the 37-point, hexagonal solution pixels in which we determine α_{CO}. In the middle panel of these same figures, we show on the left the α_{CO} values in color and the associated uncertainties on the right in gray scale. Solution pixels where the solution failed are omitted. Finally, in the bottom panels of the figures, we plot the measured α_{CO} values as a function of galactocentric radius (r_{25}). The color of the points in this plot reflects the uncertainties on the α_{CO} values, as shown in the gray scale color table in the middle panel.

REFERENCES

Abdo, A. A., Ackermann, M., Ajello, M., et al. 2010, ApJ, 710, 133
Aniano, G., Draine, B. T., Calzetti, D., et al. 2012, ApJ, 756, 138
Aniano, G., Draine, B. T., Gordon, K. D., & Sandstrom, K. M. 2011, PASP, 123, 1218
Bakes, E. L. O., & Tielens, A. G. G. M. 1994, ApJ, 427, 822
Bayet, E., Gerin, M., Phillips, T. G., & Contursi, A. 2006, A&A, 460, 467
Bell, T. A., Roueff, E., Viti, S., & Williams, D. A. 2006, MNRAS, 371, 1865
Bigiel, F., Bolatto, A. D., Leroy, A. K., et al. 2010, ApJ, 725, 1159
Blanc, G. A., Schruba, A., Evans, N. J., II., et al. 2013, ApJ, 764, 117
Bolatto, A. D., Leroy, A. K., Rosolowsky, E. W., Walter, F., & Blitz, L. 2008, ApJ, 686, 948
Braun, R., Thilker, D. A., Walterbos, R. A. M., & Corbelli, E. 2009, ApJ, 695, 937
Bresolin, F. 2007, ApJ, 656, 186
Calzetti, D., Kinney, A. L., & Storchi-Bergmann, T. 1994, ApJ, 429, 582
Daddi, E., Elbaz, D., Walter, F., et al. 2010, ApJL, 714, L118
Dahmen, G., Huttemeister, S., Wilson, T. L., & Mauersberger, R. 1998, A&A, 331, 959
Dame, T. M., Hartmann, D., & Thaddeus, P. 2001, ApJ, 547, 792
de Blok, W. J. G., Walter, F., Brinks, E., et al. 2008, AJ, 136, 2648
Digel, S. W., Grenier, I. A., Heithausen, A., Hunter, S. D., & Thaddeus, P. 1996, ApJ, 463, 609
Dobashi, K., Bernard, J.-P., Hughes, A., et al. 2008, A&A, 484, 205
Donovan Meyer, J. L., Koda, J., Momose, R., et al. 2012, ApJ, 744, 42
Donovan Meyer, J. L., Koda, J., Momose, R., et al. 2013, ApJ, 772, 107
Downes, D., & Solomon, P. M. 1998, ApJ, 507, 615
Downes, D., Solomon, P. M., & Radford, S. J. E. 1993, ApJL, 414, L13
Draine, B. T. 2011, in Physics of the Interstellar and Intergalactic Medium, (Princeton, NJ: Princeton Univ. Press)
Draine, B. T., Dale, D. A., Bendo, G., et al. 2007, ApJ, 663, 866
Draine, B. T., & Li, A. 2007, ApJ, 657, 810
Dwek, E. 1998, ApJ, 501, 643
Feldmann, R., Gnedin, N. Y., & Kravtsov, A. V. 2012, ApJ, 747, 124
Glover, S. C. O., & Mac Low, M.-M. M. 2011, MNRAS, 412, 337
Goldsmith, P. F., Heyer, M., Narayanan, G., et al. 2008, ApJ, 680, 428
Gratier, P., Braine, J., Rodriguez-Fernandez, N. J., et al. 2012, A&A, 542, 108
Herrera-Camus, R., Fisher, D. B., Bolatto, A. D., et al. 2012, ApJ, 752, 112
Hirashita, H., Tajiri, Y. Y., & Kamaya, H. 2002, A&A, 388, 439
Israel, F. P. 1997, A&A, 328, 471
Israel, F. P. 2009a, A&A, 493, 525
Israel, F. P. 2009b, A&A, 506, 689
Israel, F. P., & Baas, F. 1999, A&A, 351, 10
Israel, F. P., & Baas, F. 2001, A&A, 371, 433
Jenkins, E. B. 2009, ApJ, 700, 1299
Kainulainen, J., Alves, J., Beuther, H., Henning, T., & Schuller, F. 2011, A&A, 536, 48
Kaufman, M. J., Wolfire, M. G., Hollenbach, D. J., & Luhman, M. L. 1999, ApJ, 527, 795
Kennicutt, R. C., Calzetti, D., Aniano, G., et al. 2011, PASP, 123, 1347
Kennicutt, R. C., Jr., Armus, L., Bendo, G., et al. 2003, PASP, 115, 928
Kobulnicky, H. A., & Kewley, L. J. 2004, ApJ, 617, 240
Krips, M., Neri, R., García-Burillo, S., et al. 2008, ApJ, 677, 262
Kuno, N., Sato, N., Nakanishi, H., et al. 2007, PASJ, 59, 117
Leroy, A. K., Bigiel, F., de Blok, W. J. G., et al. 2012, AJ, 144, 3
Leroy, A. K., Bolatto, A., Bot, C., et al. 2009a, ApJ, 702, 352
Leroy, A. K., Bolatto, A., Gordon, K., et al. 2011, ApJ, 737, 12
Leroy, A. K., Walter, F., Bigiel, F., et al. 2009b, AJ, 137, 4670
Leroy, A. K., Walter, F., Brinks, E., et al. 2008, AJ, 136, 2782
Leroy, A. K., Walter, F., Sandstrom, K., et al. 2013, AJ, 146, 19
Lisenfeld, U., & Ferrara, A. 1998, ApJ, 496, 145
Liszt, H. S., & Lucas, R. 1998, A&A, 339, 561
Liszt, H. S., & Pety, J. 2012, A&A, 541A, 58L
Liszt, H. S., Pety, J., & Lucas, R. 2010, A&A, 518, 45
Lombardi, M., Alves, J., & Lada, C. J. 2011, A&A, 535, 16
Mao, R. Q., Henkel, C., Schulz, A., et al. 2000, A&A, 358, 433
Martin, P. G., Roy, A., Bontemps, S., et al. 2012, ApJ, 751, 28
Mathis, J. S., Mezger, P. G., & Panagia, N. 1983, A&A, 128, 212
Meidt, S. E., Schinnerer, E., Knapen, J. H., et al. 2012, ApJ, 744, 17
Meier, D. S., & Turner, J. L. 2004, AJ, 127, 2069
Meier, D. S., Turner, J. L., & Beck, S. C. 2001, AJ, 122, 1770
Moustakas, J., Kennicutt, R. C., Tremonti, C. A., et al. 2010, ApJS, 190, 233
Narayanan, D., Krumholz, M. R., Ostriker, E. C., & Hernquist, L. 2012, MNRAS, 421, 3127
Oka, T., Hasegawa, T., Hayashi, M., Handa, T., & Sakamoto, S. 1998a, ApJ, 493, 730
Oka, T., Hasegawa, T., Sato, F., Tsuboi, M., & Miyazaki, A. 1998b, ApJS, 118, 455
Paglione, T. A. D., Wall, W. F., Young, J. S., et al. 2001, ApJS, 135, 183

Papadopoulos, P. P., van der Werf, P., Xilouris, E., Isaak, K. G., & Gao, Y. 2012, ApJ, 751, 10
Pilyugin, L. S., & Thuan, T. X. 2005, ApJ, 631, 231
Pineda, J. E., Caselli, P., & Goodman, A. A. 2008, ApJ, 679, 481
Planck Collaboration, Abergel, A., Ade, P. A. R., et al. 2011a, A&A, 536, 25
Planck Collaboration, Ade, P. A. R., Aghanim, N., et al. 2011b, A&A, 536, 19
Press, W. H., Teukolsky, S. A., Vetterling, W. T., & Flannery, B. P. 2002, Numerical Recipes in C++: The Art of Scientific Computing, Vol. xxviii (Cambridge: Cambridge Univ. Press)
Regan, M. W., Thornley, M. D., Helfer, T. T., et al. 2001, ApJ, 561, 218
Röllig, M., Ossenkopf, V., Jeyakumar, S., Stutzki, J., & Sternberg, A. 2006, A&A, 451, 917
Sánchez, S. F., Cardiel, N., Verheijen, M. A. W., et al. 2007, A&A, 465, 207
Schinnerer, E., Weiss, A., Aalto, S., & Scoville, N. Z. 2010, ApJ, 719, 1588
Schruba, A., Leroy, A. K., Walter, F., et al. 2011, AJ, 142, 37
Schruba, A., Leroy, A. K., Walter, F., et al. 2012, AJ, 143, 138
Shetty, R., Glover, S. C. O., Dullemond, C. P., et al. 2011, MNRAS, 415, 3253
Sodroski, T. J., Odegard, N., Dwek, E., et al. 1995, ApJ, 452, 262
Solomon, P. M., Rivolo, A. R., Barrett, J., & Yahil, A. 1987, ApJ, 319, 730
Strong, A. W., & Mattox, J. R. 1996, A&A, 308, L21
Strong, A. W., Moskalenko, I. V., Reimer, O., Digel, S., & Diehl, R. 2004, A&A, 422, L47
Tielens, A. G. G. M., & Hollenbach, D. 1985, ApJ, 291, 722
van Dishoeck, E. F., & Black, J. H. 1988, ApJ, 334, 771
Walsh, W., Beck, R., Thuma, G., et al. 2002, A&A, 388, 7
Walter, F., Brinks, E., de Blok, W. J. G., et al. 2008, AJ, 136, 2563
Walter, F., Weiss, A., Martin, C. L., & Scoville, N. Z. 2002, AJ, 123, 225
Wei, L. H., Keto, E., & Ho, L. C. 2012, ApJ, 750, 136
Weiß, A., Neininger, N., Hüttemeister, S., & Klein, U. 2001, A&A, 365, 571
Weingartner, J. C., & Draine, B. T. 2001, ApJ, 548, 296
Wilson, C. D. 1995, ApJL, 448, L97
Wolfire, M. G., Hollenbach, D., & McKee, C. F. 2010, ApJ, 716, 1191
Wolfire, M. G., Hollenbach, D., & Tielens, A. G. G. M. 1993, ApJL, 402, L195
Zibetti, S., & Groves, B. A. 2011, MNRAS, 417, 812